TESIS DE LA UNIVERSIDAD DE ZARAGOZA

2024

105

Raúl Garde Casasnovas

New calibration strategies in high-resolution continuum source atomic/molecular absorption spectrometry aiming at the determination of non-metals and the sizing of nanoparticles

Director/es

Resano Ezcaray, Martín

García Ruíz, María Esperanza

ISSN 2254-7606

Prensas de la Universidad Universidad Zaragoza

Universidad de Zaragoza
Servicio de Publicaciones

ISSN 2254-7606

Universidad Zaragoza
1542

Tesis Doctoral

NEW CALIBRATION STRATEGIES IN HIGH-RESOLUTION CONTINUUM SOURCE ATOMIC/MOLECULAR ABSORPTION SPECTROMETRY AIMING AT THE DETERMINATION OF NON-METALS AND THE SIZING OF NANOPARTICLES

Autor

Raúl Garde Casasnovas

Director/es

Resano Ezcaray, Martín
García Ruíz, María Esperanza

UNIVERSIDAD DE ZARAGOZA
Escuela de Doctorado

Programa de Doctorado en Ciencia Analítica en Química

2022

Universidad Zaragoza
1542

Doctoral Thesis

New calibration strategies in high-resolution continuum source atomic/molecular absorption spectrometry aiming at the determination of non-metals and the sizing of nanoparticles

Author

Raúl Garde Casasnovas

Director/s

Martín Resano Ezcaray

María Esperanza García Ruíz

UNIVERSIDAD DE ZARAGOZA

Química Analítica

PUBLICATIONS

The present author has participated in various articles during his work in the group of MARTE, starting in 2015. All the data presented in **chapter I** has been published in article 1 while chapters **II and III** have produced two draft articles that are still being revised by the authors before submission:

Article 1) R. Garde, F.V. Nakadi, E. García-Ruíz and M. Resano ***J. Anal. At. Spectrom***.,2020, **35**,2606–2619
https://pubs.rsc.org/en/content/articlehtml/2020/ja/d0ja00359j

Article 2) Simultaneous Determination of Halogens in Active Pharmaceutical Compounds *via* Continuum Source Graphite Furnace Molecular Absorption Spectrometry coupled with a Modular Simultaneous *Echelle* Spectrograph (CS GF MAS-MOSES) “in preparation”

Article 3) Size Characterization of core-shell structures *via* High-Resolution Continuum Source Atomic Absorption Spectrometry and characterization of other metallic nanoparticles and mixtures “in preparation”

Moreover, the author has participated in other related publications prior (Article 4) or during the realization of the current PhD (articles 5 and 6):

Article 4) M. Resano, E. García-Ruíz and R. Garde, ***J. Anal. At. Spectrom***.,2016, **31**, 2233
https://pubs.rsc.org/en/content/articlepdf/2016/ja/c6ja00280c
Article 5) F.V. Nakadi, R. Garde, M.A.M.S Da Veiga, J. Cruces and M.Resano, ***J. Anal. At. Spectrom***., 2020, **35**, 136
https://pubs.rsc.org/en/content/articlepdf/2020/ja/c9ja00348g
Article 6) A novel approach for adapting the standard addition method to single particle-icp-ms for the accurate determination of np size and number concentration in complex matrices “under peer review”.

AGRADECIMIENTOS

Después de un TFG, un TFM y esta tesis, llegó el momento de abandonar el grupo MARTE. Han pasado ya 6 años desde que comencé a realizar mis primeras medidas con el contrAA.

A las primeras personas que me gustaría agradecer esta tesis es a mis directores, Martín y Espe. Especialmente por los buenos ratos rodeados de fantástica comida y cerveza. Y por el apoyo en los momentos de debilidad. Gracias

A continuación, a mis compañeros del laboratorio a lo largo de estos años, Sharay, Antonio, Maite, etc., pero especialmente al clan brasileño, encabezado por Diego y Flavio. Sin vosotros habría sido menos *gostoso.*

No me gustaría acabar estas líneas sin dedicar unas palabras a mis padres, por todo el apoyo, ayuda y cariño que me brindáis siempre.

Por último, a Elisa, que a pesar de que le digo mucho que es una pesada, me aburriría como una ostra sin ella. Te quiero. Ah, y a Moko y Mica, no hay mejores peluches antiestrés que vosotros.

This work has been funded by:

El **Ministerio de Economía y Competitividad** (**Proyecto CTQ2015-64684-P** (MINECO/FEDER)) and **FPI grant BES-2016-078971** y el **Ministerio de Ciencia e Innovación** (proyecto **PGC2018-093753-BI00** (MCIU/AEI//FEDER, UE)).

El **Gobierno de Aragón** a través de las convocatorias de Grupos de Investigación (**Grupo M.A.R.T.E.**, E-41 (2015 y 2016), E43_17R (2017-19) y E43_20R (2020-2022), Fondo Europeo de Desarrollo Regional y FEDER Aragón 2014-2020).

The European Regional Development Fund for financial support through the project **Interreg POCTEFA EFA176/16/DBS,** through the Interreg V-A Spain-France-Andorra programme (POCTEFA 2014-2020). POCTEFA aims to reinforce the economic and social integration of the French–Spanish-Andorran border. Its support is focused on developing economic, social and environmental cross-border activities through joint strategies favouring sustainable territorial development.

CONTENTS

1. Introduction

1.1. Calibration

Calibration involves the relationship of a measured response caused by a physical or chemical perturbation varying in a set of standards with a known and controlled variable. The International Union of Pure and Applied Chemistry (IUPAC) defines calibration as “an operation that relates an output quantity to an input quantity for a measuring system under given conditions” but afterwards specifies the calibration in analytical chemistry as a relation between an analytical function $x = f(g)$ and a measured function $y = g(z)$.[1]

From the perspective of an analytical chemist, the first techniques capable of providing a quantitative result were based on what is called absolute methods, which do not required to know the exact concentration or purity of any reagent to derive the analyte concentration, such as in gravimetric and coulometry approaches.[2] Such methods, thus, required no methodological calibration and are called absolute methods of analysis. However, their area of application is rather limited. In contrast with them, the vast majority of analytical methods can only provide quantitative information if the concentration or purity of at least one reagent is previously known or established, and these are termed relative methods of analysis.

In some cases, the exact mathematical relation between the analytical response and the concentration of the analyte can be established beforehand. That is the case in volumetric approaches, as such relation is directly related to the stoichiometry of a chemical reaction. But, for most methods, the property measured depends on many other factors such as pressure, temperature, energy applied, etc., and it is impossible to infer a representative result without

establishing first the exact relation between the analytical response and the concentration of the analyte. This relation is established through the measurement of standards, prior to the measurement of the unknown sample.[3]

In the late 80s and 90s, new types of absolute methods were studied to be implemented in instrumental techniques, but the absence of control over many factors affecting the physico-chemical parameters varying during analyses hampered their traceability and application and, finally, this line of investigation lost attention.[4]

1.2. **Relative methods**

The response function found in many techniques between the analytical signal and concentration is not completely stable over the course of time, bringing the necessity of assessing this response frequently. This relationship can follow different mathematical trends, the most common being linear. Despite being the most common trend, other mathematical functions have been applied: a common technique in routine laboratories, ion selective electrodes, are used to determine the concentration of ions using the Nernst equation, a logarithmic function. Nevertheless, linear relations typically offer the best precision in the end, so they are recommended.

External calibration (EC) is the preferred method of calibration carried out in reference laboratories for univariate methods due to Its simplicity, practicality, and quickness. A set of standards with different concentrations are measured to correlate its signal using a linear function.

Overall, the results will ultimately depend highly on the quality of the calibration curve used, as well as on the position of the unknown samples in the calibration

curve: lower errors are obtained in the centroid of the curve, which may require adjusting the dilution factor.

1.3. Other calibration strategies

Even though EC is the most common calibration approaches applied in univariate reference methods for instrumental techniques, other strategies have been developed in the last years when data did not fit a linear function, or to improve a certain feature.[5] The simplest solution for a dynamic range is bracketing the curve in linear segments. Then, all the statistical considerations of linear regression will be fulfilled for that specific range.

Another solution to non-linear methods was the application of polynomial functions. However, precision will be also a function dependent on the concentration as well.

However, not only concentration can be determined using a calibration strategy. A good example is single particle inductively coupled plasma mass spectrometry (sp-ICP-MS)[6] which is a technique based on a high dilution of dispersion of NPs to be introduced one by one inside the plasma to determine size and concentration according to frequency and intensity of the pulses. Of course, the ionization process of an ICP-MS and the aerosol formation makes that many NPs are lost in its way to be analyzed; thus, two calibration strategies must be done to determine size and concentration. The first one is a size calibration. This is often carried out using one dispersion of NPs well characterized in terms of number of particles. The second calibration sets the sensitivity response for one of the elements found in NP of interest, by using standards of increasing concentration of either ions or NPs.

Another quantitative method, isotopic dilution (ID), exploits the well-known natural isotopic abundances.[7] For quantitative purposes, in principle, only two solutions need to be measured to achieve quantitative result with this approach, the sample and a blend of the sample enriched with one of the isotopes, to change the natural proportion of isotopes.

These alternatives are just a few examples of the many univariate methods developed to overcome or circumvent a particular issue hampering a specific application.

1.4. Drawbacks of calibration strategies

EC is extremely practical for the analysts; many samples can be treated with the same curve. However, if the behavior showed by these curves does not match the samples of interest, and a proportional or additive interference occur, a different approach must be applied, such as matrix matching or standard addition, because EC does not provide accurate results if samples and standards do not behave similarly.

Matrix-matching and standard addition are better choices if the analyst presumes the presence of an interference. These two solve proportional interferences using the same mechanism: the interferent is in all the standards measured because it is added to the standards (matrix-matching) or because they are prepared in conjunction with the sample (standard addition). Of course, isotope diluted is also an option in this case, but it is limited to species possessing at least two stable isotopes.

1.5. New strategies of calibration in the context of for atomic and molecular spectrometry

Absorption spectrometry (AS) is a technique that started its development in 1952, when Alan Wash wondered why absorption was preferred for molecular analysis and emission used in atomic methods. Even though his studies showed that absorption should be evaluated for atomic methods in the future, he also concluded that the relationship between concentration and absorption depends on instrument resolution, and if a continuum source was used, a resolution of 2 pm would be required. The appearance of a commercial hollow cathode lamps a few years later, permitted the inclusion of a line source radiation, circumventing the resolution problem.[8]

AS takes advantage of the relationship between loss of electromagnetic radiation and concentration following Beer-Lambert's law (equation 1):

Equation 1: $I = I_0 e^{-k\,l\,C}$

Where I_0 and I are the radiation intensity before and after the , k is the absorption coefficient, l is the optical path and C is the concentration of the entity absorbing. As denoted in eq. 1, the relationship between radiation and concentration is exponential, however, a new parameter was introduced to obtain a linear relationship (equation 2):

Equation. 2: $A = \log\frac{I_0}{I} = \log(e)\ k\ \mathrm{l}\ \mathrm{C}$

The new term A, Absorbance is directly proportional to the concentration.

The instrumentation for AAS consists of a radiation source, an atomizer, a monochromator system, and a detection system. The most common light source is the HCL mentioned before, made of the element of interest to emit radiation at the same wavelength of the electronic transitions of the analyte. The two atomizers that have been most often used are flame (F) and graphite furnace

(GF) atomizers. The first one uses a combustion to produce a high temperature flame. The second, an electrothermal heating conducted though graphite.

For the next decades, AAS was primarily used to determine metallic elements from the main groups, as the HCL of rare-earth elements and many non-metals were not available. Thus, the development of a continuum source for AAS was necessary to not disappear in the next decades.

Finally, the development of commercially available high-resolution continuum source atomic absorption spectrometers (HR CS AAS) open a new field for the development of non-only atomic but also molecular methods, and for the simultaneous monitorization of multiple lines.[9] However, the spectral window of such instrumentation is still limited to approximately 1 nm in the best cases (**figure 1**).

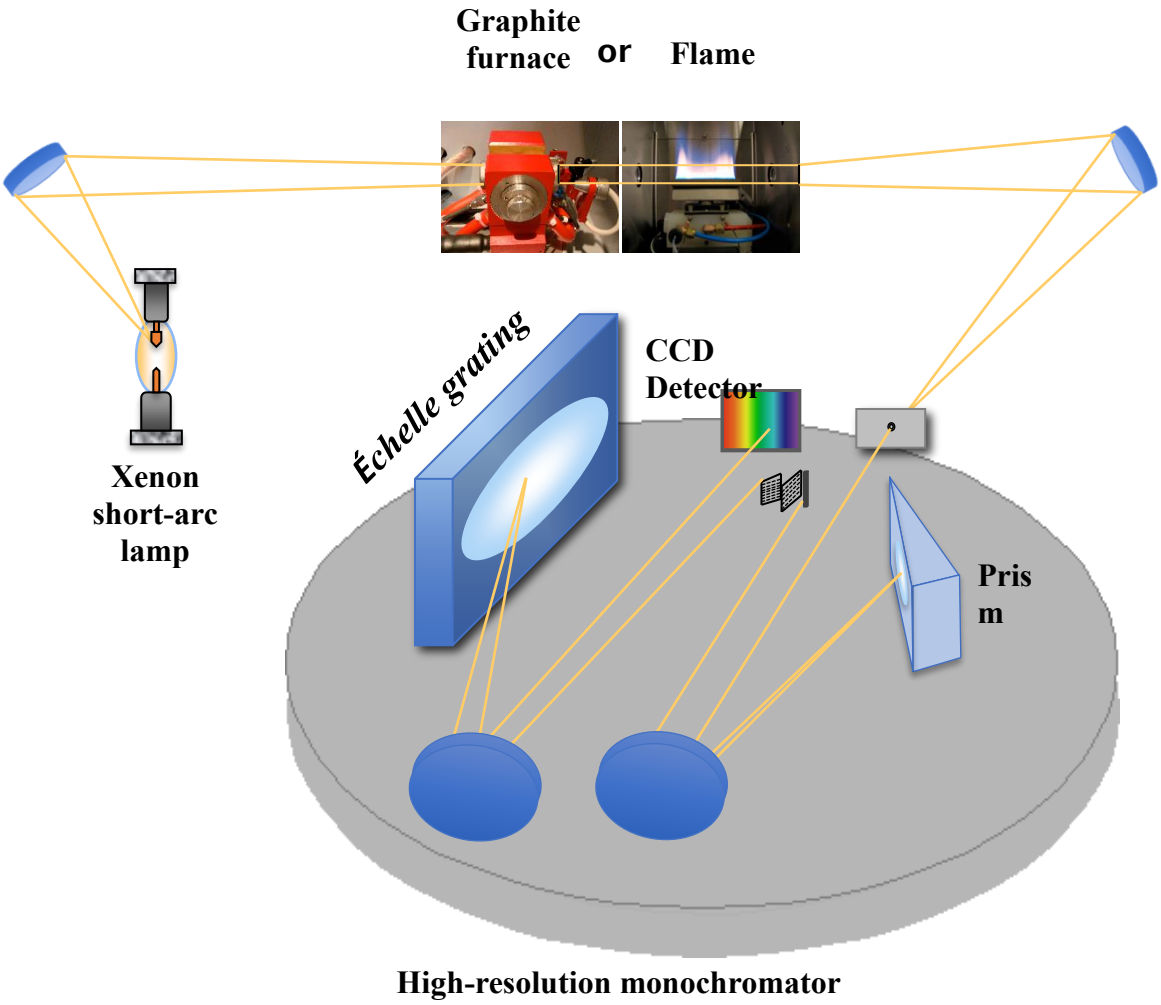

Figure 1: Setup of high-resolution continuum source atomic absorption spectrometer. Reproduced with permission from Elsevier (https://link.springer.com/article/10.1007/s00216-010-4105-x)[10]

Normally, EC is used in AAS and MAS methodologies. However, these techniques are not immune to the occurrence of interferences. Spectral interference can be sometimes resolved due to the high-resolution of the instrumentation deployed. Still, the development of fast methods that can solve proportional interferences is needed.

Recently a set of articles involving the monitorization of several response signals originating from the same analyte have been published. The main principle

followed by this methodology is that every “channel” measured will respond in the same manner, and the relationships of the sample and the sample spiked with a known amount of analyte will remain the same for each measured “channel”, similarly to ID methods. The main advantages of these methods are that they are fast to apply, easy to calculate and interpret and they can solve proportional interferences using the same principle found in standard addition.[11–13] The application of this novel methodology to HR CS AAS/MAS is still very scarce.[14,15]

On the other hand, multivariate analysis and machine learning has been expanding in the different branches of analytical chemistry. Several reviews can be found in the literature, like the chemometrics series. In 2013 the seventeenth review of the series was published. This is an interesting set of reviews covering different time lapses with new methods developed about this task.[16] The capacity of the models to interpret data conjunctly improves the decision making of the analyst, founding new correlations between variables and/or which variables do not influence the model. Again, these approaches were not applied to HR CS AAS/MAS at the moment of beginning this thesis.

Lastly, as discussed before, not all calibration approaches intend to determine the concentration of the measurand. The undeniable importance of nanoscience has brought new requirements to analytical chemistry. Sizing nanoparticles (NPs) is one of them. HR CS GFAAS shows some potential for its use as screening method to differentiate among ions and NPs of some metallic species (Au, Ag, Fe, Zn) and to estimate sizes of some metallic NPs (Au, Ag) and other nanostructured materials,[17–21] since the atomization process seems to be delayed in the presence of bigger NPs of these elements. It is therefore necessary to established suitable calibrations approaches for this new area of

application, establishing the parameters that vary with the size of the NP and the functions that they follow.

All these aspects will be discussed in much more detail in the respective chapter where they will be investigated.

1.6. References

1 K. Danzer and L. A. Currie, ***Pure Appl. Chem***., 1998, **70**, 993–1014.
2 B. V. L'Vov, ***J. Anal. At. Spectrom.***, 1988, **3**, 9–12.
3 L. Cuadros-Rodríguez, L. Gámiz-Gracia, E. M. Almansa-López and J. M. Bosque-Sendra, ***TrAC - Trends Anal. Chem***., 2001, **20**, 620–636.
4 A. Hulanicki, ***Anal. Proc***., 1992, **29**, 512–516.
5 G. L. Donati and R. S. Amais, ***J. Anal. At. Spectrom.,*** 2019,**34,** 2353-2369
6 F. Laborda, E. Bolea and J. Jiménez-Lamana, ***Trends Environ. Anal. Chem.***, 2016, **9**, 15–23.
7 P. Rodríguez-González, J. M. Marchante-Gayón, J. I. García Alonso and A. Sanz-Medel, ***Spectrochim. Acta - Part B At. Spectrosc.,*** 2005, **60**, 151–207.
8 B. Welz, H. Becker-Ross, S. Florek and U. Heitmann, ***Historical Development of Continuum Source AAS***, 2006.
9 M. Resano, M. R. Flórez and E. García-Ruiz, ***Spectrochim. Acta - Part B At. Spectrosc***., 2013, **88**, 85–97.
10 M. Resano and E. García-Ruiz, ***Anal. Bioanal. Chem***., 2011, **399**, 323–330.
11 C. B. Williams and G. L. Donati, ***J. Anal. At. Spectrom.***, 2018, **00**, 1–6.
12 A. Virgilio, J. A. Nóbrega, G. L. Donati, ***Anal Bioanal Chem.,*** 2018,**410**(3), 1157-1162.
13 D. V. Babos, A. Virgilio, V. C. Costa, G. L. Donati and E. R. Pereira-Filho, ***J. Anal. At. Spectrom***., 2018, **33**, 1753–1762.
14 A. Virgilio, D. A. Gonçalves, T. Mcsweeney, J. A. Neto, J. A. Nóbrega and G. L. Donati, ***Anal Chim Acta***, 2017, **982**, 31-36.
15 A. L. Vieira, D. A. Gonçalves, A. Virgilio, E. C. Ferreira, B. T. Jones, G. L. Donati and J. A. Gomes Neto, ***J. Anal. At. Spectrom***., 2019, **34**, 972–978.
16 B. K. Lavine, J. Workman, ***Analytical Chemistry,*** 2013, **85**, 705.
17 F. Gagné, P. Turcotte and C. Gagnon, ***Anal. Bioanal. Chem.***, 2012, **404**, 2067–2072.
18 N. S. Feichtmeier and K. Leopold, ***Anal. Bioanal. Chem***., 2013, **406**, 3887–3894.
19 M. Resano, E. Garcia-Ruiz and R. Garde, ***J. Anal. At. Spectrom***., 2016, **31**, 2233–2241.
20 J. C. García-Mesa, P. Montoro-Leal, A. Rodríguez-Moreno, M. M. López Guerrero and E. I. Vereda Alonso, ***Talanta***, 2021, **223**, 121795.
21 M. T. S. Cordero and J. M. C. Pav, ***J. Anal. At. Spectrom***., 2016, **31**, 2391–2398.

2. Objectives

This thesis is focused on the study of new calibration strategies in absorption spectrometry, with special attention to the conditions and data analysis to provide accurate and precise results. Again, the specific aspects of each calibration assessed will be discussed in much more detail in the introductory section of each experimental chapter.

In short, three different new approaches in absorption spectrometry will be investigated.

2.1. Multi energy calibration (MEC) in HR CS GF MAS, as a possibility to overcome for the often-occurring chemical interferences when an element is determined via the monitoring of a molecular spectrum. The best condition for applying this calibration techniques will be investigated, and a new approach deriving from MEC labelled multi-energy ratio will be proposed and compared with it.

2.2. A Machine Learning XGBoost strategy to solve proportional and spectral interferences with HR CS GFMAS coupled with a Modullar Simultaneous Echelle Spectrograph for simultaneous halogen determination.

2.3. Calibration using the temporal delays of the time-absorption signal profiles for the sizing of NPs and core-shell NPs via HR CS GF AAS

3. Dissertation

Chapter I

Introducing multi-energy ratios as an alternative to multi-energy calibration for Br determination *via* high-resolution continuum source graphite furnace molecular absorption spectrometry. A case study

- **I.1. Introduction**

Quantitative methods of analysis rely on the relation between the signal of the analyte and the concentration of such analyte in a sample, a relation that should be either known in advance *via* theoretical considerations without the use of any analytical standard of known concentration (absolute methods), or else experimentally established using analytical standard(s). In instrumental analysis, many efforts have been directed at the development of absolute methods.[1,2] However, in the end, the most popular strategies depend on external calibration based on linear regression statistics, a method that fits the data to a linear curve minimizing the error in the Y-axis (analytical signal), since the error in the X-axis (analyte concentration or total amount) is considered as negligible in comparison. But the presence of the matrix in the sample can affect the analytical signal, due to the occurrence of interferences. Use of internal standards is a widely accepted approach to minimize such interferences to some extent, although it cannot always be used as monitoring two different signals at the same time sometimes is not possible. Alternative calibration approaches such as standard addition or matrix-matching show the potential to correct for some of these matrix-related interferences.[3-6] These approaches provide some benefits but also come with some drawbacks, such as requiring more effort, resulting in a lower sample throughput, and, in the case of matrix-matching, the necessity to know or determine the presence of some compounds to replicate such matrix.

Alternatively, in the case of using techniques in which the signal of different isotopes can be selectively measured, isotope dilution is a powerful approach. Unlike the methods discussed before, isotope dilution mass spectrometry does not rely on linear regression. Instead, the well-known natural abundances of the stable isotopes are considered “true”, or else, their relation can be experimentally

measured. A spike of the target species that shows a substantially different isotopic composition from the natural one is also required. Typically, by measuring two isotopes free from spectral overlaps of the target species in an aliquot of the sample, an aliquot of the spike and an aliquot of an isotopically equilibrated mixture of sample plus spiked (blend), the signals from such isotopes can be ratioed and from those values the analyte content in the sample can be derived.[7] This methodology is considered a primary analytical technique due to its high precision and potential to correct for matrix effects.[8,9] However, it is not always possible to make use of it, among other reasons simply because in elemental analysis the target analyte may not possess more than one stable isotope.

Recently, a new calibration methodology has been introduced by Virgilio *et al*.[10] This strategy exploits the monitorization of several "channels" (*i.e.*, energetic transitions; isotopes; polyatomic species) of the same analyte of two aliquots: sample spiked with a blank (sample+blank) and sample spiked with a known amount of analyte (sample+standard). By plotting the signals from such aliquots and performing linear regression, the mass or concentration of the sample can be calculated using the slope of such linear regression (see section 3.1.1. for more details).

This represents an ingenious approach with potential to overcome matrix interferences without the need for performing extra measurements. In fact, the number of measurements is actually lower than those needed for a conventional external calibration (unless a one-point calibration is carried out). The advantage of obtaining multiple signals from every aliquot replaces the need to prepare and measure many standards.

This approach was labelled multi-energy calibration (MEC) and it has been used for atomic emission techniques such as inductively coupled plasma optical emission spectrometry (ICP OES),[10] microwave-induced plasma optical emission spectrometry (MIP OES)[10,11] and laser-induced breakdown spectrometry,[12-16] as well as for atomic absorption processes, namely high-resolution continuum source flame atomic absorption spectrometry (HR CS FAAS),[10] high-resolution continuum source molecular absorption spectrometry (HR CS MAS)[17] and molecular absorption in the ultraviolet-visible region of the spectra, in addition to fluorescence.[18]

The same principle has also been applied to inductively coupled plasma mass spectrometry (ICP-MS) by monitoring different isotopes from the same element,[19,20] and then it has been referred to as multi-isotope calibration. Moreover, since not all elements possess various stable nuclides, the use of a reaction cell to form and measure different adducts from the only nuclide available in such cases has also been proposed, taking advantage of the potential of inductively coupled plasma tandem mass spectrometry in this regard.[21,22] This certainly represents an innovative approach to further expand the use of this calibration approach, and then it has been named as multispecies calibration.[23]

Most of these papers demonstrate the application of this multi-signal calibration concept to develop applications with different techniques, further proving its promising performance. However, owing to its novelty, there is a lack of fundamental knowledge regarding its optimal use. For instance, as will be shown in section 3.1.1, the relationship between the slope of the regression and the concentration of the analyte is not linear, which implies that the amount of spike added may play an important role in terms of precision and accuracy.

A very recent work by Virgilio *et al.* has investigated some of these fundamental aspects, namely how to properly calculate the limits of detection (LOD) and quantification (LOQ) as well as indicating a working range for the slope in which good accuracy and precision are expected.[24] While this is a welcome addition, we believe there are still fundamental aspects that require further investigation for an optimal application of the methodology to each particular situation.

In our view, one of the techniques that can benefit more from the use of this intriguing calibration strategy is HR CS MAS in general and, in particular, when graphite furnace is used (HR CS GFMAS) as vaporizer.[25,26] The reason for this is that such technique is very prone to suffer from chemical interferences deriving from the presence of other elements in the sample. Generally, the vaporization process is often not as straightforward as a pure atomization process mostly based on temperature, and the presence of many other species may result in the formation of other compounds different from the targeted one.[27,28] Interestingly, while commercially available HR CS AAS instrumentation offers the potential to monitor only a narrow part of the spectrum simultaneously, which affects the multi-element possibilities of the technique,[29,30] when molecular species are measured different rotational or vibrational transitions superimposed to the electronic transitions are monitored,[31,32] and the resolution of the instrumentation is often sufficient to resolve such transitions. In other words, when HR CS MAS is used, often many lines can be fully simultaneously monitored, which can make MEC an ideal strategy to minimize matrix effects as well as to increase sample throughput. In this aspect, MEC has only been applied to HR CS MAS once, when Vieira *et al.*[17] studied the determination of N, P and S in fertilizers (N and P) and commercial salts (S and N) by HR CS FMAS *via* the measurement of the

molecules NO, PO and CS, respectively, and the determination of Cl in milk *via* the measurement of CaCl by HR CS GFMAS, with positive results.

This study has selected the CaBr molecule to develop a method for the determination of Br using HR CS GFMAS, with the goal to discuss fundamental aspects related with the application of MEC as calibration approach (error propagation as a function of the slope selected, selection of lines, linearity and calculation of LODs) when such technique is applied. Moreover, another different approach, similar to MEC in terms of the aliquots that need to be measured, but different in terms of data processing is introduced. This new strategy can be considered as inspired by isotope dilution as it is also based on calculating ratios (see section 3.1.2.), and the name proposed for it is multi-energy ratios (MER).

The selection of both Br as analyte and of CaBr as target molecule where certainly not fortuitous. The formation of this molecule or of any other Br molecule is easily affected by chemical interferences,[27,33] so it is a challenging problem to solve with MEC or MER approaches, as will be discussed. Moreover, CaBr offers transitions of different characteristics in two different spectral regions, such that pros and cons of these two approaches can be properly evaluated.

- **I.2. Experimental**

I.2.1. Instrumentation

All the measurements were carried out using a contrAA 800G high-resolution continuum source atomic absorption spectrometer (Analytik Jena AG, Jena, Germany) equipped with transversally-heated graphite tube atomizers that incorporated a platform (Analytik Jena AG). The main details about this type of instrument can be found elsewhere.[25] The samples and reagents were pipetted automatically with an autosampler ASGF (Analytik Jena AG).

I.2.2. Standards, reagents and samples

The solutions were prepared with reagents of analytical grade or higher purity. Deionized water purified by a Milli-Q system (Millipore, Bedford, USA) was used for the solutions. Nitric acid 65% Suprapur® (Merck, Darmstadt, Germany) was diluted to 1% v v^{-1} to prepare the chemical modifier and molecule-forming reagent solutions.

A 1000 mg L^{-1} Br standard (Merck) was used to prepare all the Br aqueous standard solutions, as sample and/or spike. A Pd standard solution 10 g L^{-1} (Merck) was diluted in order to achieve a final mass of 30 μg (5 μL of 6 g L^{-1} Pd solution). Calcium carbonate with purity of >99.0% (Sigma-Aldrich, St. Louis, USA) was dissolved in HNO_3 1% v v^{-1} until a final concentration of 3% m v^{-1} Ca was obtained, then 5 μL were pipetted together with the sample and chemical modifier (150 μg Ca). The interference study was carried out by proper dilutions of a Cl standard solution 1000 mg L^{-1} (Merck).

The certified reference material (CRM) of water Anions - Whole Volume QC3060 (Lot#LRAB9707, Sigma-Aldrich) was analyzed to evaluate the accuracy of the method and the impact of interfering species.

I.2.3. Measurement conditions

Two CaBr vibronic transitions were monitored, $X^2\Sigma \rightarrow A^2\Pi$ (0,0) and $X^2\Sigma \rightarrow B^2\Sigma$ (1,0), around 625.0 and 600.5 nm, respectively. Preliminary tests comparing peak height and peak area, with 1, 3 or 5 detector pixels in both cases, showed that using 5 pixels and measuring peak areas (integrated absorbance) resulted in better linearities obtained *via* MEC. Thus, such approach was selected for this study.

For all the measurements, unless otherwise noted, the temperature program and general conditions of the graphite furnace were adapted from Flórez & Resano[33] and are shown in **Table 1**. Several peaks (wavelengths) of both transitions were evaluated, so they were named after their detection pixel for practical purposes, as shown in **Table 2**. **Figure 1** shows the spectra (average of 68 spectra obtained during 5 s of detection time) of the CaBr diatomic molecule at both wavelengths, labelling the peaks studied with their respective detection pixel.

Table 1. HR CS GFMAS conditions for the determination of Br *via* the monitoring of CaBr.

Vibronic transition / Central pixel wavelength	$X^2\Sigma \rightarrow A^2\Pi$ (0,0) / 624.997 nm
	$X^2\Sigma \rightarrow B^2\Sigma$ (1,0) / 600.492 nm
Number of detector pixels	5 (CP±2)
Sample volume / μL	10, 20*
Chemical modifier	Pd (30 μg)
Molecule-forming reagent	Ca (150 μg)

Temperature program

Step	**Temperature / °C**	**Ramp / °C s^{-1}**	**Hold / s**	**Ar gas flow / L min^{-1}**
Drying	90	5	20	2.0
Drying	120	5	30	2.0
Pyrolysis	1000	50	20	2.0
Gas adaption	1000	0	5	0.0
Vaporization	2100	3000	4-6**	0.0
Cleaning	2500	500	4	2.0

*used for the determination of Br in the CRM QC3060

** The signal is integrated during the first 2 seconds

Table 2. Relation between the detection pixel number and the wavelength for the vibronic transitions $X^2\Sigma \rightarrow A^2\Pi$ (0,0) and $X^2\Sigma \rightarrow B^2\Sigma$ (1,0) of the CaBr diatomic molecule.

Transition $X^2\Sigma \rightarrow A^2\Pi$ (0,0)		**Transition $X^2\Sigma \rightarrow B^2\Sigma$ (1,0)**	
Pixel	**Wavelength / nm**	**Pixel**	**Wavelength / nm**
40	624.685	11	600.115
46	624.714	20	600.153
54	624.753	44	600.253
63	624.797	51	600.283
74	624.850	59*	600.321
86	624.909	68	600.354
100	624.972	74	600.379
114	625.045	84*	600.426
131	625.128	94	600.463
149	625.211	100	600.488
168	625.315	109	600.526
		122	600.580
		127	600.601
		136	600.639
		143	600.668
		151	600.701
		165	600.760
		175	600.802
		183	600.835

*Overlapped peaks

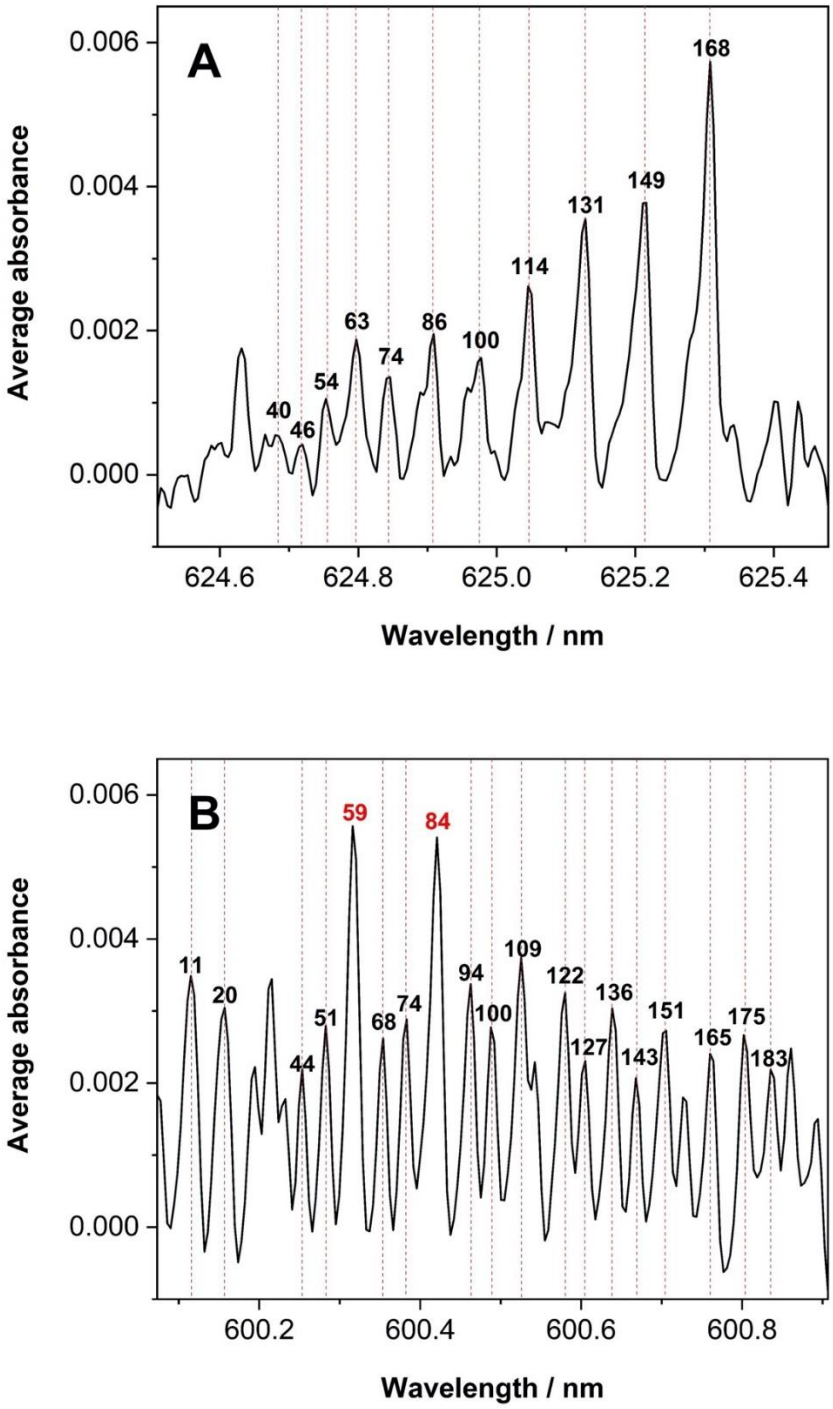

Figure 1. Spectra of the CaBr diatomic molecule (A) in the vicinity of 625.0 nm, as obtained with 30 ng Br; and (B) in the vicinity of 600.5 nm, as obtained with 100 ng Br. The numbers over the peaks correspond to the detection pixel at a

specific wavelength (see **Table 2**). Graphite furnace conditions are listed in **Table 1**.

- **I.3. Results and discussion**

I.3.1. Theoretical background

I.3.1.1. Multi-energy calibration (MEC)

Multi-energy calibration is a novel calibration approach that has been proposed by Virgilio *et al.*[10] for use in optical spectrometry. The calculations corresponding to such approach can be explained as follows: considering the general correlation found in spectrometric techniques, at a specific wavelength (λ_i), the analytical signal $I(\lambda_i)^{Sam}$ is linearly proportional, by the proportionality constant *m*, to the analyte concentration C^{Sam}, as written in equation 1. Obviously, the addition of a spike C^{Std} results in an increase in the analyte level and the instrumental response should also vary accordingly, $I(\lambda_i)^{Sam+Std}$ (see equation 2).

$$I(\lambda_i)^{Sam} = mC^{Sam} \quad (1)$$

$$I(\lambda_i)^{Sam+Std} = m(C^{Sam} + C^{Std}) \quad (2)$$

Combining both equations 1 and 2, equation 3 is obtained, which relates the analytical signal of a sample and a spiked sample with the concentration of the analyte in the sample and in the spike. This equation is convenient because this relation is true when measuring different transitions, occurring at different wavelengths, which possess different sensitivities. Therefore, if the sample and sample+standard can be measured at different wavelengths, and their data are plotted as $I(\lambda_i)^{Sam}$ *versus* $I(\lambda_i)^{Sam+Std}$, a linear plot should be obtained with a slope S equal to ($C^{Sam}/C^{Sam} + C^{Std}$), as shown in equation 4. Rearranging such equation, equation 5 is obtained, which expresses the concentration of the

sample as a function of the slope (measurable) and the concentration of the spike (which should be known in advance).

$$I(\lambda_i)^{Sam} = I(\lambda_i)^{Sam+Std}\left[\frac{C^{Sam}}{C^{Sam} + C^{Std}}\right] \quad (3)$$

$$Slope = S = \frac{C^{Sam}}{C^{Sam} + C^{Std}} \quad (4)$$

$$C^{Sam} = \frac{SC^{Std}}{(1 - S)} \quad (5)$$

The previous works about MEC usually mix sample+blank (1:1) to balance the dilution originated when the spike is added (1:1). This strategy is useful because the addition of a spike solution into the sample leads to a dilution of the latter. Therefore, if the same volume of both blank and spike solutions is added to the sample, the dilution would be the same in both cases, making it possible to carry out a straightforward calculation, as shown in equation 5.

However, this is not an issue for HR CS GFMAS because this technique typically uses a known-volume. Therefore, it is possible to use the equation 5 also for masses instead of for concentrations. In this work, the amount of analyte (bromine) will be given as mass, although the terminology C^{Sam} and C^{Std} will be maintained for simplicity. Thus, in the current work, the blank was measured separately and subtracted from the sample and sample+standard analytical signals.

Since the relation evaluated by MEC is the instrumental intensity of the sample *versus* the intensity of the sample+standard, the slope values should be between ~0 (infinite amount of spike added) and ~1 (infinitesimal amount of spike added). In this context, one could predict the theoretical bias of the concentration finally obtained as a function of the deviation of the slope experimentally calculated.

Such deviation can be expressed as the absolute slope measurement error, e_S, which ultimately contributes to the deviation of the C^{Sam} calculation, e_C, as described in equation 6.

$$(C^{Sam} \pm e_C) = \frac{(S \pm e_S)C^{Std}}{[1-(S \pm e_S)]} \quad (6)$$

The theoretical value of C^{Sam} is obtained when $e_S = 0$, *i.e.*, the relation between C^{Sam} and C^{Std} is exactly (S/1–S). Assuming that the variations of C^{Std} are practically negligible, then the deviation when calculating C^{Sam}, *i.e.* e_C, exists due the deviation in the estimation of S, *i.e.* e_S, as detailed in equation 6.

Therefore, it is possible to estimate how the e_S value will affect the concentration bias with equation 7. Basically, the bias reflects the difference between theoretical and experimentally obtained values for (S/1–S), which directly translates into a difference of C^{Sam}. Thus, the % of bias for C^{Sam} can be written as:

$$bias^{\pm}_{C^{Sam}}(\%) = \frac{\left\{\frac{(S \pm e_S)}{[1-(S \pm e_S)]}\right\} - \left(\frac{S}{1-S}\right)}{\left(\frac{S}{1-S}\right)} \times 100\% \quad (7)$$

It can be noticed (see equation 6) that the upper limit of e_S value will lead to the upper limit of e_C and concentration bias, e_C^+ and $bias^+_{C^{Sam}}$, respectively. Thus, equation 7 can be further developed into equation 8 (see Supplementary information for more details).

$$bias^+_{C^{Sam}}(\%) = \frac{e_S}{S(1-S-e_S)} \times 100\% \quad (8)$$

The lower limit, $bias^-_{C^{Sam}}$, can be calculated analogously, resulting in equation 9 (see Supplementary information). Both equations 8 and 9 can be unified and they become equation 10, which enables the calculation of both the upper and lower concentration biases, just applying "+" (for the upper limit) or "–" (for the lower

limit) where "$\pm$" is indicated. For instance, a 5% deviation of the slope, for a slope value of 0.5 (thus S=0.5 and e_S = 0.025) will ultimately result in a concentration bias of 10.5% and –9.5% (depending on whether the deviation is positive or negative, respectively). It is noteworthy that the relation between e_S and $bias^{\pm}_{C^{Sam}}$ is neither linear nor symmetric.

$$bias^{-}_{C^{Sam}}(\%) = \frac{-e_S}{S(1-S+e_S)} \times 100\% \qquad (9)$$

$$bias^{\pm}_{C^{Sam}}(\%) = \frac{\pm e_S}{S(1-S\pm e_S)} \times 100\% \qquad (10)$$

Figure 2 shows the effect of the S value on the calculation of the analyte concentration. All the data of **Figure 2** was obtained theoretically using equation 10. Three deviations of the true slope are displayed for comparison, representing 1, 5 and 10% of deviation. It is evident that high slope values will lead to greater concentration bias, *e.g.*, for slope of 0.7, a 10% deviation in the experimental calculation of such parameter leads to a difference of approx. 43% in terms of concentration. **Figure 2** shows the curves up to a slope of 0.8 only, because the concentration bias grows substantially for higher values when a 10% deviation in the calculation of the slope is assumed: for a slope of 0.90, the concentration bias rises up to 1000%. In fact, for high deviations and high slopes the model proposed in equation 8 will eventually fail, as the denominator (1 – S - e_S) may become negative, which makes no sense as such error is defined as positive.

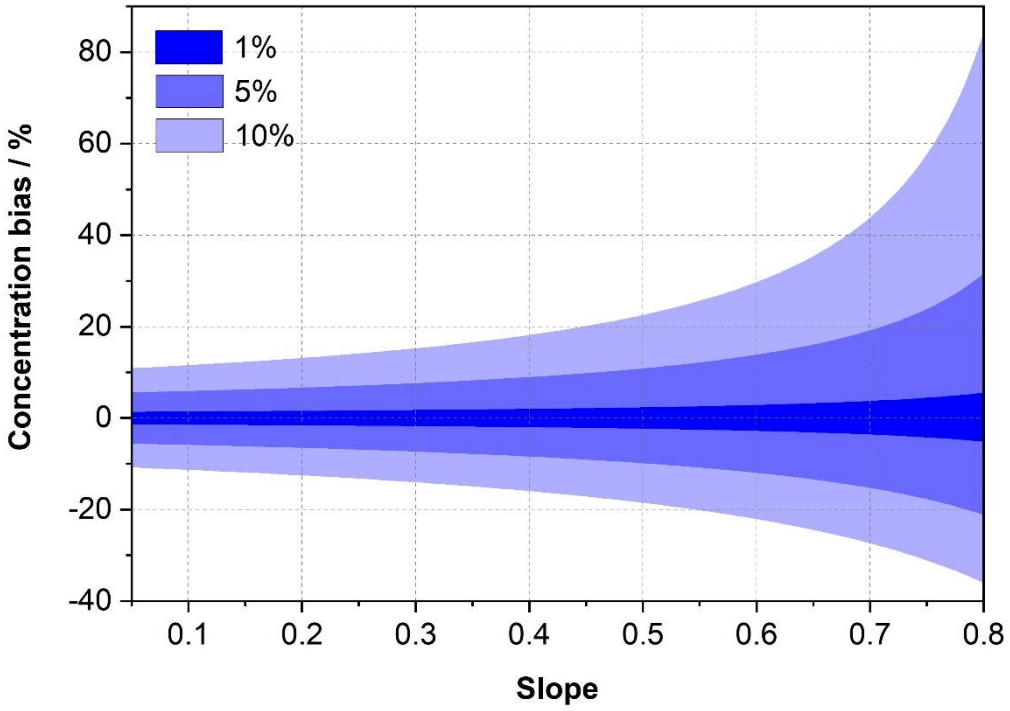

Figure 2. Theoretical relation between different deviations from the true slope (1, 5 and 10%, with different shades of blue) and the final bias in the concentration calculated using MEC.

In any case, this extremely high deviations for high slopes can be explained simply by analyzing equation 5, because as the slope gets closer to 1, the value (1-S) gets closer to zero and any small difference in the estimation of S leads to a large difference in terms of (S/1–S). For instance, for a true value of 0.9, obtaining a calculated value of 0.909 represents a difference of only 1%. However, this variation will lead to a (S/1–S) value of 9.99, instead of the true value of 9. Thus, a difference of only 1% is transformed into a final difference of 11% in terms of (S/1–S). Therefore, when designing the experiments with high S values, higher deviations are expected, which would lead to inaccuracies if only

one replicate is performed, and to higher irreproducibility when several replicates are carried out.

Figure 2 suggests that using lower slopes (when the amount of analyte in the spike is several times higher than in the sample) would be recommended because the bias will be lower, which in theory is correct. However, such situation could lead to another source of error. For low slopes, the concentration of the analyte in the sample gets to be so low that it shows a minimal influence on the analytical signal, which is certainly not desirable. This effect will be further discussed in Section 3.2. Virgilio *et al*.[24] recently shown experimentally that use of "extreme conditions" for the slope ($\leq$0.1 or $\geq$0.9) results in lower trueness.

Clearly, the deviation of the MEC slope can lead to a miscalculation of the analyte concentration, as it also occurs for other more conventional calibration strategies. However, MEC also presents another issue that should be considered carefully. The concept of MEC is to plot a graph of instrumental responses (analytical signals), sample (y-axis) *vs*. sample+standard (x-axis), measured at different wavelengths and use linear regression to calculate the slope, which is later substituted in equation 5 to calculate the sample concentration. Therefore, the variables represented in both graph axes show uncertainties associated with the measurements when using MEC, unlike what occurs in a conventional calibration, where the error in the x-axis (mass or concentration) can be considered as negligible.[3] Thus, choosing a suitable linear regression model seems recommended. In this work, the software Origin 2019b was used to calculate the MEC slope and its standard deviation (which can be readily applied for calculating the standard deviation of the analyte content) with a linear fit with

x error mode, which minimizes the sum of square of error on both x and y directions, also known as York Method.[34]

I.3.1.2. Multi-energy ratios (MER)

For MEC, the relation of the analytical signal at different wavelengths with the concentration is described in equation 3, from which equation 5 is derived. Another way to process the data is also possible for which we propose the name of multi-energy ratios (MER). Instead of a linear regression, a direct ratio between both intensities can be calculated. The concentrations will now be related to the ratios (R) of the analytical signals measured at every wavelength (equation 11). Equation 12 can be derived from equation 11, showing that both ways to process the data, either using the slope (equation 5) or the (equation 12) ratio, are analogous, simply changing the way in which the same data is processed. Therefore, all the considerations made for MEC in Section 3.1.1 are also valid for MER.

$$\frac{I(\lambda_i)^{Sam}}{I(\lambda_i)^{Sam+Std}} = R = \frac{C^{Sam}}{C^{Sam} + C^{Std}} \qquad (11)$$

$$C^{Sam} = \frac{RC^{Std}}{(1-R)} \qquad (12)$$

Figure 3 shows an example of the same experimental data treated by both methods, MEC and MER. The measurements of 11 transitions were evaluated, from 624.510 to 625.478 nm (pixels 40, 46, 54, 63, 74, 86, 100, 114, 131, 149 and 168, see **Figure 1A** and **Table 2** for more information). The x-axis of **Figure 3B** shows the detection pixels instead of the wavelengths for practical purposes. In this study, the sample was 10 μL of a 3 mg L^{-1} Br standard solution (30 ng Br) and the sample+standard was 20 μL of the same solution (60 ng Br), representing

the addition of 10 μL of spike of 3 mg L^{-1} (Br-spike mass 30 ng). The instrumental conditions used are shown in **Table 1**.

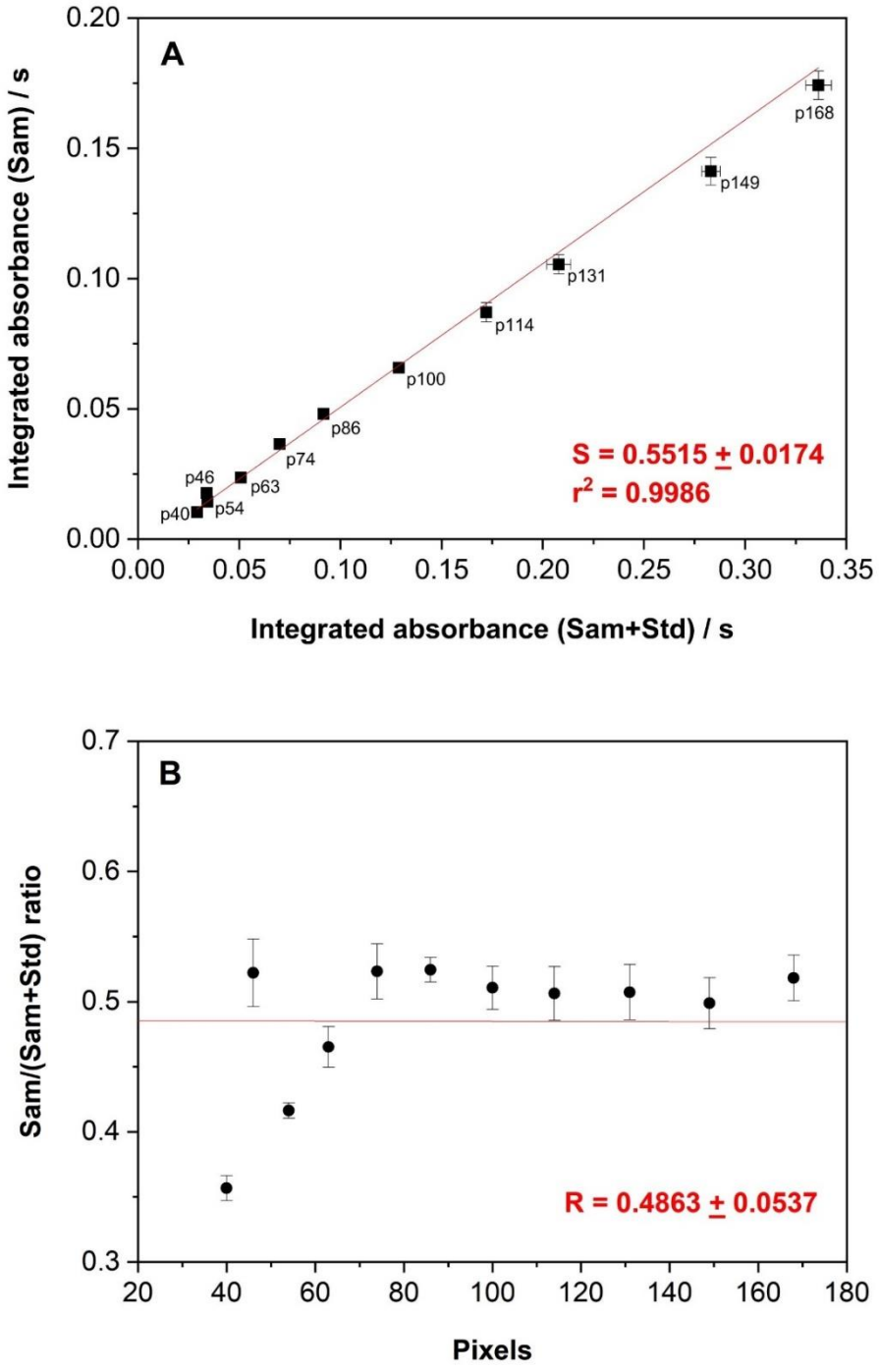

Figure 3. Experimental data (11 transitions) obtained for 30 ng Br as sample and 30 ng Br as spike using HR CS GFMAS for the monitoring of CaBr in the vicinity of 625 nm with (A) MEC and (B) MER strategies. Error bars correspond to the

standard deviation (n=3). The labels shown in Figure 3A correspond to the pixels measured

MEC shows good correlation among the data, $r^2 = 0.9986$, and a slope of 0.5515 is calculated with such approach, which deviates by approx. 10% from the theoretically expected slope (0.5). Applying equation 5, the Br sample mass calculated is 36.9 ± 2.6 ng (average value ± standard deviation), which is 23% biased from the actual mass of 30 ng. On the other hand, the average ratio of all 11 transitions was found to be 0.4863, which applying the MER approach results in a value of 28.9 ± 5.4 ng, a 3.6% difference only from the true mass.

One of the advantages of using the MEC strategy is the possibility to detect and eliminate outliers.[10] Visualizing the residual data plot of **Figure 3A**, it is possible to remove the data from pixels 46, 149 and 168, which would lead to a new linear correlation of $r^2 = 0.9975$ and a slope of 0.5670 ± 0.0157. In this case, the calculated Br mass of the sample will be even higher, 39.3 ± 2.5 ng. On the other hand, a conventional linear regression using direct weighing errors with all the 11 transitions was also performed, and in that way MEC leads to a $r^2 = 0.9984$ and a slope of 0.5146 ± 0.0070, and an ultimate Br value of 31.8 ± 0.9 ng. Although in this case this simpler linear regression model provides a slope-value that, calculating the concentration, is less biased, we still propose and will use for further data analysis (unless otherwise noted) a regression model that considers the contribution in terms of uncertainty of both axes for calculating the best linear correlation, as it is more correct considering that in both axes absorption measurements are plotted.

But outliers can also be detected with ease using MER. Evaluating the data for MER in **Figure 3B**, it is clear that the pixels 40 and 54 are far off the ratio average: they differ by 26.6% and 14.4%, respectively, from 0.4863. If they are considered as outliers, the resulting average ratio is 0.5085 ± 0.0194, equivalent to a Br mass of 31.1 ± 2.2 ng. It can be noted that the values obtained with or without outliers do not differ significantly from the theoretical value of 30 ng (Student's t-test, t_{exp} = 0.676 < t_{crit}95% = 2.228, n=11; t_{exp} = 1.500 < t_{crit}95% = 2.306, n=9). Moreover, there is no significant difference between the mean results obtained in both cases (Student's t-test, t_{exp} = 1.232 < t_{crit}95% = 2.145, degrees of freedom = 14, two tails, different variance), but a much better precision is achieved if these two values are rejected (Fisher's test, F_{exp} = 6.025 > $F_{crit95\%}$ = 4.295, two tails).

Overall, removing outliers is possible with both approaches but it is important to emphasize that they are not going to influence MEC and MER results to the same degree. In any case, robust statistical approaches that are less affected by the occurrence of outliers are available both for performing regressions and for calculating the most representative value of a group of data, but it is out of the scope of this paper to further discuss such topic.

Both strategies, MEC and MER, represent different ways to extract analytical information from the same set of data and their distinct behavior will be further investigated in this work.

I. 3.2. Monitoring CaBr around 625 nm: different intensity transitions

As discussed in section 3.1.1., there is an analytical limitation when low- or high-value slopes are used for MEC and, due to the similarity of the equations, MER should be influenced by these extreme values as well. Therefore, it is important to verify this behavior experimentally.

The first experiment consisted in evaluating the RSD obtained for the final Br concentration by measuring a blank solution, in order to subtract its values at each studied wavelength (pixel), and ten different Br masses: 10, 20, 30, 40, 50, 60, 80, 100, 120 and 150 ng (10 μL of standard solutions diluted accordingly). All measurements were done in triplicate. The data was treated as follows: assuming 10 ng Br is the sample, thus 20 ng Br could be treated as 10 ng Br sample +10 ng Br spike. This is equivalent of using MEC or MER with a theoretical value S = R = 0.5. Moreover, 20 ng Br could be treated as a sample and compared with 30 ng Br (10 ng Br spike), with a theoretical S and R of 0.667, and so forth. All the possible combinations were evaluated for both MEC and MER and the results are shown in **Figure 4**. The slope and ratio axes use logarithm scale for better visualization of lower values. In **Figure 4B** a column goes out of scale, with an RSD of 117% (sample Br mass 50 ng with R = 0.833), but the maximum of the z-axis was set at 50% in order to use the same axis for both Figures 4A and 4B, thus enabling an immediate comparison.

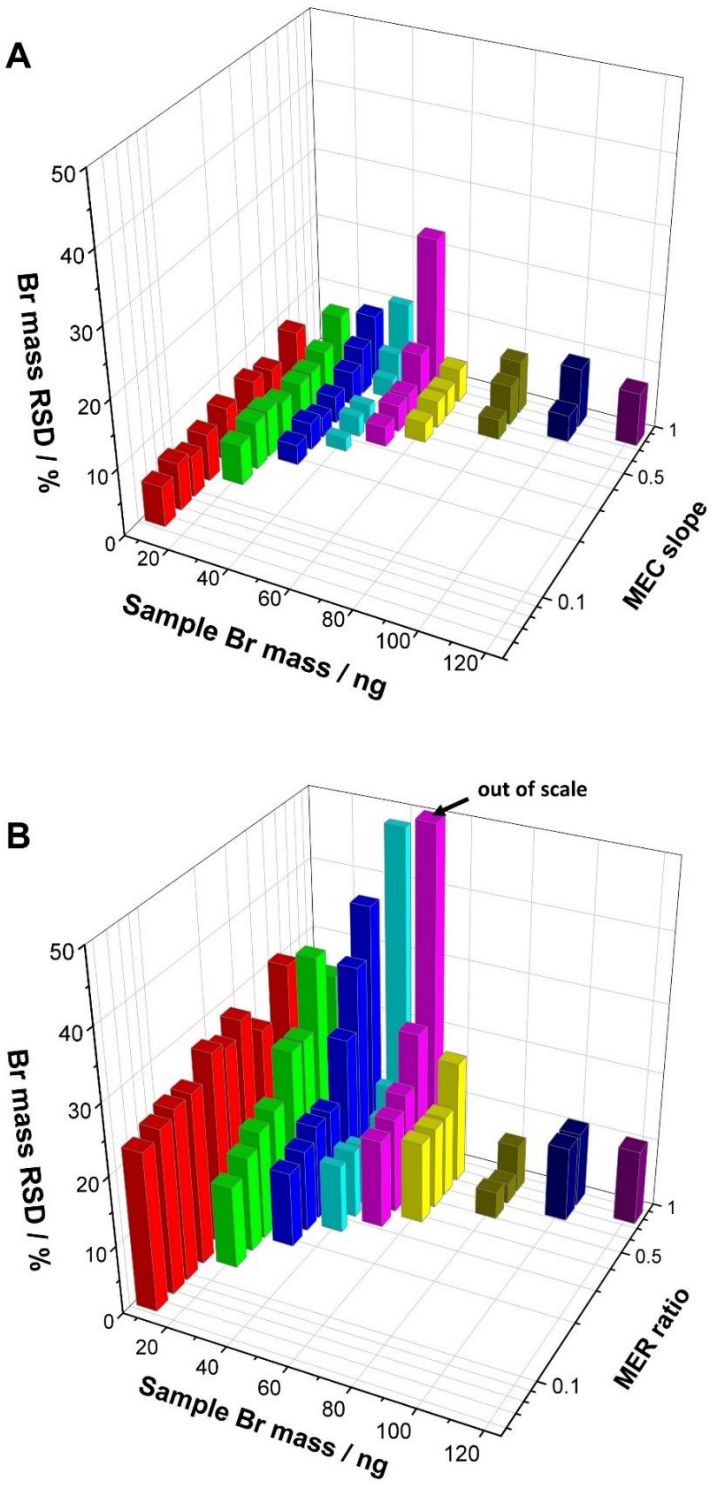

Figure 4. Evaluation of the RSD of the Br masses calculated from standard solutions containing Br ranging 10 to 120 ng with different (A) slopes and (B) ratios using MEC and MER, respectively. In Figure 4B, the RSD value for sample Br mass 50 ng with 0.833 ratio is out of scale (actual value,117%).

Both strategies show a similar behavior: for all the Br mass studied, there is an increase in the final RSD at higher slope or ratio values. This fact agrees well with the theoretical values discussed previously for MEC (see **Figure 2**). A quite constant value of RSD through all the slope and ratios was obtained for 10 ng of Br because for low slope or ratio values only slight variations are found (as discussed before, the content of the sample hardly influences the signal). The RSDs are generally higher for low sample Br masses due to their proximity to the limits of detection (LOD). The transitions with lower intensities are more prone to be influenced by the instrumental noise and/or baseline fitting, which increase the uncertainty of the measurement at low Br masses.

It is also clear that the RSD is usually higher for MER than for MEC. MER weighs all the ratios equally, thus it is more sensitive to suffer from outliers, if no values are excluded. However, MER also provides an intuitive way to understand all the potential issues, as shown in **Figure 5**. **Figure 5A** shows the results for a Br mass of 30 ng in a sample with different spikes (10, 20, 30, 50, 70, 90 and 120 ng Br), and it plots the Br mass finally obtained using MEC versus the slope calculated experimentally. In this example, as predicted, the use of lower slopes results in lower RSDs (error bars show the standard deviation). However, such low slopes are also accompanied by a higher deviation from the true value. This effect was commented in Section 3.1.1., that lower slopes/ratios values could lead to poorer accuracy due to the non-optimal relation between sample and spike. The same effect is observed in other strategies such as standard addition and isotope dilution, where it is well-known that the relation between spike and sample contents should be close to one, if possible.

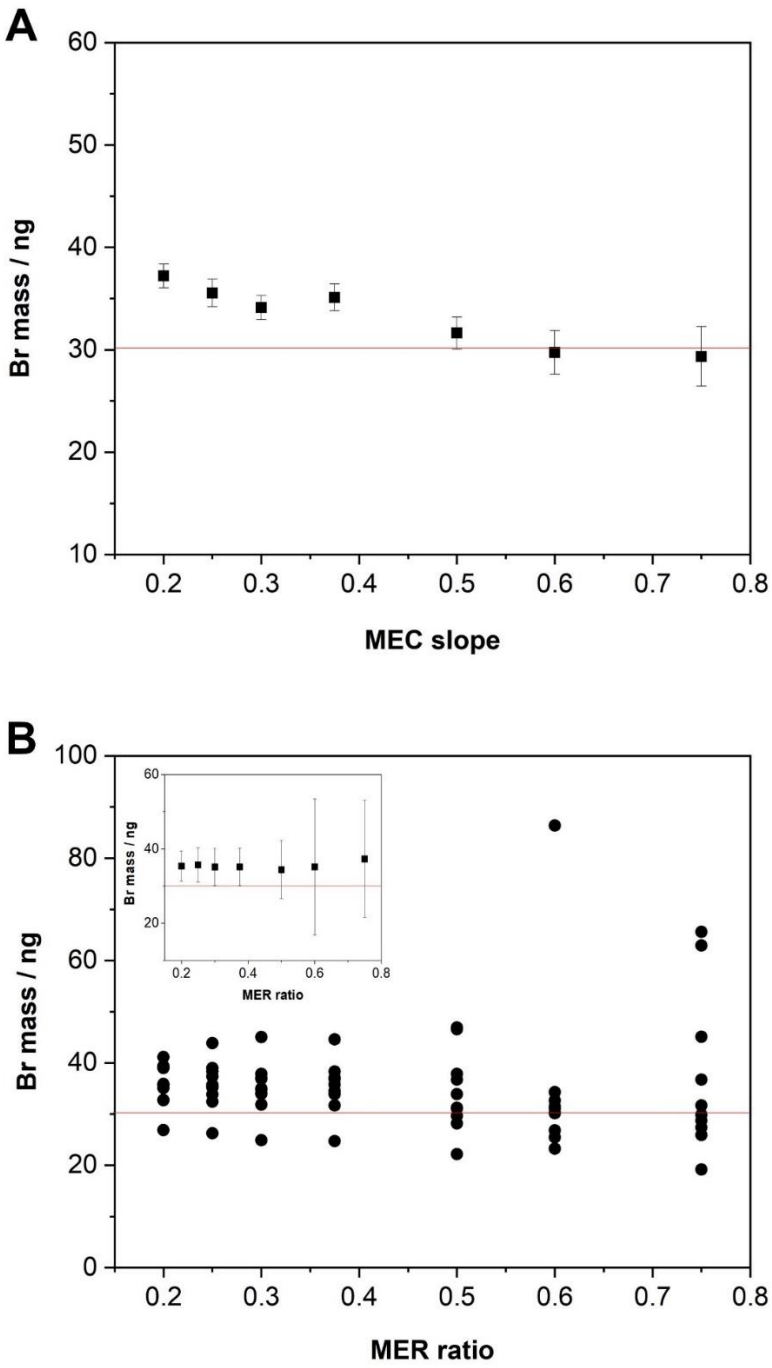

Figure 5. Br determination (true mass 30 ng) through (A) MEC and (B) MER at different slopes/ratios. Each data of Figure 5B shows the mean value for each one of the transition evaluated. The small graph inside Figure 5B shows the overall mean value of all the transitions with its uncertainty. The red line corresponds to the real value (30 ng). The error bars correspond to the standard deviations (n=3).

For MER, a similar trend can be seen for the ratios: use of higher values lead to higher uncertainties, (see the small graph inside **Figure 5B**). However, if each individual value (the ratio of each transition) is plotted (see **Figure 5B**), it is possible to visualize a zone with a high-density of similar ratios (similar Br mass). If only those values are selected, the final results will be closer to MEC results. Moreover, observing R = 0.6, the Br mass is 35.2 ± 18.3 ng considering all the data. Obviously, there is an outlier with a value of approximately 85 ng, 2.5 times higher than the average and exceeding the average value plus 2 standard deviations. Eliminating this data with a Dixon's Q test (Q_{exp} = 0.825 > $Q_{crit95\%}$ = 0.466, n=10), the final value changes to 29.5 ± 3.6 ng, which obviously represents much better accuracy and precision. As discussed before, we do not want to complicate too much this topic and to carry out any unfair comparison, but simpler robust estimators (use of median and quartiles; use of the trimmed mean and the robust standard deviation) could and probably should be used for MER instead of relying on tests to reject outliers.

In conclusion, while Virgilio *et al.* recommended using slope values between 0.1 and 0.9 for MIP OES, ICP OES and ICP-MS,[24] it seems advisable to limit this range more and use values between 0.5 and 0.6 in the case of monitoring CaBr using HR CS GFMAS for both MEC and MER strategies to guarantee a well-balanced relation between accuracy and precision.

I.3.3. Effect of analyte-mass linearity for MEC and MER. Figures of merit

It is already well-known that AAS and MAS measurements obey the Lambert-Beer Law, but only for a relatively narrow range of masses. A linear relation between the analytical signal and the analyte mass can be established for one, or maximum two orders of magnitude. It is already well-established what this concept means when external calibration is deployed (*e.g.* need for diluting samples that provide a signal outside the linear range): However, it is necessary to also discuss what this fact represents when trying to use MEC or MER.

Figure 6 shows the response of the HR CS GFMAS instrument (integrated absorbance) for several masses of Br, between 20 and 400 ng (n=8), monitoring CaBr molecule, at the 11 transitions evaluated in the previous sections around 625 nm. The calibration curves for the most sensitive transitions show linearity until approximately 120 ng (other experiments show that 150 ng is still a safe value) and they lose linearity for a higher Br mass. Less sensitive transitions seem to show linearity in other ranges,[33] from 120 or 200 to 400 ng and probably more, but notice that such linearities (*e.g.*, from 200 to 400 for pixels 131, 114 and 100) do not necessarily go through the intercept. That means that this second range of linearity could be used for external calibration,[35] but not for MEC or MER as the equations shown in sections 3.1.1 and 3.1.2 will not be valid.

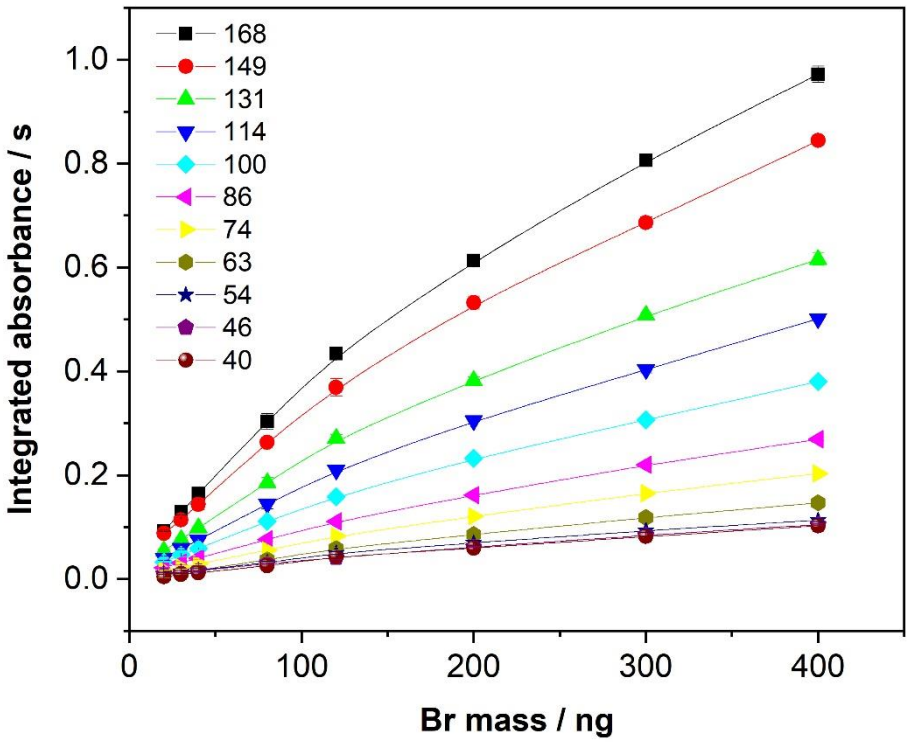

Figure 6. Calibration curves (Br values ranging from 20 to 400 ng) when monitoring the CaBr molecule using HR CS GFMAS. The numbers of each calibration curve correspond to the detection pixels (wavelength) used to obtain the integrated absorbance (CP±2) of different rotational contributions of the vibronic transition $X^2\Sigma$ – $A^2\Pi$ (0,0). Error bars correspond to the standard deviation (n=3).

It is thus important to stress that lack of linearity may affect the determination of the analyte concentration by MEC and MER. Both methods rely on a linear and constant relation between the analyte and the instrumental signal regardless of the amount, *i.e.*, if one of the contents falls outside of the linear range, the calculations should be incorrect, as both contents (sample, and sample plus spike) will obey to different analyte *vs*. mass relations. The fact that the linear

range may be different for different transitions may be taken into account when designing the experiments, and eventually may minimize the number of transitions that should be used for a particular analyte amount.

Another limitation for using some lines depending on the analyte amount is the limit of quantification (LOQ). The traditional method for calculating LOD and LOQ is three and ten times the standard deviation (SD) of ten measurements of blank divided by the calibration curve slope, respectively. Using this approach, the LOD and LOQ of each wavelength (pixel) previously studied were calculated and the results are shown in **Table 3**, labelled as external calibration (EC). The LOD of pixel 168 which corresponds to the wavelength 625.315 nm, the usual analytical line studied for Br determination *via* CaBr molecule, was 3 ng, comparable to the values found in the literature for such transition (between 2.0 and 5.4 ng),[33,36,37] all higher than the value of 78 pg achieved by Limburg & Einax.[38]

Table 3. Figures of merit corresponding to the CaBr vibronic transition $X^2\Sigma - A^2\Pi$ (0,0) using HR CS GFMAS. External calibration (the calibration curve covered a Br mass range between 10 and 150 ng) is labelled as EC. Each number besides MER corresponds to the Br mass spike, in ng, used for the calculation of LOD and LOQ. Both EC and MER were evaluated using 11 wavelengths (pixels). n.a.: not applied.

Pixel	LOD; LOQ / ng Br			
	EC	***MER 20***	***MER 80***	***MER 150***
40	40; 135	n.a.	86; 286	54; 181
46	52; 174	n.a.	116; 386	70; 235
54	43; 142	n.a.	89; 297	57; 189
63	53; 178	n.a.	143; 476	82; 274
74	22; 72	15; 50	25; 84	23; 77
86	26; 87	25; 84	34; 115	30; 100
100	17; 55	11; 36	18; 61	18; 59
114	6; 21	3; 10	6; 20	6; 21
131	9; 30	4; 15	9; 30	9; 30
149	4; 14	2; 6	4; 13	4; 14
168	3; 11	1; 4	3; 10	3; 10

LOD and LOQ definitions can also be applied in combination with the MER strategy. A blank signal plus $3SD_{10blank}$ or 10 $SD_{10blank}$ is considered as the signal of the sample, and equation 11 is used to calculate R for each transition and each spike used. Then equation 12 is applied to estimate the LODs and LOQs. These

values are also shown in **Table 3**. Three Br spikes were chosen for this purpose: 20, 80 and 150 ng

Calculating the LOD and LOQ for MEC is, however, not equally straightforward. It requires the calculation of the slope through linear regression, comparing two analytical signals, sample and sample+standard, to later apply equation 5. In this case, the "sample" is the blank solution that by definition is the absence of analyte, *i.e.*, there is practically no analytical signal under normal conditions. In the x-axis, intensity values proportional to the sensitivity of each transition due to the spike (blank+standard) will be plotted, while the y-axis should provide almost random intensity values due to the blank. Therefore, a linear correlation cannot be expected (see **Figure S1**).

Very recently, Virgilio *et al.* have proposed a method for calculating LOD/LOQ for multi-signal calibrations, including MEC.[24] The authors use equation 13 to calculate the LOD/LOQ, where S_{Slope} is the standard deviation of the MEC slope, and N is 3 when calculating the LOD, and 10 for the LOQ. Thus, this strategy was also investigated, and the results are shown in **Table 4**.

$$LOD\ or\ LOQ = N\left(\frac{C^{Std}S_{Slope}}{(1-Slope)^2}\right) \qquad (13)$$

Four different strategies were evaluated with this approach. Calculation by: i) using the 11 transitions around 625 nm (see **Table 2**); ii) using the three most sensitive transitions (pixels 131, 149 and 168); iii) using the same 11 pixels as in i), but considering Slope = 0; and iv) using the same 3 pixels as in ii), but considering Slope = 0. The first strategy is similar to the one proposed by Virgilio *et al.*[24] The second uses equation 13 with the minimum number of different transitions recommended for a MEC analysis, which is three, as discussed by Donati & Amais.[3] The third and fourth ones are estimations based on the following

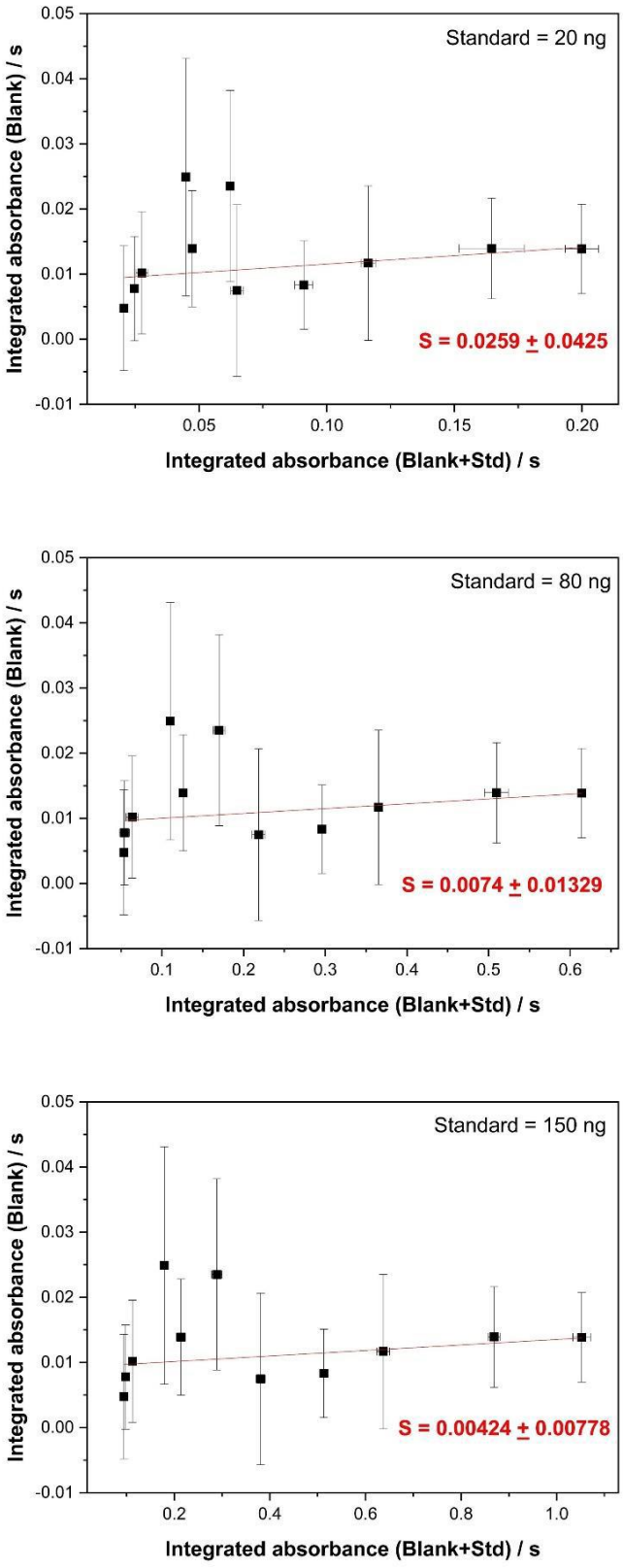

Figure S1. Blank measurements vs. 20, 80 and 150 ng Br spikes using MEC for calculating the LOD and LOQ, as described in equation 13.

concept. As discussed before, MEC should compare two analytical signals, but in this case, one corresponds to a blank solution that shows a random behavior. Thus, the data plotted would hardly follow any linear tendency (see **Figure S1** for examples). It is not evident that the slope resulting from such calculation would possess any physical meaning. Therefore, we assume that a theoretical perfect blank should result in a slope value of zero, and the estimation of LOD/LOQ should only account for the uncertainty of the slope measurement.

As shown in **Table 3**, the LODs and LOQs calculated for MER 80 and MER 150 are, for the most sensitive wavelengths, comparable to those obtained using EC. This can be explained because using the method described for calculating the LOD/LOQ for MER is analogue to using a one-point calibration curve, which would be the spike, since the signal from the blank solution should be negligible in comparison with the signal of the spike. Following the same argument, MER 20 probably has a bit “higher slope” (linearity is never perfect), leading to lower values of LOD/LOQ.

MER 150 shows lower LOD/LOQ values at low-sensitive wavelengths than MER 80. That could have been expected, as higher analytical signals should be less affected by random events. Moreover, comparing the previous strategies for the most sensitive transitions (**Table 3**, pixel 168) with the LOD/LOQ calculated with equation 13 for MEC using first and third strategies, both making use of 11 transitions (see **Table 4**), they are all rather similar.

Table 4. Figures of merit corresponding to the CaBr vibronic transition $X^2\Sigma - A^2\Pi$ (0,0) using HR CS GFMAS and MEC calculated *via* equation 13. N_T represents the number of transitions used for the calculation of the LOD/LOQ, and S is the theoretical value of slope

Br spike / ng	LOD; LOQ / ng Br			
	N_T = 11	**N_T = 3**	**N_T = 11, S = 0**	**N_T = 3, S = 0**
20	3; 9	10; 33	3; 9	10; 32
80	3; 11	13; 43	3; 11	13; 43
150	4; 12	14; 48	4; 12	14; 48

In any case, we believe that calculating LODs and LOQs using the MER approach is always useful to assess which lines should be considered and which rejected as a function of the analyte content. On the other hand, when providing the overall figure of merit, a method should not have various limits, and a suitable strategy to calculate the global LOD and LOQ should be proposed for MER. As mentioned above, Donati & Amais[3] stated that at least three transitions are needed to use MEC, and in this case we will follow the same criteria for MER. Therefore, it is reasonable that the three most sensitive analytical lines should be considered for calculating the overall LOD/LOQ.

Pixel 131 (λ = 625.128 nm) measures the third most sensitive transition in this region, with a relative sensitivity of 58% compared with the highest peak (625.315 nm). However, during the analysis, an unidentified molecule (see **Figure 7**) was observed when only the blank solution was monitored with both chemical modifier (Pd) and molecule-forming reagent (Ca). This molecule was generated only when the graphite furnace was new and calcium was used. Due to the refractory nature

of this molecule (wide-time profile and low intensity), it could be a calcium oxide polyatomic molecule, which has been reported to show a transition at 625.85 nm.[39] The interfering molecule could not be eliminated with background least-square correction, available from the AspectCS software, and it especially hampers the measurement at 625.128 nm. Integrating the first 2 s of signal only minimizes the effect of this overlap for the CaBr analytical signal, an approach that was used throughout this study whenever this interfering molecule was detected. Moreover, it is visible that the baseline in this region (see **Figure 7**) shows a “wavy” profile, which may also influence the determination of peak relations, especially the ones with low intensity. Overall, pixel 114 (λ = 625.045 nm) was used as the third most sensitive line for the current method instead of pixel 131 (λ = 625.128 nm).

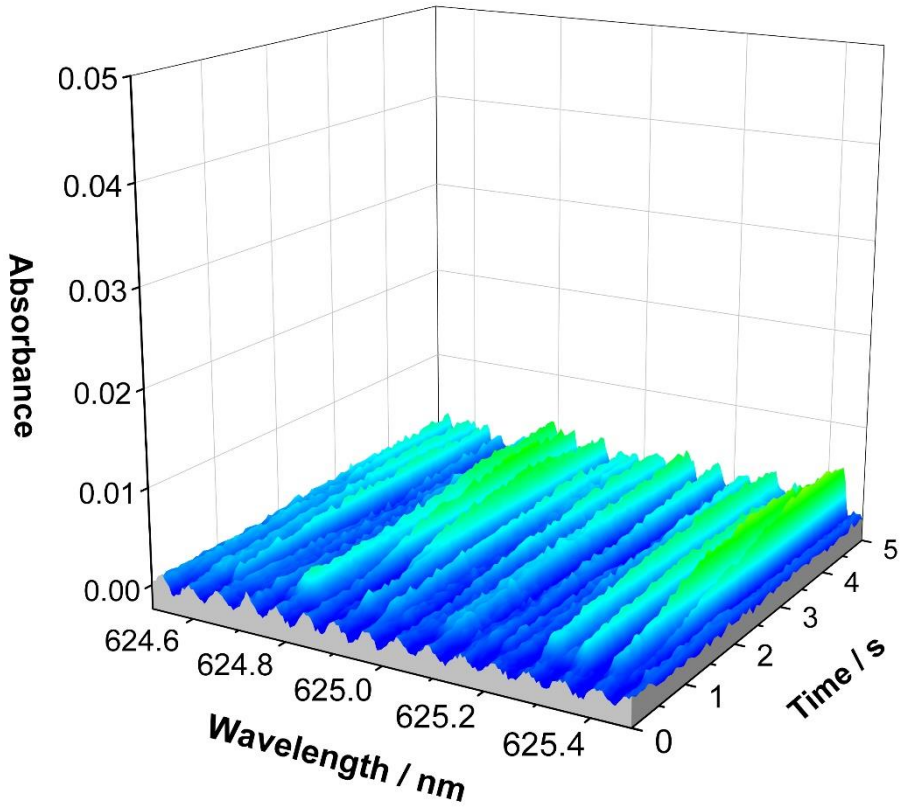

Figure 7. Time- and wavelength-resolved spectrum of the unknown molecular interference appearing in the analytical region around 625 nm.

Obviously, the overall limits are finally restricted by the highest LOD/LOQ values of the three, *i.e.*, pixel 114 at 625.045 nm. Consequently, in this case we propose a LOD and LOQ of 6 ng and 21 ng, respectively, for the MER strategy. Both figures of merit can be calculated directly as explained without needing any external standard calibration to obtain this value. Nevertheless, using lower amount of spike could be a strategy to improve a bit the LOD and LOQ.

Using the same hypothesis for equation 13 (use of the 3 most sensitive transitions only), the values varied from 10 and 33 to 14 and 48 for LOD and LOQ, respectively (see **Table 4**). Assuming a slope value of blank as zero, the limits are practically identical, as the slope is very low in comparison with 1.

In principle, as mentioned by Virgilio *et al.*[24] these multi-signal methods will typically show higher values of LOD/LOQ compared to external standard calibration all things considered, as for EC only the most sensitive line is used and for these approaches more, less sensitive and more noisy lines need to be used. However, the difference between MEC and MER here is that, at least applying the equations proposed in ref. 24, MEC benefits from the use of more transitions as lower LODs and LOQs are provided then (see **Table 4**). This is a bit paradoxical, as those extra transitions added offer poorer sensitivity.

Overall, we would recommend simply using MER for calculating the LODs and LOQs of the lines tested, as such approach provides useful information for selecting the most suitable ones according to the sample concentration. Such criteria will be used in the next sections to select the lines for the determinations intended.

I.3.4. Monitoring CaBr around 600 nm: similar intensity transitions

Considering the results shown in section 3.2., MEC could be considered as a bit more suitable as calibration strategy for CaBr molecule detection using HR CS GFMAS around 625 nm mainly because it leads to lower RSD values. The mean value of Br mass obtained by both MEC and MER are similar, and for both strategies is advisable to work in the vicinity of S = R = 0.5.

However, the vibronic transition studied in that section, $X^2\Sigma \rightarrow A^2\Pi$ (0,0),[39] shows an interesting profile where lines with increasing intensities appear. This is not always the case. For other molecules monitored by HR CS MAS for the determination of non-metals (*e.g.*, CS, widely proposed to determine S,[17,28,40] or PO, used to determine P[17,28,41]) this behavior is not encountered, but instead many lines of similar sensitivity are measured.[42] Interestingly, this other type of

profile can also be investigated measuring CaBr as well. There is another vibronic transition for the CaBr molecule, $X^2\Sigma \rightarrow B^2\Sigma$ (1,0), which appears around 600.24 nm and has been previously explored for isotopic analysis.[43] In this region, all the transitions of CaBr show similar intensities when Br is found in the natural composition (50.7% ^{79}Br and 49.3% ^{81}Br), except for two larger peaks at 600.321 and 600.426 nm where there is an overlap from the transitions of $Ca^{79}Br$ and $Ca^{81}Br$ (thus, practically a double signal is measured; see **Figure 1B** where these overlapped lines are labelled in red). Therefore, this region was studied with MEC and MER to evaluate their performance in this context.

Seventeen peaks were selected between 600.115 and 600.835 nm (all the pixels but the two larger ones; see **Figure 1B**). The temperature and chemical modifiers are the same listed in **Table 1**, and the results are displayed in **Figure 8**.

The small differences on the peak intensities reveal a major effect on the signal relations in MEC (see **Figure 8A**), which was already observed for CS, PO and NO molecules using HR CS MAS with flame as atomizer, as several transitions needed to be excluded to improve the linearity.[17] Overall, there is a linear tendency, $r^2 = 0.9583$, but not all the points follow well the trend, and visually there is no easy criteria to select which outliers could be removed. The problem is that all those points in practice behave like three or four different groups of points, instead of like a high number of points more or less evenly distributed along the line, like in **Figure 3A**. In this case, the theoretical slope and ratio is 0.5. The slope obtained (0.5725 ± 0.0350) resulted in a Br mass of 134 ± 19 ng, which is 34% biased high. If we include in the regression both pixels 59 and 84 (600.321 and 600.426 nm, respectively, red-labelled peaks in **Figure 1B**) that show more sensitivity (lines for which $Ca^{79}Br$ and $Ca^{81}Br$ signals overlap), the

MEC slope approximates better to the true value as 0.5364 ± 0.0220 (116 ± 10 ng Br) is obtained, further supporting the concept that the MEC approach benefits from a higher sensitivity variation between lines (see **Figure 8B**).

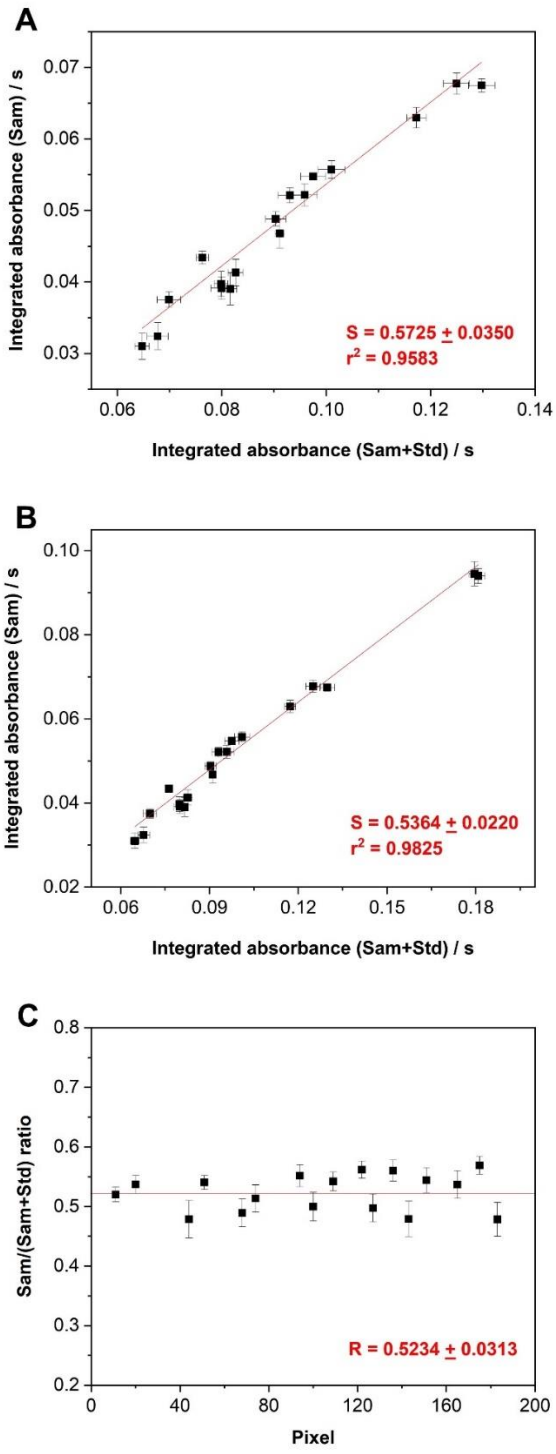

Figure 8. Experimental data for 100 ng Br as sample and 100 ng Br as spike using HR CS GFMAS *via* monitoring of the CaBr molecule in the vicinity of 600 nm using: (A) MEC with 17 transitions; (B) MEC with 19 transitions (the 17 used before plus pixels 59 and 84); and (C) MER with 17 transitions. Error bars correspond to the standard deviation (n=3).

When the MER approach is followed (see **Figure 8C**), the small difference between line sensitivities does not appear to show any clear influence for this strategy, as could be expected. Using more ratios provides a more robust estimation. The ratio estimated, 0.5234 ± 0.0313, is converted to 110 ± 14 ng Br, with a bias of 10%, which is in any case within the precision of the measurements. In conclusion, it is possible to assume that MEC could be usually recommended as a calibration strategy, unless the available transitions show similar sensitivities, a situation where MER should be considered instead.

I.3.5. Non-spectral interference

As discussed before, both strategies show higher limits of detection compared to external standard calibration, but they can help in detecting the occurrence of spectral overlaps at distinct transitions, which should result in outliers. Moreover, MEC and MER show potential to correct for matrix effects with only two solutions, in a similar way as what occurs with isotopic dilution,[43,44] or with standard addition (even though for the latter more points are usually prepared and measured to minimize the uncertainty of the final results when extrapolating).

A common problem in the case of HR CS MAS is the occurrence of interferences due to chemical competition with other species present in the matrix, affecting the formation of the target species. In the case of monitoring the diatomic molecule CaBr, there are two possibilities: the presence of species that interact with Br, not leaving it available to Ca (*e.g.,* Al) or the presence of species that react with Ca (*e.g.,* other halogens), which would eventually lead to the same effect: formation of less CaBr.[43]

One of the elements more commonly present in a sample at sufficiently high levels to compromise the formation of the CaBr diatomic molecule is Cl. Nakadi

et al.[43] already studied the interference of chlorine on the determination of Br *via* the monitoring of the CaBr molecule by HR CS GFMAS. In that work, the presence of Cl resulted in 80% of sensitivity loss for the signal of CaBr when it was found at an amount (in moles) 10 times higher than Br. The problem was circumvented using isotopic dilution as calibration strategy, a powerful approach, but one that requires looking for alternative, less sensitive transitions that show sufficiently high isotopic shifts, besides the use of an isotopic spike.

Under these circumstances, use of MEC and MER could be a more general way to compensate for this effect, because the change in the analytical signal caused by the presence of Cl should be proportionally the same in the sample and in the sample plus the spike, and thus the slope/ratio should be constant.

To evaluate this hypothesis, a 30 ng standard solution of Br was used as sample and CaBr was monitored around 625 nm. Four Br spikes were studied (10, 20, 30 and 40 ng Br) with three different Cl spikes: 0, 500 and 1000 ng of Cl as sodium chloride. Both MEC and MER were compared for each set of data, and the results are shown in **Figure 9**. Four pixels were used for this study (both MEC and MER), namely 114, 131, 149 and 168, due to their figures of merit, as the rest of the pixels did not provide a LOQ $\leq$ 30 ng (see **Table 3**).

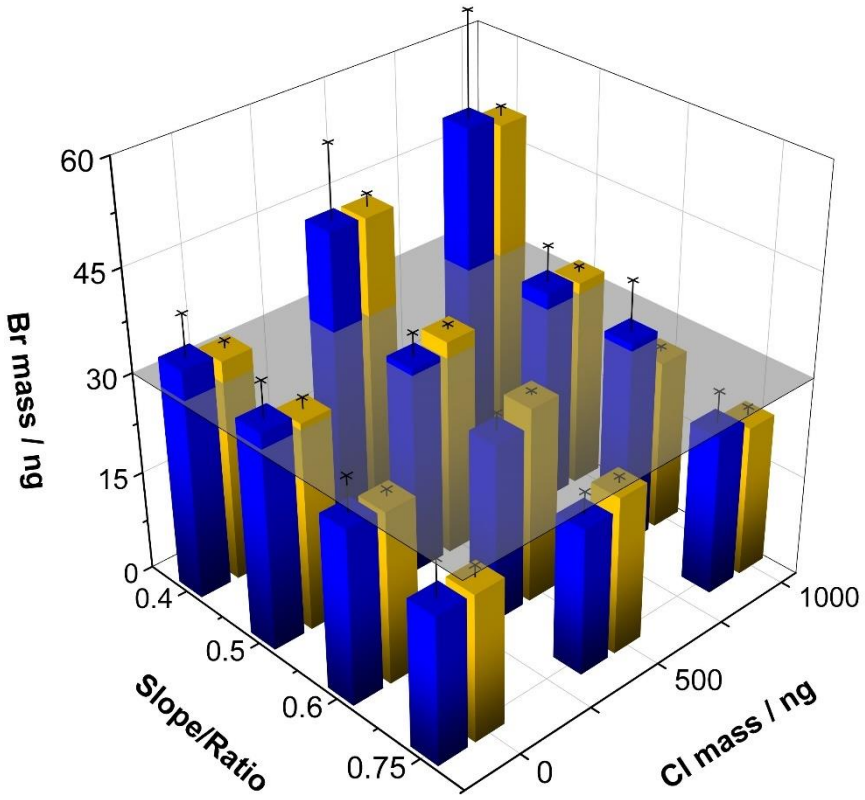

Figure 9. Study of the effect of the presence of Cl on the determination of Br *via* the monitoring of the CaBr molecule with HR CS GFMAS using MEC (blue bars) and MER (yellow bars) strategies for quantification. The gray surface indicates the real Br mass (30 ng). Error bars correspond to the standard deviation (n=5).

Evaluating pixel 168 (λ = 625.308 nm), there was a 35% decrease in the CaBr analytical signal when 500 ng Cl were added, and 54% for 1000 ng Cl. Nonetheless, using MEC (blue bars) and MER (yellow bars) it is possible to circumvent this interference, as can be seen in **Figure 9**. It is noteworthy that, as described previously, working at a slope/ratio around 0.5 usually leads to better accuracy (difference with the true value lower than 8% considering all Cl masses) Opting for a lower slope/ratio (0.4), results biased high seem to be obtained, while for a slope/ratio of 0.75 the results are a bit biased low. In this case, using four

transitions only produces increased RSD values for MEC in comparison with MER, as could be appreciated in the error bars of **Figure 9**.

Overall, both strategies were successful in correcting for the Cl interference in this study. Nevertheless, it seems advisable to carry out a previous study to have an approximate idea of the sample content before spiking it, or either to test various spikes to finally work with that providing a slope/ratio close to 0.5 - 0.6.

I.3.6. Determination of Br in water sample using MEC and MER

A CRM water (QC3060) was used to evaluate how both strategies can correct for the occurrence of interferences and validate the method in a complex matrix. This CRM provides the concentration of bromide (2.81 ± 0.42 mg L^{-1}) in addition of several anions, such as the halogens chloride (54.9 ± 8.2 mg L^{-1}) and fluoride (2.52 ± 0.38 mg L^{-1}), and others with higher concentrations as nitrate (66.1 ± 9.9 mg L^{-1}) and sulfate (81.5 ± 12.2 mg L^{-1}). Five transitions were evaluated (pixels 100, 114, 131, 149 and 168) around 625 nm, pipetting 20 μL of the sample (56.2 ± 8.4 ng Br) instead of 10 μL to increase the signal, with three Br spikes of 20.4, 58.3 and 96.6 ng. The results obtained are listed in **Table 5**.

Table 5. Determination of Br in QC3060 *via* the monitoring of CaBr with HR CS GFMAS using MEC and MER strategies. Uncertainties are given as 95% confidence intervals (n=5). n.a.: not applied. MEC values are obtained as recommended in this work (see 3.1.1.), while for MEC_Y, conventional linear regression considering only the errors in y-axis was used.

	Slope/Ratio			**Br concentration / mg L^{-1}**				
	MEC	**MEC_Y**	**MER**	**MEC**	**MEC_Y**	**MER**	**EC**	**Reference**
0	n.a.	n.a.	n.a.	n.a.	n.a.	n.a.	0.282 ± 0.022	
20.4	0.745 ± 0.116	0.743 ± 0.054	0.716 ± 0.023	2.97 ± 2.10	2.94 ± 0.86	2.57 ± 0.36	n.a.	2.81 ± 0.42
58.3	0.504 ± 0.045	0.504 ± 0.039	0.495 ± 0.020	2.97 ± 0.54	2.96 ± 0.47	2.85 ± 0.29	n.a.	
96.6	0.390 ± 0.036	0.392 ± 0.033	0.376 ± 0.017	3.08 ± 0.47	3.11 ± 0.43	2.91 ± 0.27	n.a.	

Using external standard calibration (calibration range 20 – 100 Br ng, 5 points, r^2 = 0.9993, λ = 625.315 nm), the Br concentration was calculated to be 0.282 ± 0.022 mg L^{-1}, which represents only around 10% of recovery, further highlighting the influence of the concomitant species. As predicted, using a slope/ratio close to 0.5 leads to better values with both MEC and MER, with RSDs of 15% and 8%, and a deviation of the average value of only 5.6% and 1.5%, respectively, well within the uncertainty of the measurements.

In any case, all the conditions evaluated lead to results that overlap with the expected value. However, for a 0.75 slope/ratio value, the uncertainty remains higher than the others (in particular for MEC), demonstrating that high slopes should be avoided. Despite this high uncertainty at 0.75, use of MEC provides practically the same average value for all the spikes, proving its robustness.

MEC was also evaluated with conventional least-squares regression (MEC_Y) for further comparison. Both MEC strategies lead to similar average results, although the uncertainty is larger when using York method (see 3.1.1.), as expected, because the error sources from both axes are considered in such case. Such difference becomes more relevant when using high S values (S ≅ 0.75).

Overall, all strategies, when properly optimized, enable circumventing these non-spectral interferences caused by competing species, supporting their use as a valuable alternative method of calibration when performing HR CS GFMAS.

- **I.4. Conclusions**

The limitations and application of the MEC calibration strategy for determining non-metals *via* HR CS GFMAS was verified in this study, using CaBr as a proxy. Moreover, another similar approach that only differs in the way in which the data is processed (MER) was proposed and evaluated as well for the first time, comparing its performance with that of MEC in different circumstances.

This work confirms previous reports indicating that MEC is a useful tool as a calibration alternative due to its advantage of needing only the preparation and measurement of two aliquots (sample, and sample plus spike) to determine the analyte concentration. Furthermore, this study presents some new conclusions for the best use of both MEC and MER: i) use of too high or too low slope/ratios is not recommended, and values between 0.5 and 0.6 should be chosen; ii) MEC could provide better precision, but its use is favored when many transitions of dissimilar sensitivity are available; if, on the other hand, the transitions available are only a few or show similar sensitivities, the use of MER can provide better results. Furthermore, the calculation of LODs and LOQs using MER is proposed, as it enables checking which lines are above these limits for any particular determination. In any case, it should always be remembered that both the analyte contents of the sample and of the sample plus standard should fall within the working linear range for all the lines considered.

The measurements were hampered mainly by the wavy baseline and occasional appearance of an unknown molecule, as well as by the occurrence of chemical interferences that prevented the quantitative formation of CaBr. Nevertheless, accurate results could be obtained for both MEC and MER, under optimal conditions, proving that these can be very valuable analytical tools for HR CS

GFMAS. Moreover, this conclusion can be expanded to other techniques that are prone to be affected by similar issues, and where several different analytical signals can be derived from a single analyte.

- **I.5. References**

1. B. V. L'Vov, ***J. Anal. At. Spectrom.***, 1988, **3**, 9–12.
2. A. Hulanicki, ***Anal. Proc.***, 1992, **29**, 512–516.
3. G. L. Donati and R. S. Amais, ***J. Anal. At. Spectrom.***, 2019, **34**, 2353-2369.
4. J. A. Carter, A. I. Barros, J. A. Nóbrega and G. L. Donati, ***Front. Chem.***, 2018, **6**, 504.
5. P. Kościelniak and J. Kozak, *Crit. Rev.* ***Anal. Chem.***, 2006, **36**, 27–40.
6. J. E. T. Andersen, ***TrAC - Trends Anal. Chem.***, 2017, **89**, 21–33.
7. F. Vanhaecke, L. Balcaen and D. Malinovsky, ***J. Anal. At. Spectrom.***, 2009, **24**, 863–886.
8. P. Rodríguez-González, J. M. Marchante-Gayón, J. I. García Alonso and A. Sanz-Medel, ***Spectrochim. Acta, Part B,*** 2005, **60**, 151–207.
9. K. G. Heumann, S. M. Gallus, G. Rädlinger and J. Vogl, ***J. Anal. At. Spectrom.***, 1998, **13**, 1001–1008.
10. A. Virgilio, D. A. Gonçalves, T. McSweeney, J. A. Gomes Neto, J. A. Nóbrega and G. L. Donati, ***Anal. Chim. Acta***, 2017, **982**, 31-36.
11. R. C. Machado, A. B. S. Silva, G. L. Donati and A. R. A. Nogueira, ***J. Anal. At. Spectrom.***, 2018, **33**, 1168–1172.
12. D. V. Babos, A. Virgilio, V. C. Costa, G. L. Donati and E. R. Pereira-Filho, ***J. Anal. At. Spectrom.***, 2018, **33**, 1753–1762.
13. A. S. Augusto, J. P. Castro, M. A. Sperança and E. R. Pereira-Filho, ***J. Braz. Chem. Soc.***, 2019, **30**, 804–812.
14. D. F. Andrade, F. M. Fortunato and E. R. Pereira-Filho, ***Anal. Chim. Acta***, 2019, **1061**, 42–49.
15. F. M. Fortunato, T. A. Catelani, M. S. Pomares-Alfonso and E. R. Pereira-Filho, ***Anal. Sci.***, 2019, **35**, 165–168.
16. A. A. C. Carvalho, L. A. Cozer, M. S. Luz, L. C. Nunes, F. R. P. Rocha and C. S. Nomura, ***J. Anal. At. Spectrom.***, 2019, **34**, 1701–1707.
17. A. L. Vieira, D. A. Gonçalves, A. Virgilio, E. C. Ferreira, B. T. Jones, G. L. Donati and J. A. Gomes Neto, ***J. Anal. At. Spectrom.***, 2019, **34**, 972–978.
18. M. C. Alencar, D. A. Gonçalves, G. Nicolodelli, S. L. Oliveira, G. L. Donati and A. R. L. Caires, ***Spectrochim. Acta, Part A***, 2019, 117221.
19. A. Virgilio, J. A. Nóbrega and G. L. Donati, ***Anal. Bioanal. Chem.***, 2018, **410**, 1157–1162.
20. J. M. de Higuera, A. B. S. da Silva, A. F. de Oliveira and A. R. de Araujo Nogueira, ***Food Chem.***, 2020, **303**, 125395.
21. E. Bolea-Fernandez, L. Balcaen, M. Resano and F. Vanhaecke, ***J. Anal. At. Spectrom.***, 2017, **32**, 1660–1679.
22. L. Balcaen, E. Bolea-Fernandez, M. Resano and F. Vanhaecke, ***Anal. Chim. Acta***, 2015, **894**, 7–19.
23. C. B. Williams and G. L. Donati, ***J. Anal. At. Spectrom.***, 2018, **33**, 762-767.

24. A. Virgílio, A. B. S. Silva, A. R. A. Nogueira, J. A. Nobrega and G. L. Donati, ***J. Anal. At. Spectrom.***, 2020, **35**, 1614-1620.
25. B. Welz, H. Becker-Ross, S. Florek and U. Heitmann, *High-resolution Continuum Source AAS. The Better Way to Do Atomic Absorption Spectrometry*, Wiley-VCH, Weinheim, 2005.
26. M. Resano, M. Aramendía and M. A. Belarra, ***J. Anal. At. Spectrom.***, 2014, **29**, 2229–2250.
27. M. Resano, E. García-Ruiz, M. Aramendía and M. A. Belarra, ***J. Anal. At. Spectrom.***, 2019, **34**, 59–80.
28. M. Resano, M. Aramendía, F. V. Nakadi, E. García-Ruiz, C. Alvarez-Llamas, N. Bordel, J. Pisonero, E. Bolea-Fernández, T. Liu and F. Vanhaecke, ***TrAC Trends Anal. Chem.***, 2020, **129**, 115955.
29. M. Resano, L. Rello, M. Flórez and M. A. Belarra, ***Spectrochim. Acta, Part B,*** 2011, **66**, 321–328.
30. M. Resano, M. R. Flórez and E. García-Ruiz, ***Spectrochim. Acta, Part B,*** 2013, **88**, 85–97.
31. B. Welz, F. G. Lepri, R. G. O. Araujo, S. L. C. Ferreira, M. D. Huang, M. Okruss and H. Becker-Ross, ***Anal. Chim. Acta***, 2009, **647**, 137–148.
32. M. Resano, M. R. Flórez and E. García-Ruiz, ***Anal. Bioanal. Chem.***, 2014, **406**, 2239–2259.
33. M. R. Flórez and M. Resano, ***Spectrochim. Acta, Part B,*** 2013, **88**, 32–39.
34. https://www.originlab.com/doc/Origin-Help/LinearFit-XErr-Dialog, accessed in 2020, July 14th
35. B. Welz, L. M. G. dos Santos, R. G. O. Araujo, S. do C. Jacob, M. G. R. Vale, M. Okruss and H. Becker-Ross, ***Spectrochim. Acta, Part B,*** 2010, **65**, 258–262.
36. M. D. Huang, H. Becker-Ross, S. Florek, U. Heitmann and M. Okruss, ***Spectrochim. Acta, Part B,*** 2008, **63**, 566–570.
37. É. R. Pereira, I. N. B. Castilho, B. Welz, J. S. Gois, D. L. G. Borges, E. Carasek and J. B. De Andrade, ***Spectrochim. Acta, Part B,*** 2014, **96**, 33–39.
38. T. Limburg and J. W. Einax, ***Microchem. J.***, 2013, **107**, 31–36.
39. R. W. B. Pearse and A. G. Gaydon, *The Identification of Molecular Spectra, fourth ed*., Chapman and Hall Ltd., London, 1976.
40. N. Ozbek and A. Baysal, ***TrAC - Trends Anal. Chem.***, 2017, **88**, 62–76.
41. L. C. Pomarolli, M. A. M. Silva da Veiga, M. Resano, F. V. Nakadi, ***J. Anal. At. Spectrom.***, 2020, **35**, 2305.
42. D. J. Butcher, ***Anal. Chim. Acta***, 2013, **804**, 1–15.
43. F. V Nakadi, M. A. M. S. da Veiga, M. Aramendía, E. García-Ruiz and M. Resano, ***J Anal Spectrom***, 2016, **31**, 1381–1390.
44. F. V. Nakadi, M. A. M. S. da Veiga, M. Aramendía, E. García-Ruiz and M. Resano, ***J Anal Spectrom***, 2015, **30**, 1531–1540.

Chapter II

Simultaneous Determination of Halogens in Active Pharmaceutical Compounds *via* Continuum Source Graphite Furnace Molecular Absorption Spectrometry coupled with a Modular Simultaneous *Echelle* Spectrograph (CS GF MAS-MOSES)

- **II.1. Introduction**

The determination of halogens in organic derivatives is still challenging.[1] Inductively coupled plasma mass spectrometry (ICP-MS) suffers from the difficulty to ionize these elements (specially fluorine) as well as from spectral overlap (Br, Cl), while to deploy emission spectrometry the use of particular instrumentation capable of monitoring the vacuum UV is required. Even though with the help of a sector field mass filter it is possible to perform the analysis,[2] there is still necessity for alternative techniques to overcome problems such as solvent and/or matrix incompatibilities.

The reference technique for the determination of halogens in active pharmaceutic ingredients (APIs) is ionic chromatography (IC) due to its selectivity and capability to couple in hyphenated systems.[3–6] However, that technique is time consuming, especially compared to atomic techniques such as absorption, emission, and mass spectrometry. Ion selective electrode (ISE) is a better option due to its simplicity and speed. However, it only detects free ions, so a pretreatment is necessary for total F determination, and its sensitivity is sometimes not sufficient. High resolution continuum source atomic absorption spectrometry has shown its potential to determine non-metals *via* the monitorization of the absorbance of molecular species.[7,8] The key of this improvement compared to traditional line source instruments is the high intensity continuum short arc xenon lamp, capable of emitting between 190-900 nm, and the monochromator system consisting of a quartz prism and an *echelle* grating, responsible of the high resolution and a spectral window of less than 1 nm for the visible, and even narrower in the UV region.[9] Sadly, the spectral range of the instrument is limited, and just a few examples of simultaneous determinations have been reported successfully, with

only a couple of elements falling in the right spectral window, and/or the necessity of using a very low sensitive line for one of the elements.[10] Thus, a unique technique capable of trace level determination in liquids and/or direct solids and relatively free from spectral interferences cannot compete with their direct competitors in the majority of applications (ICP-MS, ICP-OES) where multi-element information is required.[11]

Determining halogens by HR CS GF MAS is already described in the literature. Several molecules have been studied for this purpose. Fluorine has been determined by using calcium,[12–19] gallium,[20,21] aluminum,[22] strontium,[23–25] and boron[22] as molecular forming agents; chlorine, by using aluminum,[26,27] strontium,[28–30] magnesium,[31,32] gallium,[33] calcium[3,34] and indium.[27,35] Bromine has been determined with calcium[36,37] and thallium.[38] From the different molecules, the three halogens can form a bond with calcium, with a dissociation energy of 527, 406 and 348 kJ mol^{-1} for CaF, CaCl and CaBr respectively, which might be stable enough during vaporization in for graphite furnace molecular absorption spectrometry monitoring. Thus, the three analytes act as interference to each other for many molecule forming agents. Moreover, chlorine is present in many samples, such as marine waters, biological tissues, foodstuff, etc. at fairly high levels, which may result in interferences due to chemical competition for the Ca atoms. This can be solved by trying to find more specific molecule forming agents, or else tby applying a standard addition strategy to compensate for such interference.

A new monochromator system has been developed to improve the features of contrAA instruments. MOSES opens new opportunities for absorption spectrometry (AS) due to the spectral window, covering in just one measurement

around 100-200 nm, depending on the region of the spectra. Simultaneous determinations of metals and molecules, multivariate analysis and machine learning become accessible for the technique. MOSES first setup is described elsewhere,[39] and its scheme is shown in **Figure 1**.

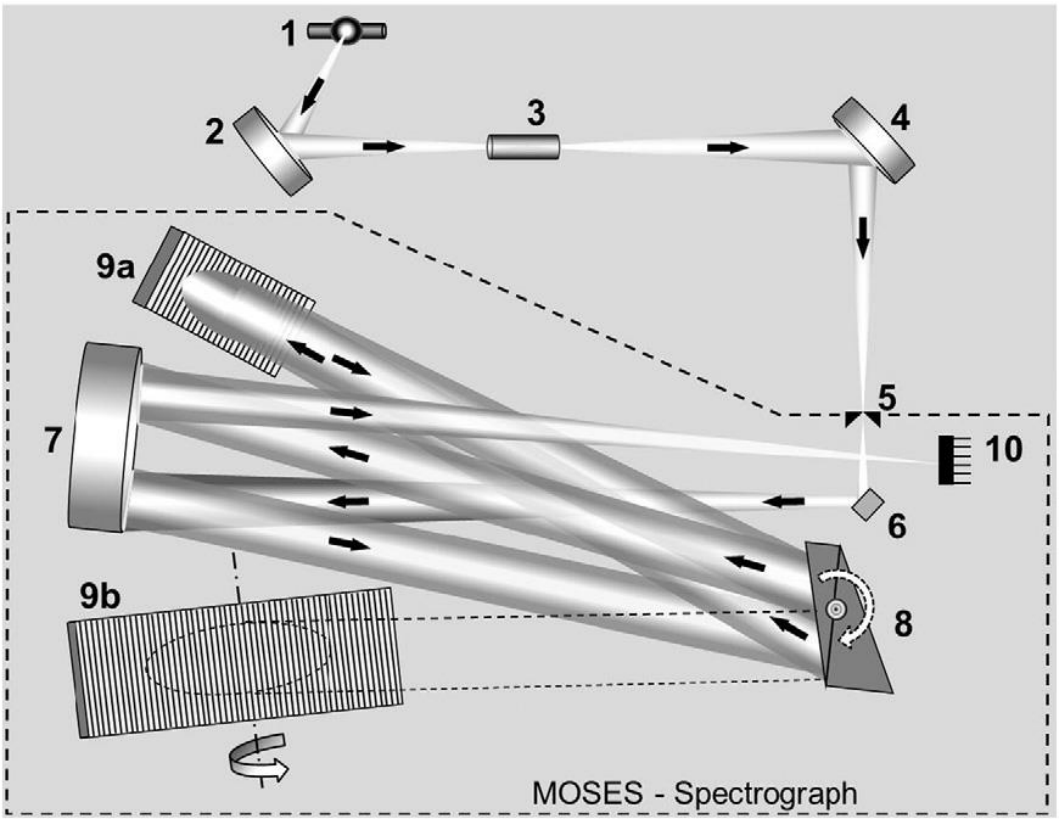

Figure 1: Schematic diagram of the experimental set-up including MOSES spectrograph: (1) laser-driven continuum source, (2, 4) transfer optics consisting of two elliptical mirrors, (3) atomizer, (5) entrance slit, (6) folding mirror, (7) off-axis parabolic mirror, (8) prism stage with two Littrow prisms, (9a, 9b) echelle gratings, and (10) C-MOS detector. Reproduced with permission from Elsevier.[39]

With the increase of spectral information, strategies based on multivariate analysis and machine learning become available. The development of new methods, including algorithms, with the capacity to make predictions can bypass

problems of spectral and proportional interferences or find patterns in overwhelmed amounts of data.

However, this is not a completely new methodology in the spectrometry research field. Machine learning (ML) is being applied recurrently in Raman spectroscopy, laser ablation-ICP-MS and laser-induced breakdown spectrometry (LIBS). The three of them can register a wide region of the spectra, making ML a desirable strategy. Recently, an article using XGboost (a ML algorithm) to measure the isotopic ratio of lithium *via* HR CS GFAAS has been published. This algorithm was applied to a limited region of the spectra (from 670.6658 nm to 670.9340nm, 61 detector pixels) measured with a contrAA 800.[40] Thus, the wider spectral window of MOSES possesses the potential for developing new applications in absorption spectrometry. XGboots is a univariate algorithm based on a scalable tree boosting system, providing successful ML strategies for state-of-the-art results.[42] The advantage of this method over PCA or other multivariate analysis is that it is suitable for nonlinear combinations, using every spectrum as a fingerprint.

The algorithm starts with a prediction (non-defined) and then, a loss function is calculated to assess the validation of that initial prediction. The objective of the algorithm is to minimize the loss function.[42]

$$\mathrm{L}\,(\varphi) = \sum_i l(\hat{y}i, yi) + \sum_k \Omega\,(f_k) \qquad (1)$$

Where $\Omega\,(f) = \gamma \mathrm{T} + \frac{1}{2}\,\lambda w^2$

Equation (1) consists of two terms, the first one minimizes the pseudo residuals of the predicted value (ŷi) and the true value (yi), the second term Ω penalizes the complexity of the model and smooths the weights to avoid over-fitting.

In this study, a ML strategy using a XGboost algorithm is applied to build a model capable of estimate the proportion of halogens in APIs with variable proportions of Br, Cl and F. This approach, combined with the determination of F *via* multi-energy ratios (MER), an approach already developed and evaluated in this thesis (see chapter ZZ), can provide quantitative information for the three target elements, despite the expected chemical interferences.

The authors believe that such example serves a proof-of-concept on how new calibration approaches, combined with new instrumental advances, can help in the development of new analytical methods to perform challenging multi-element determinations.

- **II.2. Experimental**

II.2.1. Samples and standards

Standard solutions of F, Cl and Br were prepared from the sodium salt dissolved in mili-Q water (18.2 MΩ cm*,* Millipore gradient, Merck Millipore, Darmstadt, Germany). A Ca solution of 3% m/m was prepared from a solid standard of $CaCO_3$ (Certipur®, Merck, Germany) dissolved in HNO_3 concentrated (EMSURE, Merck, Darmstadt, Germany), which was previously purified by sub-boiling distillation in PFA containers. A zirconium dioxide nanopowder (ZrNPs) in a water suspension of 20 wt% and 45-55 nm in size (US Research Nanomaterials, Inc, USA) was used as permanent modifier for F for the entire set of analyses. Additionally, a Pd solution (10 g L^{-1}, $Pd(NO_3)_2$/ HNO_3 ca. 15%, Merck, Darmstadt, Germany) was used as chemical modifier for Cl and Br.

Four active pharmaceutical ingredients (APIs) containing different amounts of halogens were analyzed for validation of the ML model. Penfluridol ($C_{28}H_{27}ClF_5NO$, purity = 100.1 ± 0.3%), efavirenz ($C_{14}H_9ClF_3NO_2$, purity = 100.1

± 0.4%) and gefitinib ($C_{22}H_{24}ClFN_4O_3$, purity= 98.9 ± 0.4%) were purchased from LCGC (London, UK) and selumetinib ($C_{17}H_{15}BrClFN_4O_3$, purity = 98+%) was purchased from AmBeed (Chicago Area, IL, USA). The analysis solutions were prepared by diluting the APIs in dimethylsulfoxide (Merck, Darmstadt, Germany) and acetonitrile (Sharlab SL, Barcelona, Spain).

II.2.2. Instrument and conditions

All multi-energy ratio measurements for F determination were carried out using a HR-CS AAS contrAA800G (Analytik Jena, Jena, Germany) as radiation source and atomization system.

Experiments for the XGBoost algorithm training and API proportion determination were carried out using a combination of a commercially available graphite furnace HR-CS AAS contrAA800 with the direct solid autosampler solidAA and a unique MOSES spectrograph[39] (Leibniz-ISAS e.V.) equipped with the original contrAA xenon lamp and a high resolution large format CMOS sensor. Half of the radiation was directed to the contrAA monochromator and detector system while the other half was directed towards the MOSES, thus, only half of the initial intensity reaches both detectors, decreasing the signal-to-noise ratio. This instrument was available at the BAM (Federal Institute for Materials Research and Testing) in Berlin.

The optimization of the temperature program for sample analysis and determination of F using the MER was carried out at the university of Zaragoza.

Solid graphite platform was modified permanently with ZrNPs using the method described by Abad *et al*.[41] For measurement of standards and samples, 10 µL of calcium solution 3% and 10 µL of a Pd solution were deposited onto the modified

platform alongside 10 µL of the solution of interest. The temperature program is displayed in **table 1.**

Table 1: HR CS GFMAS temperature program

Temperature Program				
Step	Temperature/ºC	Ramp/ºC s^{-1}	Hold/s	Ar gas flow/L min^{-1}
Drying	80	6	20	2
Drying	90	3	20	2
Drying	110	5	10	2
Pyrolysis	800*	300	10	2
Gas adaption	800	0	5	0
Atomize	2300	3000	9	0
Clean	2500	500	4	2

*1600 ºC s^{-1} for API analysis

II.2.3. ML data analysis for halogen proportion in samples

The ML procedure followed in this study is summarized in **Figure 1**. To develop the model, 150 solutions containing different concentrations of Br, Cl and F were prepared with the proportions in the ternary diagram (see **Figure 2**) and measured with MOSES (3 replicas per mixture). Thus, all the spectra extracted between 520 and 630 were used to build the model. Besides, the amount of data generated per measure was difficult to process, so it was decided to integrate contiguous points 2 by 2, reducing the temporal resolution from 0.073 s (the standard resolution from a contrAA instrument) to 0.146 s, for a total of 11000 points per spectra. Time-resolved three-dimensional spectral data was acquired using *Echelle software* developed to process MOSES data. Then the data is

preprocessed to include it in the XGboost model integrated in MATLAB based software SOLO+MIA (Eigenvector Research, Inc, Manson, USA).

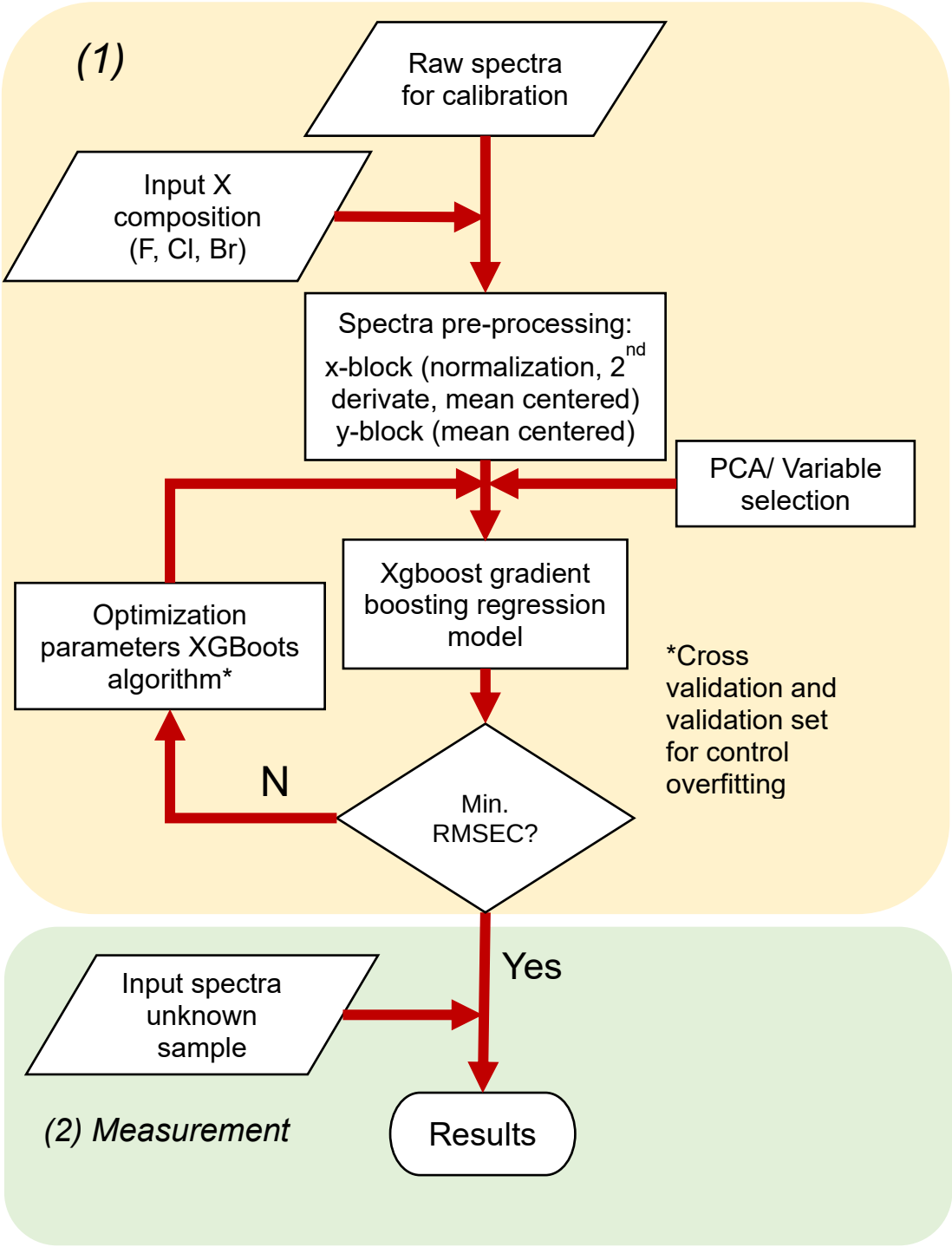

Figure 1: Flow diagram for the data analysis of the halogen fractions using machine learning.

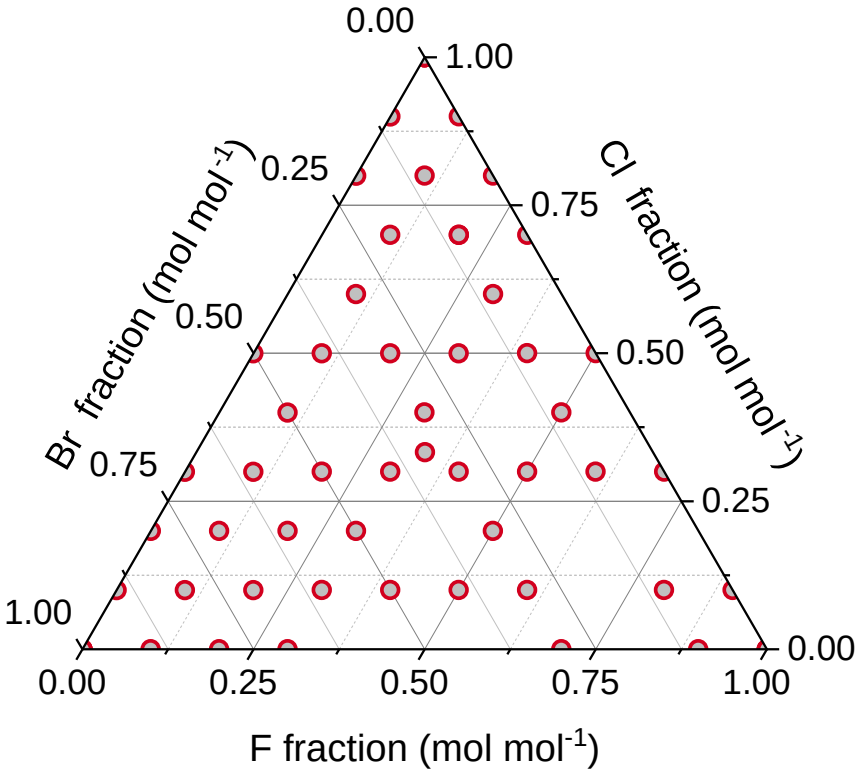

Figure 2: Ternary diagram with the halogen fractions for the ML training model.

The preprocessing of the spectra consisted in normalizing the spectra and calculating its 2nd derivative. Then, the variables chose for the tree gradient model were selected using partial component analysis (PCA).

II.2.4. Determination of F content in APIs using Multi Energy Ratios

Fluorine determination in presence of other halogens cannot be carried out by standard calibration in MAS with calcium as molecule forming agent, and a strategy capable of solving proportional interferences is needed. Standard addition is the most reliable option; however, a new strategy has been proposed recently. This methodology can correct for these interferences in the same way standard addition does, but it only needs one addition monitored at different "channels" (wavelengths in the case of multi-energy calibration methods). In this

work, we make use of a derivation of multi-energy calibration named multi-energy ratios, which is discussed in detail in Chapter ZZ of this thesis. With this approach, only 3 solutions per sample were analyzed: blank, sample and sample+ spike. Samples were diluted until the concentration of F was approximately 500 µg L^{-1} and spiked with a F standard of the same concentration to obtain a multi energy ratio as near as possible to 0.5, which is optimal as described by Garde *et al.*[43] Penfluridol and efavirenz were diluted in acetonitrile in a first step, then, the last dilution was made in milli-Q water until the target concentration was reached. Gefitinib and selumetinib followed the same process but these two compounds were soluble in dimethylsulfoxide (DMSO) instead of acetonitrile during the first dilution. Reference values of concentrations of the halogens in these compounds were calculated attending to their molecular formula and purity for comparison purposes.

- **II.3. Results and Discussion**

II.3.1. Temperature program and conditions for CaX

The three molecules selected to monitor the halogens, CaX, have already been studied in the literature. The furnace temperature programs for them are similar, which permits developing a compromise program to maximize the signal-to-noise ratio for the three target elements. In this work, conditions were adapted from C. Abad *et al*,[41] A. Guarda[34] and R. Garde *et al*[43] to reach compromise conditions for the three analytes

From the three target molecules, the absorbance of CaF increases significantly in the presence of a Zr permanent modifier. Thus, the absorbances of blanks and a standard of Cl and Br were assessed in presence and absence of the modifier, showing no significant differences. However, after measuring a solution with F,

the blanks measured afterwards presented higher absorption values than before. This might occur because F is being retained by the ZrNPs deposited on the surface of the tube, but after several cleaning cycles F is released completely. However, this coating only affects the CaF signal and the blanks of CaCl and CaBr are not affected.

II.3.2. Selection of the spectra region

CaF, CaCl and CaBr present their major electronic transitions in the visible region. The transitions centered at 606, 620 and 625 have been used for determination purposes. However, these are not the only transitions present in the spectra. Thanks to the MOSES features, it is possible to record more than 200 nm simultaneously. **Figure 3** shows the spectra of the three molecules formed.

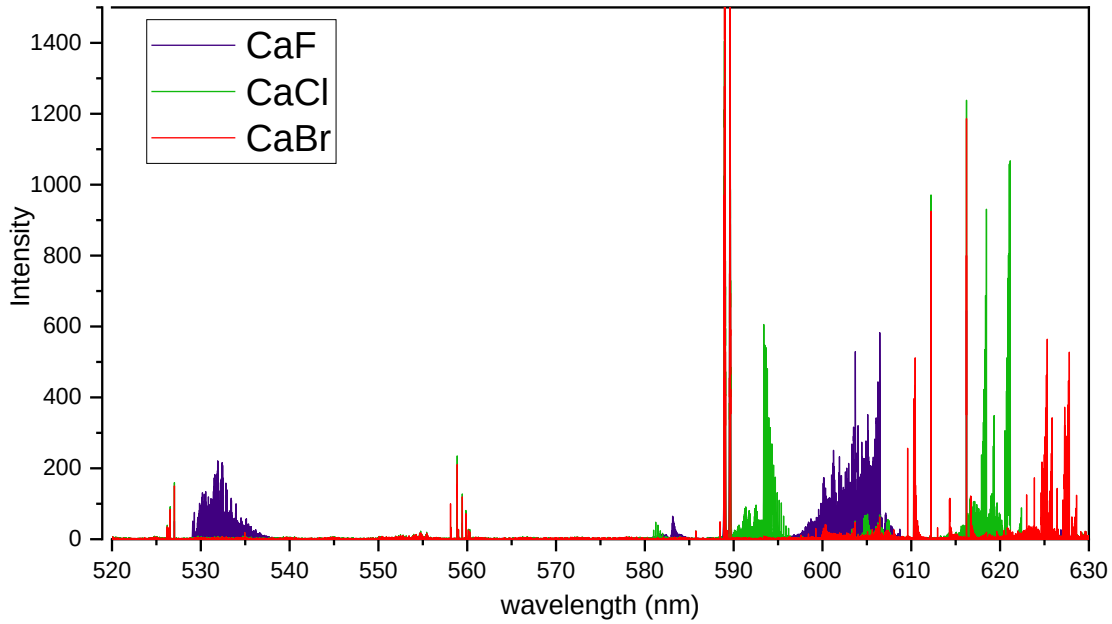

Figure 3: Integrated bbsorption spectra from 520nm to 630 nm of a) CaF; b) CaCl; c) CaBr.

CaF presents three electronic transitions in this region of the spectra. A broad one covering from 529 nm to 537 nm approximately, the second covers from 581.5 to 584 nm, and the principal transition from 600 to 608 nm. Four transitions corresponding to CaCl are observed: from 550 to 556 nm; from 590 to 596 nm; from 617.7 to 619.5 nm, and the last one from 620.5 to 621.2. CaBr only shows transitions at 610.5 nm and at 625 nm.

Thus, the input spectra (x-block in the ML model) were set between 520 and 630 nm.

II:3.3. Optimization and validation of the ML model

The ML model was validated by cross-validation (Venetian blinds with 10 splits and blind thickness of 1) and the best model was estimated with Root Mean Square of Calibration (RMSEC) (see **Table 2**)

Table 2: Optimization and validation parameters of the XGboost model for the data treatment.[a]

Parameter	Value
Preprocessing spectra	(1) Surface normalization, (2) 2nd derivative Savitzky-Golay (order 2, window 15points, tails weighted), and (3) mean center
Preprocessing Halogen composition (Y-block)	mean center
Feature compression of the spectra	PCA
Eta (learning rate)	0.3
Maximum depth	1

Number of rounds	100
Cross-validation	Venetian blinds with ten splits and blind thickness = 1
RMSEC	0.00194
Bias	7.20×10^{-6}

[a]Parameters for preprocessing, feature compression, learning parameters, and cross-correlation are given. Eta describes the slope of the gradient for iterative optimization, the depth is the number of hierarchy levels of the trees, the rounds resemble the number of iterations, and root-mean-square error of calibration (RMSEC) gives the RMS error of the calibration.

To assess the prediction capacities of the ML model, four active pharmaceutical ingredients (API) containing variable concentrations of Br, Cl and F were analyzed using HR CS GFMAS-MOSES to assess the error committed by the model after analyzing them. The proportions of halogens are variable in these compounds, showing F: Cl: Br proportions of 1:1:0 (gefitinib), 1:3:0 (efavirenz), 1:5:0 (penfluridol) and 1:1:1 (selumetinib). Solutions of these compounds were prepared following the description presented in section 2.4. Three replicas per API were measured using MOSES and the proportions of halogens quantified using the XGBoost model. Br model showed worst capabilities than the other two, probably, due to the analytical properties of this molecule compared to the other two studied (it is the one with the weakest molecular bond), and the model do not respond to the changes in Br concentration in the mixtures. Since the degrees of freedom are two, Br can be calculated as the remaining fraction, $\chi_{Br} = 1 - \chi_F - \chi_{Cl}$. The results of the proportions returned from the model are in good agreement

with the proportions of the halogens showed in the API formulae with a slight overestimation for F (see **Table 3**).

Table 3: Theoretical fractions of F, Cl and Br in the four APIs and its fractions calculated using the XGBoost ML model.

	Theoretical value fractions			Measured value fractions		
Compound	F	Cl	Br	F	Cl	Br
efavirenz	0.750	0.250	0.000	0.755 ± 0.006	0.243 ± 0.005	0.002 ± 0.006
penfluridol	0.833	0.167	0.000	0.849 ± 0.015	0.150 ± 0.010	0.001 ± 0.012
gefitinib	0.500	0.500	0.000	0.522 ± 0.005	0.483 ± 0.006	-0.005 ± 0.001
selumetinib	0.333	0.333	0.333	0.345 ± 0.010	0.332 ± 0.002	0.323 ± 0.012

II.3.4. F determination in active pharmaceutic ingredients using multi energy ratios

The interferences between halogens in APIs might be sufficiently low to be corrected with a standard addition procedure, or a MEC method. But it would require carrying three different additions for each sample. The determination of the proportions using MOSES, although it might appear as a more complicated approach, once the ML approach is fully developed, reduces the working time of the operator, and it is easy to apply. It also reduces the amount data generated by MOSES, which is a problem of practical significance.

From the three analytes, Br is not present in three of the four samples, therefore only Cl and F can be used for determination purposes. F was selected because of its higher sensitivity, lower limit of detection, and, as discussed before in section 3.3, its higher energy bond, which favors its formation over the others, diminishing chemical interferences.

As discussed before, ZrNP coating was necessary because F is prone to be lost before the vaporization of CaF and Zr coating strongly retains the F. This is advantageous for the sample and the spike, as both inorganic and organic F will be then vaporized similarly, favoring the determination.

The appearance of a molecule/noise signal prior to the CaF hampers proper signal integration (see **figure 4**). The absorption profile seems randomly distributed; however, the intensity of the peak never surpasses the value of the sample and shows a certain trend of proportion. This behavior is already described by Pomarolli *et al*.[44] To avoid the integration of this part, it was decided to increase the pyrolysis to 1600ºC. Adding an integration delay would work as well.

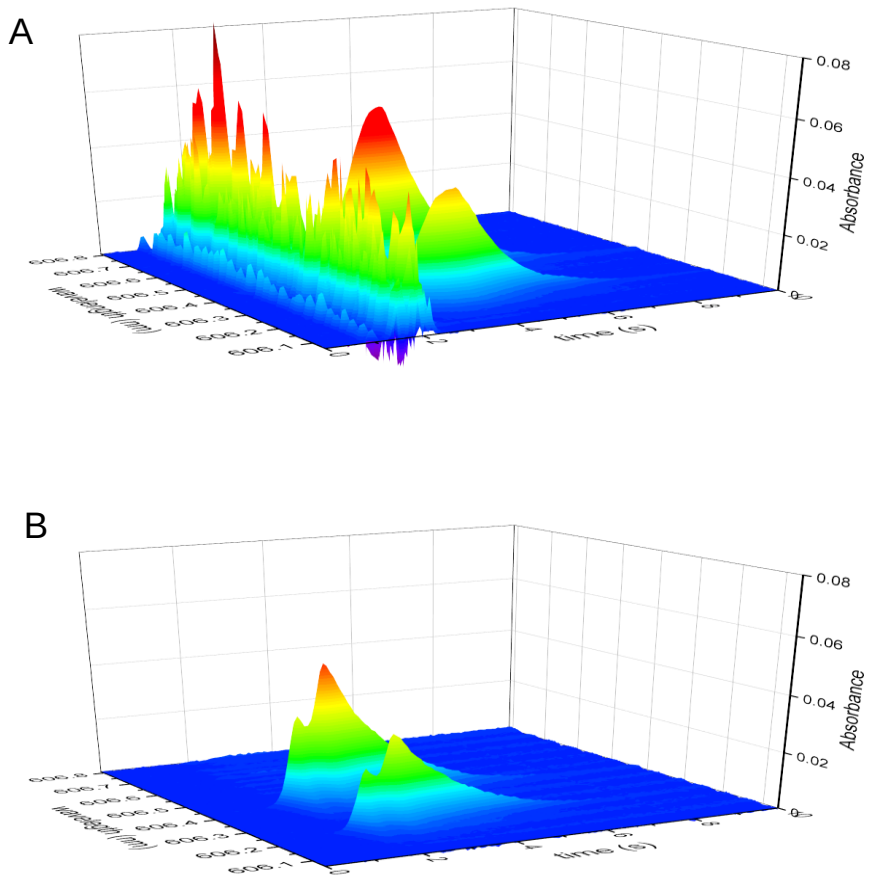

Figure 4: Three dimensional spectra of CaF obtained measuring gefitib dissolved in DMSO A) using 800ºC s^{-1} pyrolysis and B) using 1600ºC s^{-1} pyrolysis.

Blanks measured after a standard or sample were always higher, showing a memory effect. To return to original values, around ten temperature cycles were needed. Besides, calcium is corrosive for the platform, reducing the durability of the graphite tube. The combination of corrosion by calcium and F retention by the Zr coating produces an effect where after several cycles, a replica shows an abnormal rise of the absorbance. We hypothesize that part of the F is sometimes retained under the surface by the Zr, and, when graphite particles start to shatter, Zr-F adducts are released, increasing the CaF signal. To minimize these effects,

the analysis cycle was modified. Instead of measuring consecutive replicas, the analysis followed a cycle of blank, sample and sample+spike, until obtaining three replicas per measure. Using this strategy, the results obtained were in good agreement with the F present in samples (**Table 4**). 5% or less error is achieved for every determination.

Table 4. Results of the F determination using MER (n=3, number of transitions= 4)

Compound	F concentration (reference value) in APIs/ mg g^{-1}	F concentration found with MER HR CS GFMAS/ mg g^{-1}	% error
efavirenz	180.6	179.4 ± 1.5	-1%
penfluridol	181.3	185.2 ± 9.7	2%
gefitinib	42.0	42.1 ± 2.4	0%
selumetinib	40.7	42.7 ± 5.3	5%

Finally, the concentration of Cl and Br were determined using the proportions calculated with the XGBoost model and the concentration of F calculated using MER (see **table 5**). Such results are shown in Table 6. Uncertainties were calculated propagating the standard deviations of the MER determination and ML proportions.

Table 5: Cl and Br concentrations calculated in APIs using the proportions of halogens calculated with the ML model and the concentration of F using MER.

Compound	Cl conc. (ref. value) in APIs/ mg g^{-1}	Cl conc. found (Xgboost+ MER)/ mg g^{-1}	% error	Br conc. (ref. value) in APIs/ mg g^{-1}	Br conc. found (Xgboost+ MER)/ mg g^{-1}	% error
efavirenz	112.4	107.7	-4%	0	2.0	n.a.
penfluridol	67.8	61.1	-10%	0	0.4	n.a.
gefitinib	78.4	72.7	-7%	0	-1.7	n.a.
selumetinib	76.0	76.7	1%	174.6	171.1	-2%

As can be seen, overall, a good agreement with the references is possible, as deviations lower than 10% were always found for all the halogen quantifications.

- **II.4. Conclusions**

A novel machine learning strategy is described for absorbance spectrometry to determine the proportions of halogens in samples. Even though halogens act as interference among them, XGBoost could return the proportion of the halogens in the samples. F content was determined using a multi energy ratio method monitoring 4 vibronic transitions at 605.8602, 606.0377, 606.2302 and 606.4379 nm. Precision of the algorithm was around 0.1% and determination error was less than 5% for every sample. The model performs worst for Br, which was calculated as the remaining fraction after calculating F and Cl proportion.

In any case, the method proposed, once the ML method is fully developed and validated enables fast determination of Br, Cl and F in unknown samples, since only F needs to be determined *via* MER (measuring only sample and sample plus standard), and Br and F can subsequently be determined *via* the proportions obtained by ML.

- **II.5. References**

1 P. A. Mello, J. S. Barin, F. A. Duarte, C. A. Bizzi, L. O. Diehl, E. I. Muller and E. M. M. Flores, ***Anal. Bioanal. Chem***., 2013, **405**, 7615–7642.
2 X. Bu, T. Wang and G. Hall, ***J. Anal. At. Spectrom***., 2003, **18**, 1443–1451.
3 M. A. Bechlin, E. C. Ferreira and J. A. Gomes Neto, ***Microchem. J***., 2017, **132**, 130–135.
4 R. M. Pereira, V. C. Costa, C. A. Hartwig, R. S. Picoloto, E. M. M. Flores, F. A. Duarte and M. F. Mesko, ***Talanta***, 2016, **147**, 76–81.
5 A. Kinani, H. Salhi, S. Bouchonnet and S. Kinani, ***J. Chromatogr. A***, 2018, **1539**, 41–52.
6 L. Gehrenkemper, F. Simon, P. Roesch, E. Fischer, M. von der Au, J. Pfeifer, A. Cossmer, P. Wittwer, C. Vogel, F. G. Simon and B. Meermann, ***Anal. Bioanal. Chem***., 2021, **413**, 103–115.
7 D. J. Butcher, ***Anal. Chim. Acta***, 2013, **804**, 1–15.

8 M. Resano, M. R. Flórez and E. García-Ruiz, ***Anal. Bioanal. Chem***., 2014, **406**, 2239–2259.
9 B. Welz, H. Becker-Ross, S. Florek and U. Heitmann, *Historical Development of Continuum Source AAS*, 2006.
10 M. Resano, L. Rello, M. Flórez and M. A. Belarra, ***Spectrochim. Acta - Part B At. Spectrosc.***, 2011, **66**, 321–328.
11 M. Resano, E. García-Ruiz, M. Aramendía and M. A. Belarra, ***J. Anal. At. Spectrom.***, 2019, **34**, 59–80.
12 N. Ozbek and S. Akman, ***J. Anal. At. Spectrom***., 2018, **33**, 111–117.
13 P. M. Machado, S. Morés, É. R. Pereira, B. Welz, E. Carasek and J. B. De Andrade, ***Spectrochim. Acta - Part B At. Spectrosc.***, 2015, **105**, 18–24.
14 Y. Xing, H. Fuss, J. Lademann, M. D. Huang, H. Becker-Ross, S. Florek, A. Patzelt, M. C. Meinke, S. Jung and N. Esser, ***Spectrochim. Acta - Part B At. Spectrosc***., 2018, **142**, 91–96.
15 W. Boschetti, M. B. Dessuy, A. H. Pizzato and M. G. R. Vale, ***Microchem. J***., 2017, **130**, 276–280.
16 M. Krawczyk-Coda and E. Stanisz, ***Anal. Bioanal. Chem***., 2017, **409**, 6439–6449.
17 N. Ozbek and S. Akman, ***Food Anal. Methods,*** 2016, **9**, 2925–2932.
18 N. Ozbek and S. Akman, ***Food Chem.,*** 2016, **211**, 180–184.
19 A. R. Borges, Á. T. Duarte, M. da L. Potes, M. M. Silva, M. G. R. Vale and B. Welz, ***Microchem. J***., 2016, **124**, 410–415.
20 H. Gleisner, B. Welz and J. W. Einax, ***Spectrochim. Acta - Part B At. Spectrosc***., 2010, **65**, 864–869.
21 P. Ley, M. Sturm, T. A. Ternes and B. Meermann, ***Anal. Bioanal. Chem***., 2017, **409**, 6949–6958.
22 J. Acker, S. Bücker and V. Hoffmann, ***J. Anal. At. Spectrom***., 2016, **31**, 902–911.
23 N. Ozbek, H. Baltaci and A. Baysal, ***Environ. Sci. Pollut. Res***., 2016, **23**, 13169–13177.
24 N. Ozbek and S. Akman, ***Spectrochim. Acta - Part B At. Spectrosc***., 2012, **69**, 32–37.
25 N. Ozbek and S. Akman, ***Anal. Sci.***, 2013, **29**, 741–746.
26 F. V. Nakadi, M. A. M. S. da Veiga, M. Aramendía, E. García-Ruiz and M. Resano, ***J. Anal. At. Spectrom***., 2015, **30**, 1531–1540.
27 M. S. P. Enders, A. O. Gomes, R. F. Oliveira, R. C. L. Guimaraes, M. F. Mesko, E. M. M. Flores and E. I. Müller, ***Energy and Fuels***, 2016, **30**, 3637–3643.
28 É. R. Pereira, L. M. Rocha, H. R. Cadorim, V. D. Silva, B. Welz, E. Carasek and J. B. De Andrade, ***Spectrochim. Acta - Part B At. Spectrosc***., 2015, **114**, 46–50.
29 N. Ozbek and S. Akman, ***J. Agric. Food Chem.***, 2016, **64**, 5767–5772.
30 É. R. Pereira, J. Merib, H. R. Cadorim, M. Schneider, G. S. Carvalho, F. A. Duarte, B. Welz, J. del C. Menoyo and J. Feldmann, ***Food Control***, 2017, **78**, 456–462.
31 R. L. da S. Medeiros, S. O. Souza, R. G. O. Araújo, D. R. da Silva and T. de A. Maranhão, ***Talanta***, 2018, **176**, 227–233.
32 I. K. S. Oliveira, R. L. S. Medeiros, D. R. Silva and T. A. Maranhão, ***J. Braz. Chem. Soc***., 2018, **29**, 571–578.

33 H. Tinas and S. Akman, ***Spectrochim. Acta - Part B At. Spectrosc***., 2018, **148**, 60–64.
34 A. Guarda, M. Aramendía, I. Andrés, E. García-Ruiz, P. C. do Nascimento and M. Resano, ***Talanta***, 2017, **162**, 354–361.
35 Ľ. Machyňák, F. Čacho, M. Němeček and E. Beinrohr, ***Spectrochim. Acta - Part B At. Spectrosc***., 2016, **125**, 140–145.
36 F. V. Nakadi, M. A. M. S. Da Veiga, M. Aramendía, E. García-Ruiz and M. Resano, ***J. Anal. At. Spectrom***., 2016, **31**, 1381–1390.
37 J. S. de Gois, S. J. M. Van Malderen, H. R. Cadorim, B. Welz and F. Vanhaecke, ***Spectrochim. Acta - Part B At. Spectrosc.***, 2017, **132**, 50–55.
38 F. Cacho, L. Machynak, M. Nemecek and E. Beinrohr, ***Spectrochim. Acta - Part B At. Spectrosc***., 2018, **144**, 63–67.
39 S. Geisler, M. Okruss, H. Becker-Ross, M. D. Huang, N. Esser and S. Florek, ***Spectrochim. Acta - Part B At. Spectrosc.***, 2015, **107**, 11–16.
40 A. Winckelmann, S. Nowak, S. Richter, S. Recknagel, J. Riedel, J. Vogl, U. Panne and C. Abad, ***Anal. Chem***., 2021, **93**, 10022–10030.
41 C. Abad, S. Florek, H. Becker-Ross, M. D. Huang, A. G. Buzanich, M. Radtke, A. Lippitz, V. D. Hodoroaba, T. Schmid, H. J. Heinrich, S. Recknagel, N. Jakubowski and U. Panne, ***J. Anal. At. Spectrom.,*** 2018, **33**, 2034–2042.
42 T. Chen and C. Guestrin, Proc. ACM SIGKDD Int. Conf. Knowl. Discov. Data Min., 2016, 13-17-Augu, 785–794.
43 R. Garde, F. V. Nakadi, E. García-Ruiz and M. Resano, ***J. Anal. At. Spectrom***., 2020, **35**, 2606–2619.
44 L. C. Pomarolli, M. A. M. S. Da Veiga, M. Resano and F. V. Nakadi, ***J. Anal. At. Spectrom***., 2020, **35**, 2305–2314.

Chapter III

Size Characterization of core-shell structures *via* High-Resolution Continuum Source Atomic Absorption Spectrometry and characterization of other metallic nanoparticles and mixtures

- **III.1. Introduction**

Graphite furnace atomic absorption spectrometry (GFAAS) is a suitable technique for the analysis of trace metals in difficult matrices, and especially in solids. However, the technique was developed to provide an analytical signal proportional to the concentration following the Beer-Lambert law. New studies has shown its potential to differentiate among physicochemical species of the same element, like ions and NPs.[1–4] In general, the absence of chemical modifier enables the different atomization processes to occur, while the addition of chemical modifiers produces an intermediate to ensure the same atomization process for samples and standards independently of their original state, suppressing any differences existing during the temperature program.[5] Pd is considered as the universal modifier, because it forms intermetallic compounds with most metals in the periodic table. Thus, the release of the analyte in the gas state is controlled by the adduct formed in the previous steps of the atomization. All studies for sizing NPs have avoided the usage of modifiers, since none of the attempts improved the signal differences for the species analyzed.

The majority of studies conducted about this topic focuses on metallic NPs of Au[2,6] and Ag.[1,7,8] These papers show a trend where a higher energy is required for the complete atomization of bigger NPs. However, it is not possible to elucidate the shape of the NPs[7] and the differences might be related with necessary energy to break all the bonds in the NP (volume relation) or with the atoms in the surface (surface area of the NP). Some papers tried to study the capacity of the method to resolve mixtures of NPs of different sizes. However, NPs signals are complex, and often not resolved enough to use a deconvolution approach.[9] A few multivariate strategies were applied instead with better results.

However, the accuracy of some samples was poor and some mixtures were assigned to a single NP population.[10]

Other elements have shown potential to be sized using GFAAS as well. Vereda-Alonso *et al* published a study where a sizing method is developed to characterize magnetic NPs (magnetite) using the upslope of the signal of Fe.[3] Another study was capable of identifying Zn and ZnO NPs calculating the t_{delay} (defined as the difference in time between the appearance of peak maximum and the start of the atomization step) of both species.[4] Overall, the elements sharing this behavior show a mild atomization temperature (around 2000ºC) and a relatively high electric and thermal conductivities.[11]

However, some species did not show the same trend as the others. A study conducted by Leopold *et al* tried to estimate the sizes of PdNPs and PtNPs unsuccessfully. It seems that these elements require a higher atomization temperature, and its own modifier effect might suppress the size differences during its atomization.[8]

In recent years, core shell structures comprised of bimetallic nanoparticles are getting more importance due to the combined properties of both nanostructures, as well as even new properties derived from the new structure, broadening their applications.[12–15] These engineered materials have been gaining more importance over simple NP structures comprised by only one element. Their size characterization is usually carried out using electron microscopies. However, the mechanisms for screening and sizing already studied for NPs *via* GFAAS might be an additional tool to characterize CSNPs.

In this manuscript, different core-shell NPs and mixtures of Au and Ag NPs and ions were analyzed *via* AAS to study their atomization mechanisms and estimate

their sizes using the NPs of the elements of the CSNPs. Additionally, other CSNPs of these elements with silica were also tested. Additionally, NPs of copper, platinum and silica were studied to assess the capabilities of the technique to identify and characterize different sizes of NPs and ions containing those elements.

- **III.2. Experimental**

III.2.1. Instrumentation

All the measurements were carried out using a contrAA 800G high-resolution continuum source atomic absorption spectrometer (HR CS GFAAS, Analytik Jena AG, Jena, Germany) equipped with transversally-heated graphite tube atomizers that incorporated a platform (Analytik Jena AG). The main details and future perspectives about this type of instrument can be found elsewhere.[16,17]

The samples and reagents were pipetted automatically with an autosampler (Analytik Jena AG).

III.2.2. Standards, reagents, and samples

The solutions were prepared with reagents of analytical grade or higher purity. Deionized water purified by a Milli-Q system (Millipore, Bedford, USA) was used for the solutions and suspensions of NPs.

Standards of 1000 mg L^{-1} of Au (Merck, Darmstadt, Germany), Ag (Sigma-Aldrich), Pt (Merck, Darmstadt, Germany), Si (Merck, Darmstadt, Germany) and Cu (Merck, Darmstadt, Germany) were used to prepare all the ionic solutions and standard calibrations. Nanoparticles utilized in this study are compiled in **Tables 1 and 2.** Before analysis, NPs were suspended in miliQ water until proper concentration.

Table 1: NPs evaluated in this study.

NPs	Coating	Concentration (mg mL^{-1})	Diameter (nm)	Manufacturer
Au 10	PEG carboxyl	0.053	8.8 ± 0.4	Nanocomposix
Au 20	PEG carboxyl	0.052	20.4 ± 0.5	Nanocomposix
Au 30	PEG carboxyl	0.052	28.0 ± 0.9	Nanocomposix
Au 50	PEG carboxyl	0.05	50.3 ± 2.3	Nanocomposix
Au 100	PEG carboxyl	0.053	102.2 ± 4.2	Nanocomposix
Ag 10	Citrate	0.02	9.9 ± 1.9	Nanocomposix
Ag 20	Citrate	0.022	19.9 ± 2.8	Nanocomposix
Ag 30	Citrate	0.021	30.0 ± 3.0	Nanocomposix
Ag 50	Citrate	0.021	51.0 ± 6.0	Nanocomposix
Ag 80	Citrate	0.021	79.0 ± 7.0	Nanocomposix
SiO_2 20	silanol	5.2	21.4 ± 2.7	Nanocomposix
SiO_2 80	silanol	10.5	81.0 ± 6.0	Nanocomposix
Cu 25	-	solid	25.0 ± 1	Merck
CuO 50	PVP	1.03	48.0 ± 7.0	Nanocomposix
Pt20	-	0.763	18.5 ± 11.0	Hiq Nano
Pt80	-	1.144	85.0 ± 3.5	Hiq Nano

Table 2: CSNPs evaluated in this study.

Core Shell Nanoparticle	Core	Shell	Coating	Diameter (core)/nm	Diameter (shell)/nm	Concentration (core)/mg L^{-1}	Concentration (shell)/mg L^{-1}	Particle concentration/mL	Total size/nm
Res660	Si	Au	PVP 40kDa	79 ± 3	58	-	54	2.50E+09	137
Res800	Si	Au	PVP 40kDa	117 ± 5	38	-	52	2.50E+09	155
Res980	Si	Au	PVP 40kDa	198 ± 10	44	-	53	8.10E+08	242
Au@Si20	Au	Si	Silanol	17 ± 1	40	1070	-	2.00E+13	57
Au@Si50	Au	Si	Silanol	54 ± 5	36	1080	-	6.80E+11	90
Au@Si70	Au	Si	Silanol	70 ± 7	30	1100	-	3.20E+11	100
Au@Ag20	Au	Ag	Citrate	7.0 ± 0.8	13.4	100	960	2.20E+13	20.4
Au@Ag60	Au	Ag	Citrate	30 ± 3	30	240	710	6.50E+11	60
Au@Ag80	Au	Ag	Citrate	51 ± 6	34	400	690	2.70E+11	85
Ag@Si50	Ag	Si	Silanol	50.5 ± 5.2	42.8 ± 2.6	1000	-	1.50E+12	93.3

III.2.3. Measurement conditions for NP analysis

The temperature program and transitions monitored for the analysis are collected in **Table 3**. All signals are integrated using signal area and 3 measurement pixels (central and 2 lateral pixels).

Table 3: Instrumental conditions used for monitoring the different NPs.

Temperature Program				
Step	Temperature/ ºC	Ramp/ ºC s^{-1}	Hold/ s	Ar gas flow/ L min^{-1}
Drying	90	3	20	2
Drying	110	5	10	2
Pyrolysis	500	50	20	2
Pyrolysis	700	100	10	2
Gas adaption	700	0	5	0
Atomize	2200^{+}	100*	6	0
Clean	2500	500	4	2

$^{+}$ 2500ºC for Si and Pt monitoring
* 300ºC s^{-1} for Si monitoring

Instrumental parameters used to monitor the analytes by HR CS GFAAS	
Au	242.795 nm
Si	251.611 nm
Pt	265.945 nm
Cu	324.754 nm
Ag	328.068 nm
Number of detector pixels summed per line	3
Sample volume	10 µL

Conditions were optimized to provide the best separation in temperature and time, but without compromising the time of analysis and signal-to-noise ratio for all the elements of interest. Only Si needed a higher ramp, due to the higher temperature needed to atomize it. At 100ºC s^{-1} the signal does not increase significantly from the baseline, thus a faster ramp was selected for the study of SiO_2NPs.

III.2.4. Software for data analysis

All t_{delays} calculated in this paper were calculated using OriginPro 2021b. Two methods were applied, signal derivative and peak fitting. The first strategy was already studied in the literature.[18] In this work, a strategy based on fitting the peak into a known symmetrical function to calculate the atomization delay was also tested.

- **III.3. Results and discussion**

III.3.1. Sizing/Screening Copper, Platinum and Silica Nanoparticles and ions

Copper, platinum and silica nanoparticles and ions were analyzed to get information about size with HR CS GFAAS. The NPs analyzed are compiled in **Table 1** with the information about particle concentration, size, and concentration. Solutions/dispersions of Cu (II), CuNPs of 50 nm and CuONPs of 50 nm were diluted to a concentration of 100 µg L^{-1} using ramps of 50, 100, 200 and 500ºC s^{-1} (see **Figure 1**). The results show a monomodal signal at low ramps, and the increase of the ramp provides a better signal-to-noise ratio in detriment of the symmetry, with a noticeable tail at 500ºC s^{-1}. Signal for atomization ramp of 500ºC s^{-1} was set for a duration of four seconds in the experiments at 500ºC s^{-1} atomization ramp.

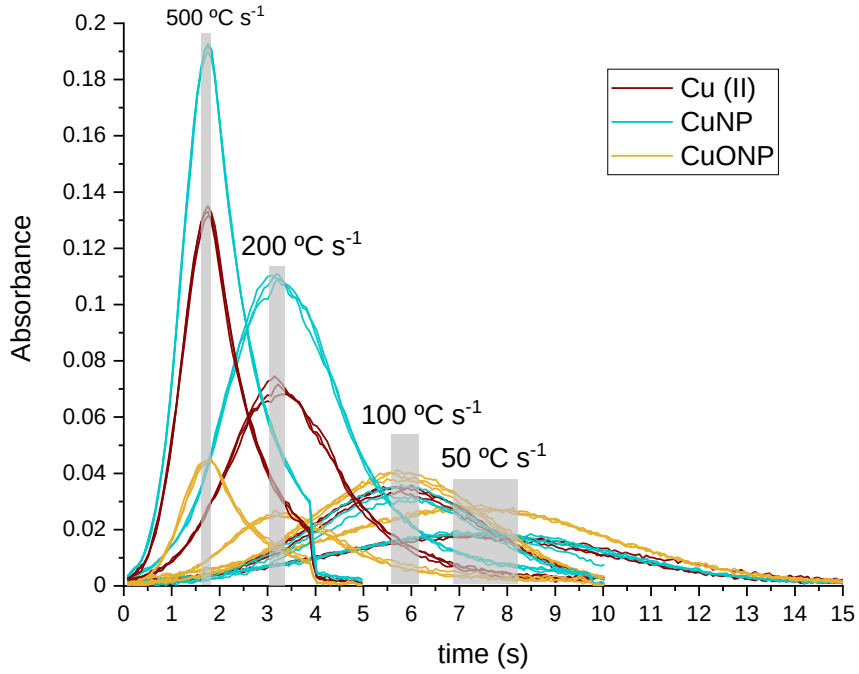

Figure 1: Absorbance spectra of three species of copper (Cu (II), CuNPs of 50 nm and CuONPs of 50 nm) applying 50, 100, 200 and 500ºC s^{-1} atomization ramps. The gray area highlights the peak maxima.

None of the conditions evaluated showed differences in terms of peak maximum for the three species evaluated, which might indicate that the atomization process is not controlled by the size and probably an intermediate is formed.

Pt was also studied using 3 ramps of 3000, 500 and 100ºC s^{-1} and 3 species of Pt: Pt (I), PtNP of 20 nm and PtNP of 80 nm diluted to a concentration of 100 µg L^{-1} (see **Figure 2**). The temperature program selected needed a higher atomization temperature. Results show a sharp increase of the signal and then a tail or shoulder once the signal descends for 3000 and 500ºC s^{-1}. For 100ºC s^{-1}, the atomization process is sufficiently slow to provide a more symmetrical signal. The maxima for the signals obtained from ions and NPs overlap at every ramp,

and like for the Cu species, no differences are observed at any ramp selected. Brand *et al* already tried to develop a screening/sizing method for Pt, showing that no significant differences were achieved.[8] Our study confirms the same results.

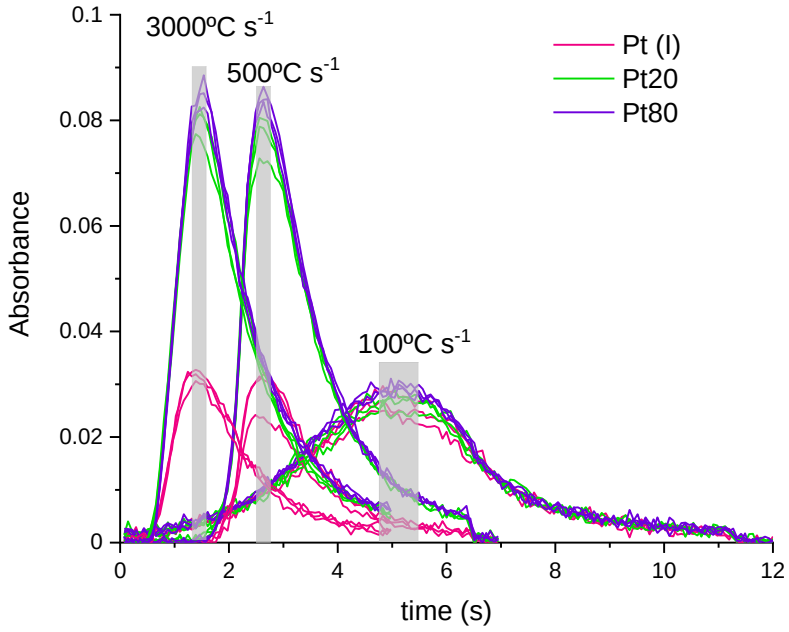

Figure 2: Absorbance spectra of three species of Pt (ionic solution, PtNPs of 20 nm and PtNPs of 80 nm) using 100, 500 and 3000ºC s^{-1} atomization ramp. The gray area highlights the peak maxima.

Finally, suspensions of silica NPs of 20 nm and 80 nm and a solution of Si (IV) of 500 µg L^{-1} were analyzed using ramps of 3000, 500 and 300ºC s^{-1} (see **Figure 3**). No differences were observed for any of the ramps tested. Thus, silica species do not atomize following a size dependent mechanism. A ramp of 100ºC s^{-1} was studied as well, but the refractory nature of Si made impossible to achieve a good analytical signal, due to a wide profile and low intensity signals, which were almost undetectable from the baseline, as discussed before.

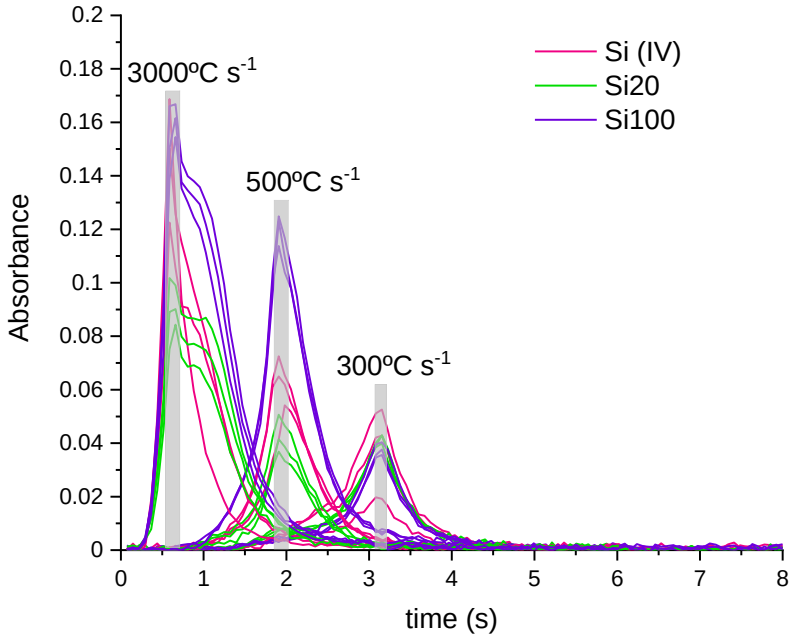

Figure 3: Absorbance spectra of three species of Si (Si (IV), SiO_2NPs of 20 nm and SiO_2NPs of 100 nm) using 300, 500 and 3000ºC s^{-1} atomization ramp. The gray area highlights the peak maxima.

In conclusion, unlike what occurs with other elements (most notably Ag and Au), none of these elements have shown any difference in their atomization mechanisms as a function of the physico-chemical species measured.

Besides, the use of high ramps provided more asymmetrical signals, adding a tail to the signal. However, if the ramp is sufficiently slow, the tail is eliminated, and a more symmetric function is achieved, which improves the possibility to apply a fitting strategy to simulate the peak.

III.3.2. Sizing AuNPs: Au peak fitting, profile and t_{delay} vs concentration

As discussed before, several methods have been developed for sizing and screening AuNPs with GFAAS. All the approaches require the calculation of a parameter to estimate the size or to discriminate among species. The parameters assessed for Au in previous studies are called atomization delay (t_{delay}) and atomization rate (k_{at}). In short, these parameters represent the time at which the absorbance reach its maximum, and the upslope of the signal, respectively. The maximum of the signal for AuNPs is shifted towards longer times, and the bigger the NP is, the bigger the shift. k_{at} also increases for bigger NPs, but it is also influenced by the concentration of the element,[19] thus, we don't recommend using the atomization rate as a sizing parameter due to the necessity of a precise control in the concentrations of samples and standards.

For calculating the t_{delay} of a measure, two strategies were compared: derivation and peak fitting. In the first one, the spectrum is derived, and the inflexion point associated to the maximum of the signal will correspond to its atomization delay (i.e., absorbance = 0). Moreover, peak fitting can provide the t_{delay} too. However, there are several aspects that will influence the fitting. Only symmetrical signals can be fitted in a Gaussian or Lorentzian single peak function. Thus, if the signal presents a shoulder, either the derivative or using a multiple peak fitting might be a better approach. Also, asymmetrical functions can be used. However, in that case the maximum is shifted, and the t_{delay} cannot be determined accurately.[20]

All Au signals for NPs from 5 nm to 100 nm were fitted into a single peak fit following a pseudo-Voigt profile (combination of Gaussian and Lorentzian functions with different peak width), the peak fitting was evaluated through the convergence of chi-square tolerance value: a value of $\leq 10^{-9}$ needs to be reached to be considered a successful fitting. However, the atomization process of Au (III)

is variable. For a worn-out tube, Au (III) atomizes producing a signal comprised of two peaks; the first peak tends to be higher (but that is not always the case) and appears earlier than the usual signal for NPs, while the second peak appears immediately after as a shoulder/tail at times corresponding to the atomization of AuNPs (see **Figure 4**). The appearance of this tail might be related with a reduction process of gold *in situ* during the temperature program or caused by the interaction with the graphite pores. In general, the atomization process of NPs remains invariable, following a unimodal signal fitted in a Voight profile.

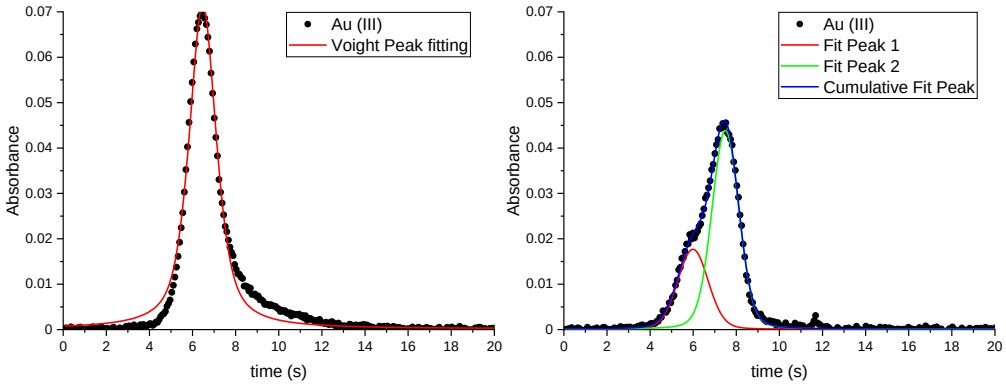

Figure 4: Absorbance of two solutions of Au (III) of 50 µg L^{-1} in a) a new graphite tube and b) a worn-out graphite tube.

For Au(III), the t_{delay} is not constant with the concentration (see **Figure 5**); thus, it cannot be included in the size estimation curve. NPs, on the other hand, provide a stable t_{delay} regardless of their concentration. Hence, a fast-screening method for ions and NPs only required to measure the species at 2 different dilutions. If t_{delay} changes significantly, Au (III) ions are presented in the sample. Otherwise, the sample contains only NPs. Also, the presence of a tail or even a double peak is a good indicator of the presence of Au (III) ions as discussed earlier (although

a mixture of NPs of very different sizes can also produce a double peak, as will be discussed later), but in new tubes monomodal signals can occur, as shown in **Figure 4**. Therefore, ions are easily distinguishable by checking the evolution of the t_{delay} at different concentrations, but its presence hampers the characterization of NPs.

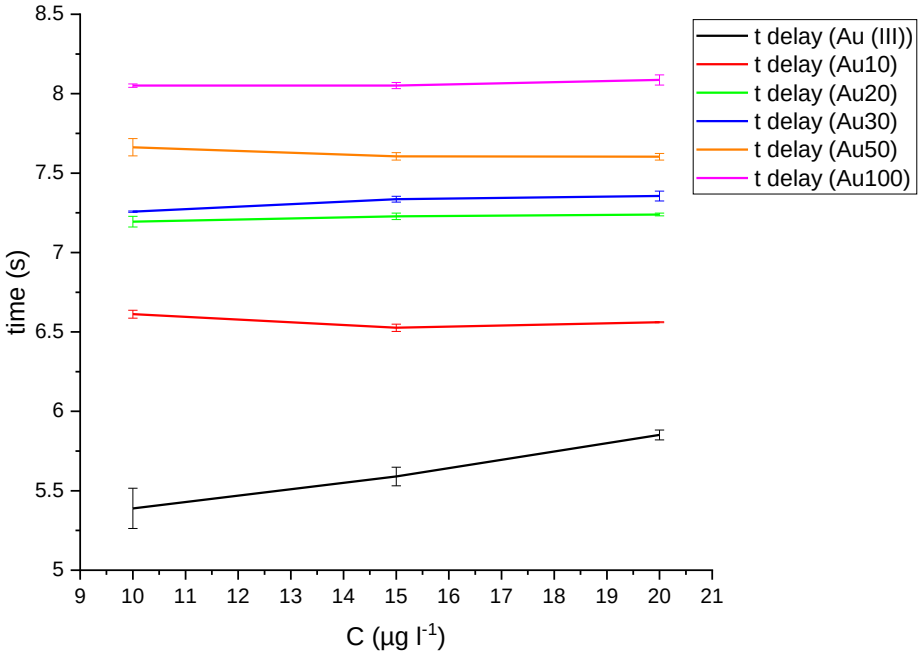

Figure 5: Dependency of t_{delay} with concentration of an ionic solution and 3 suspensions of NPs of 10, 20, 30, 50 and 100 nm.

The progression of the t_{delay} vs the size of the NPs show that small NPs can be differentiated with a better resolution due to the higher sensitivity, while bigger NPs tend to provide a closer t_{delay} value (see **Figure 6**). Two different approaches were selected to determine the size of the samples: 1st, fitting the curve in two linear ranges, the first one covering from 5 nm to 20 nm (n= 3, t_{delay}= 0.048 S + 6.93, R^2= 0.995; S: NP diameter), with a higher sensitivity, as explained before,

and a second one with less size resolution (slope) from 20 to 100 nm (n= 4, tdelay= 0.008 S + 7.76, R^2 =0.995). Second, a logarithmic fitting covering the whole range of NPs, from 5 nm to 100 nm (n= 6, tdelay = 0.469 ln(S) + 6.398, R^2= 0.983). The performance of both approaches will be further discussed in sections 3.4. and 3.5.

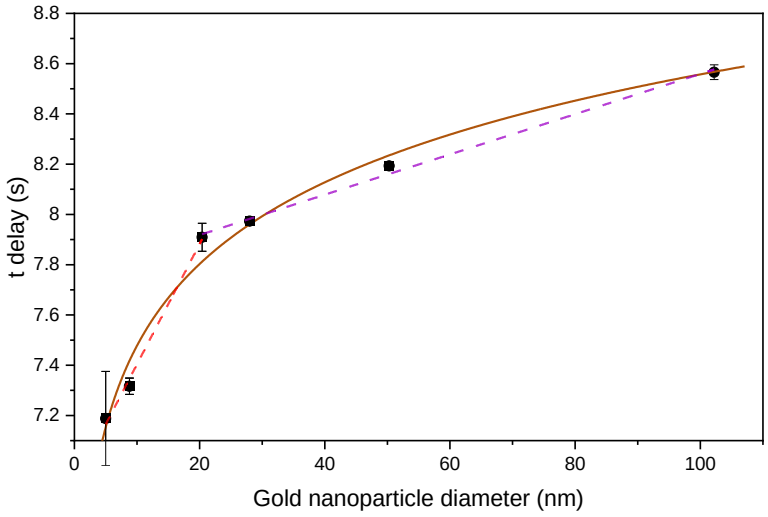

Figure 6: Atomization delays of NPs of 5, 10, 20, 30, 50 and 100 nm as function of their NP diameter. The solid brown curve follows a logarithm trend, the red and purple dotted lines follow a linear trend

To sum up, AuNPs and ions are better fitted into a Voigt profile, showing a single monomodal peak for NPs and a more variable profile for ions, depending on the state of the tube. Finally, the size estimation curve follows a logarithmic curve that can also be described as 2 linear curves with a change in slope at 20 nm.

III.3.3. Ag peak fitting, profile and t_{delay} vs concentration

Solutions/dispersions of Ag(I) and AgNPs of 10, 20, 30, 50 and 80 nm were diluted until a concentration of 20 µg L^{-1}

Gauss was the best function for Ag fittings. However, the number of peaks to adjust was not clear. Two (P1, P2) to three peaks (P1, P2, P3) seem to fit better the overall profile of the signals (see **Figure 7**). Linear and logarithmic approaches were assessed in the next sections to evaluate their performances (see **Figure 7**).

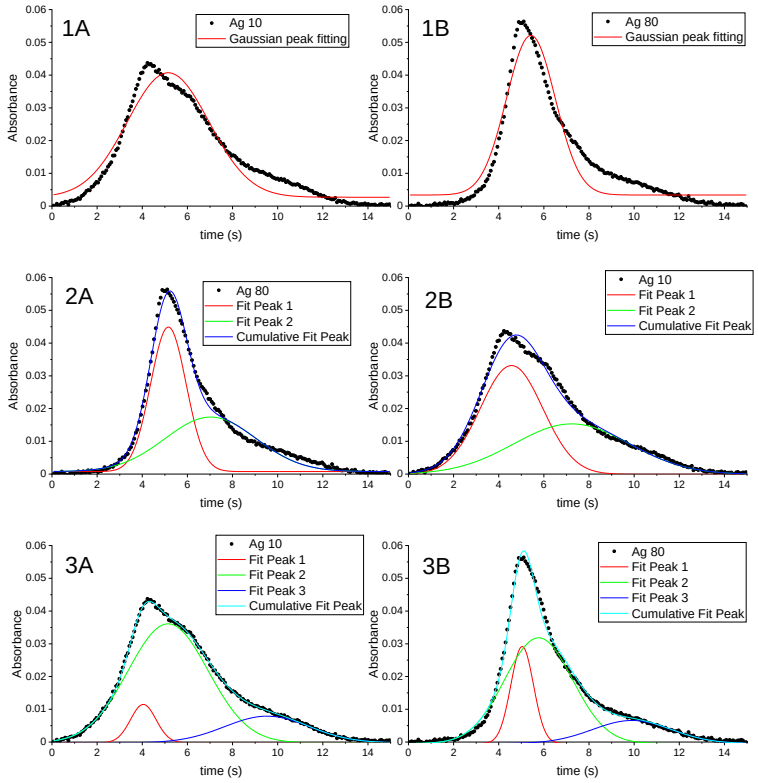

Figure 7: Absorbance signals registered for two dispersions of AgNPs fitted as a Gaussian distribution 1A) 10 nm, one peak; 1B) 80 nm, one peak; 2A) 10 nm, two peaks; 2B) 80 nm, two peaks; 3A) 10 nm, three peaks; 3B) 80 nm, three peaks.

The different populations present in the signals were already exploited for the development of a method to identify free ions coming from oxidized AgNPs by Degenkolb *et al.*[21] A pre-peak appears after the NP associated signal indicating the existence of ions. This, the presence of multimodal signals in AgNP seem like a good indication of the state of the NPs, and only fresh new dispersions might

present a simpler signal profile. Brandt et al reported the presence of three different populations in Au (III) solutions, explained by free ions released, agglomeration *in situ*, and migrated ions in the furnace.[6,8,18] Maybe AgNPs are less stable and more prone to be oxidized and aggregate, however it is not clear that this effect is not caused by the interaction of the graphite with the Ag (I) and AgNPs during the pyrolysis or atomization steps.[8]

The dependency of the three populations and the size of the NPs studied was assessed. If the previous assumptions are right, the first peak of all AgNPs should be associated to Ag ions released from the NP, the second peak to the original AgNPs, and the last one to aggregates and migrated ions in the furnace.

Two functions were evaluated to fit the data, linear and logarithmic (see **Figure 8**). The linear regression results for the three peaks showed a poor correlation for peaks one (n=5, t_{delay} = 0.0099 S + 4.16, R^2 =0.73) and three (n=5, t_{delay}= 0.00871 S + 8.96, R^2 = 0.81), but peak two showed a better correlation (n=5, t_{delay}= 0.0096 S + 4.99, R^2 = 0.97). The results from the logarithmic regression provided a similar outcome. Peaks one (n= 5, t_{delay} = 0.366 ln(S) + 3.30, R^2 =0.85) and three (n=5, t_{delay} = 0.251 ln(S) + 8.43, R^2 = 0.58) did not completely fit into a logarithmic function. On the other hand, peak two (n=5, t_{delay}= 0.340 ln(S) + 4.21, R^2 = 0.98) also showed a good correlation using the logarithmic fitting as well.

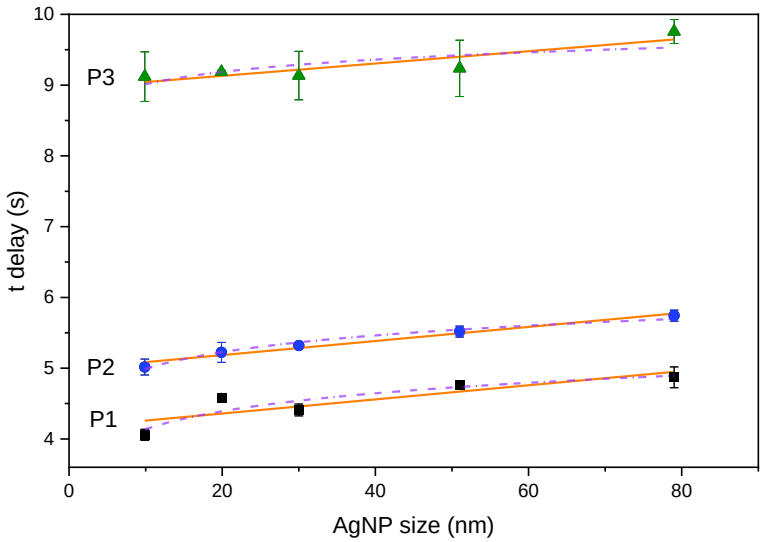

Figure 8: Atomization delays of P1, P2 and P3 as function of the AgNP size. Solid lines follow a linear trend and the short dash patters corresponds to the logarithmic fit.

III.3.4. Resolving mixtures of NPs

Mixtures of AgNPs are already studied by Gruszka *et al*.[9] Results showed that the signals of AgNPs mixtures does not resolve in any case, showing only 1 maximum per signal. The complex atomization mechanism overlaps the different size populations of the AgNPs and Ag(I) in mixtures. Therefore, mixtures cannot be estimated for silver using this methodology. Another strategy worth mentioning was the application of multivariate methods. Partial component analysis (PCA) and machine learning (ML) were evaluated, but results showed inconsistencies in both approaches.[10]

Due to the impossibility to identify different populations, we considered the signal of a mixture as an unknown sample and calculate the size of the NP by interpolating its t_{delay} in the size curve calibration. Thus, dispersions containing AgNPs of 10, 20, 50 and 100 nm were studied as if they were dispersion of NPs

with one main population. The error is calculated comparing the experimental size estimated and compared to the average size and average volume of the mixtures Results are shown in **Table 4**. Sizes were calculated by fitting the signals into three gaussian peaks and calculate their t delay. Afterwards size is calculated using the regression models introduced in the previous sections.

Table 4: Mixtures of AgNPs of sizes from 10 to 100 nm of 20 µg L^{-1} each.

	Size/nm	error% (vs average size)	error% (vs average volume)
Ag10 & Ag80	41.1 ± 1.4	-7%	-34%
Ag10 & Ag100	64.0 ± 4.1	19%	2%
Ag20 & Ag80	44.5 ± 3.1	-10%	-29%
Ag20 & Ag100	62.3 ± 3.7	6%	-20%
Ag30 & Ag50	36.4 ± 4.6	-10%	-53%
Ag50 & Ag80	63.3 ± 4.0	-3%	-19%

Both logarithmic and linear approaches using the P2 of the Ag regression models provided similar results, differing in 1% between the two models. The size results in mixtures of AgNPs were compared to the average size and average volume of the mixtures prepared, with errors ranging between -10% and 19% when the results are compared to the average size. Results compared to the volume average were underestimated with errors between -53% and -19%. Only mixture Ag10 & Ag100 provided a lower error compared to the average volume. Overall, even though the signals of the mixtures are not resolved, the average size can be calculated with a very reasonable accuracy.

The resolution of mixtures of AuNPs and ions have not been studied in the literature yet, and since their mechanism is much simpler, it might easier to obtain resolved signals in some cases. Several mixtures of NPs and ions were prepared, with increasing differences in size to assess the capacity to resolve the maximum of the mixtures. All mixtures were treated as unknown samples, thus, resolved

maximums will be treated as two different populations and when only one peak is distinguishable, the size of that maximum (t_{delay}) will be estimated. **Table 5** shows the results obtained when the mixtures are considered as one population. In this case, except for the Au (III) & Au 50 mixture, it can be seen that a screening of the average size is feasible, with the error increasing as the sizes of the two populations are closer.

Table 5: Size estimation and error committed for mixtures of Au (III) and AuNPs of 50 µg L^{-1} applying the linear regression model (n=3).

Mixtures	Size/nm	error % (vs average size)	error % (vs average volume)
Au(III) & Au50	134.4 ± 27.3	433%	237%
Au10 & Au100	50.7 ± 2.1	-9%	-38%
Au20 & Au100	72.7 ± 2.4	19%	-11%
Au30 & Au100	76.9 ± 0.2	18%	-6%
Au50 & Au100	103.5 ± 0.8	36%	23%
Au20 & Au50	55.6 ± 1.4	57%	36%

Mixtures of ions and relatively big NPs (50, 100 nm) do present a double peak with two clear maxima. Also, mixtures of Au5 and Au100 are resolved too, and finally two mixtures of Au5 and Au50, and Au10 and Au100, show a profile where two peaks can be identified but not resolved enough to provide an accurate t_{delay} (**figure 9**). In these last two cases, the signals were fitted into one and two peaks. The rest of the mixtures exhibit a single peak profile where no populations can be discerned.

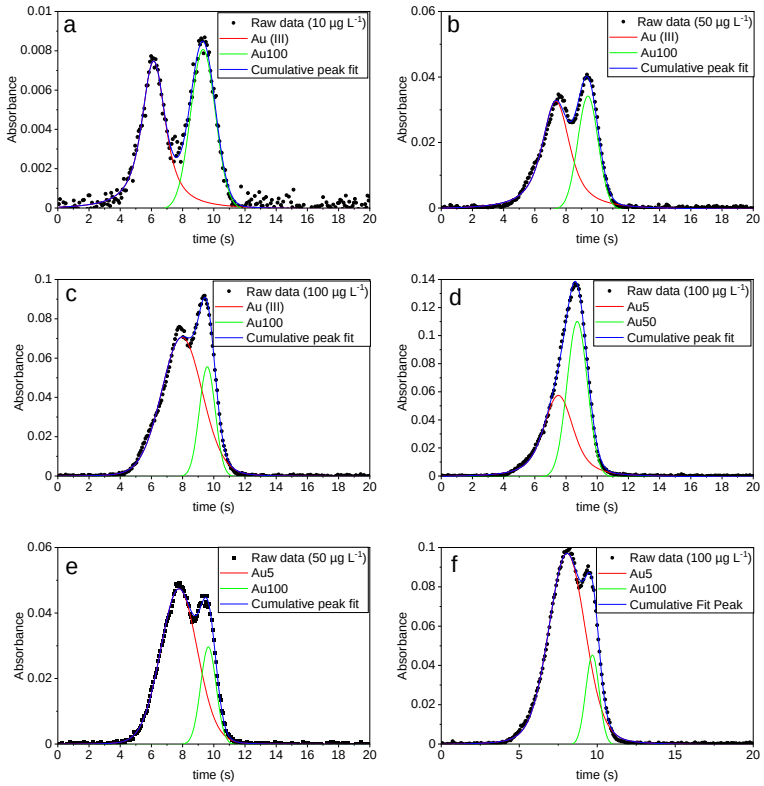

Figure 9: Absorbance signals registered for aqueous suspensions containing mixtures of Au (III) and Au100 at a) 10, b) 50 and c) 100 µg L^{-1}; and three additional dispersions of d) Au5 and Au50 (100 µg L^{-1}), e) Au5 and Au100 (50 µg L^{-1}) and f) Au5 and Au100 (100 µg L^{-1}).

The mixtures with Au (III) might contribute to the second peak, due to its trend to form a tail/shoulder, but in mixtures resolved with only NPs, the areas fitted are proportional to the absorbances of the single species measured. Also, in both resolved and non-resolved mixtures, when Au (III) is present, the t_{delay} calculated at three different concentrations in the mixture Au (III) & Au100 for the first peak varied significantly, with equivalent sizes of 0.6 nm to 8.8 for a concentration of 10 µg L^{-1} to 100 µg L^{-1} respectively, while mixtures with only NPs show a more stable size for the different dilutions, as demonstrated in the results of Au5 &

Au100 at 50 and 100 µg L^{-1}. Thus, the change in concentration is especially useful to detect the presence of ions in a dispersion/solution, where its t_{delay} will be shifted significantly, as discussed before.

Three replicas were measured under the conditions optimized previously. The results are shown in **Table 6.**

Table 6: Size estimation and error committed for resolved mixtures of Au (III) and AuNPs applying the linear regression model (n=3).

		Peak 1		**Peak 2**	
Resolved Mixtures	Concentration / µg L^{-1}	Size AuNP	error%	Size AuNP	error%
Au(III) & Au100	10	0.6 ± 0.1	298%	95.8 ± 10.7	-6%
Au(III) & Au100	50	4.2 ± 0.2	2732%	114.9 ± 8.4	12%
Au(III) & Au100	100	8.8 ± 2.5	5906%	136.7 ± 10.0	34%
Au5 & Au50	100	4.4 ± 1.6	-12%	35.6 ± 1.6	-29%
Au5 & Au100	50	9.0 ± 2.3	80%	139.9 ± 36.2	37%
Au5 & Au100	100	11.4 ± 2.2	128%	109.8 ± 9.4	7%

The results show that resolved mixtures always provide overestimated values for the first peak except for Au5 & Au50. The presence of Au(III) worsens the results in mixtures, and this effect is exacerbated when its concentration increases but it does not affect the second peak if that is sufficiently resolved, like in Au(III) & Au100. The population giving rise to the second peak can, on the other hand, be sized with reasonable accuracy.

In conclusion, from the mixtures studied, only a few comprised of highly differing sizes of AuNPs and/or Au (III) showed a bimodal signal. The average of mixtures can be estimated for AgNPs and if peak maxima are not fully resolved for AuNPs, with varying degree of accuracy. In the case of resolved peak maxima for AuNPs, the presence of Au(III) worsens the sizing of the other AuNP, probably due to the tail formed during Au(III) atomization, which overlaps with the AuNP signal. This

effect increases with the concentration of Au (III). Still, it is feasible to size the AuNP with reasonable accuracy for some mixtures.

III.3.5. Core shell size estimation

In this section the response of t_{delay} of different CSNPs is assessed to estimate the size of the overall NP and its two components. Also, the possibilities of the technique for screening and possible inconsistencies are discussed for CSNPs of Au, Ag and SiO_2.

III.3.5.1. Size estimation of CSNPs of Au and Ag

HR CS GFAAS capacities to differentiate among NP sizes of Au and Ag opens the question of how CSNPs of these elements will atomize under the same conditions. Thus, three CSNPs, denoted as Au@Ag20, Au@Ag60 and Au@Ag80 (see **Table 1**) were dispersed in milli-Q water until concentrations of 50 μg L^{-1} and 20 μg L^{-1} for Au and Ag, respectively, for their monitoring *via* HR CS GFAAS. Then, the t_{delay} Au and Ag were calculated and using the size estimation curves of sections 3.2. and 3.3., and the sizes of both core and shell were estimated. Linear and logarithmic approaches for both Au and Ag provided similar results.

Figure 10 shows the percentage of error and the uncertainty (expressed as RSD%) obtained in two different days, when comparing the size calculated using the size estimation curves for Au and Ag and the reference values provided by manufacturer (see **Table 1**).

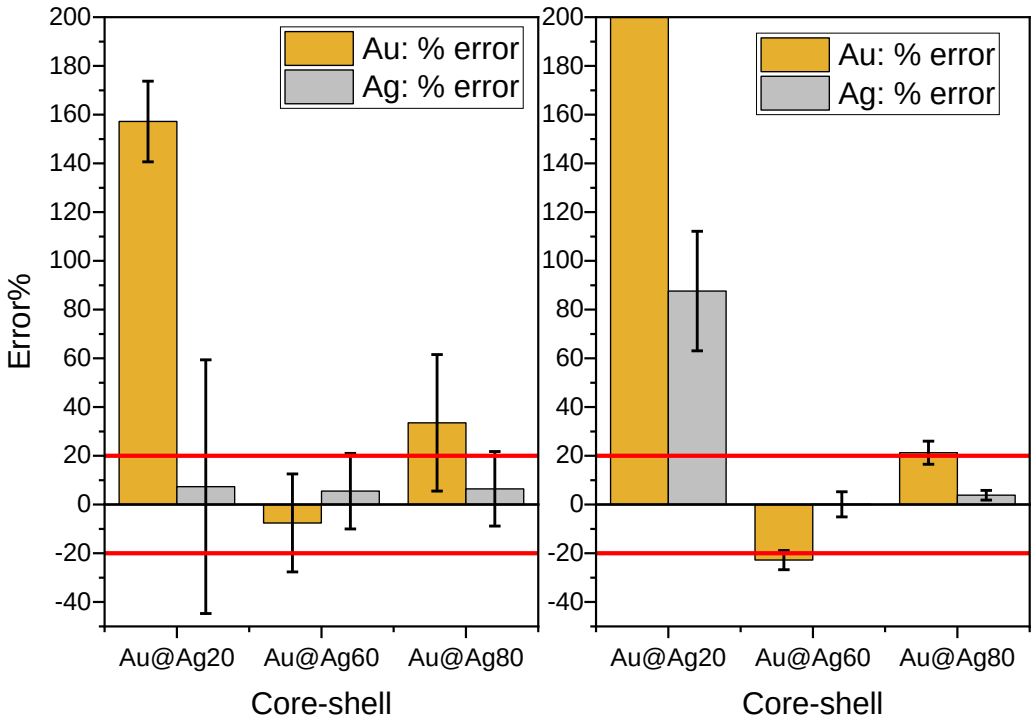

Figure 10: Percentage of error committed in the size estimation of Au@Ag20, Au@Ag60 and Au@Ag80 in two different days. The error bar for Au@Ag20 is out of scale, with a value of 467 ± 76%.

The size estimated values for Au-core were highly biased. Especially for Au@Ag20, the smaller CSNP. Errors for Au@Ag60 and Au@Ag80 were between -23 and 34%, closer to the reference values, but still high for characterization purposes.

Silver-shell sizing showed more promising results. Due to the different geometry of the shell compared to spherical NPs used as references, the size calculation could be related to the total volume of the atoms comprising the shell, or to the overall volume of the CSNP. The figure shows the error related to the total size of NP. Results for sizing Ag-shell in Au@Ag60 and Au@Ag80 showed a good correlation with the total size of the CSNP, with error <6.5% for all the estimations,

confirming this correlation with the overall volume of the CSNP. However, the results of Au@Ag20 suggests that estimating NPs of 20 nm or smaller lead to inaccurate and/or imprecise results.

Clearly, this methodology did not provide good quantitative results for Au-core results. Maybe the atomization processes of Au@AgNPs cannot be compared to AuNPs due to the encapsulation in the Ag-shell.

III.3.5.2. Size estimation of CSNPs of Au/Ag with SiO_2

CSNPs of SiO_2 were studied in this section, to evaluate the effect of SiO_2 on the atomization processes of Au and Ag. Thus, suspensions of Au@SiO_2 (20, 50 and 70 nm) and SiO_2@Au (denoted in **Table 1** as Res660, Res800, Res980) were diluted until reaching concentrations of 50 μg L^{-1} and 200 μg L^{-1} for Au and Si monitoring, respectively, and using the same procedure for Au sizing applied in previous sections.

An alternative strategy was applied for the estimation of SiO_2 core size in SiO_2@Au CSNPs (Res660, Res800 and Res980), without the need to use the Si signal obtained *via* HR CS GFAAS for sizing, which was deemed before as unsuitable.

As discussed before, sizing the Ag-shell in the previous section led to a value near the overall size of the CSNP, and its concentration determined, the volume associated that will occupy the core (V_{core}) can be calculated if the particle number is known (P_N). Hence, the total concentration (C_{shell}) is divided by the particle number concentration, provided by the manufacturer, obtaining the mass of shell per CSNP. Then, the volume occupied by the shell is calculated using its density (d_{shell}). Thus, the volume of the core is calculated subtracting the volume of the

shell to the overall volume calculated sizing the shell, as shown in **Equation 1**. Results are shown in **Figure 11**.

$$\text{Equation 1: } V_{core} = V_{exp} - \frac{C_{Shell}}{P_N \, d_{Shell}}$$

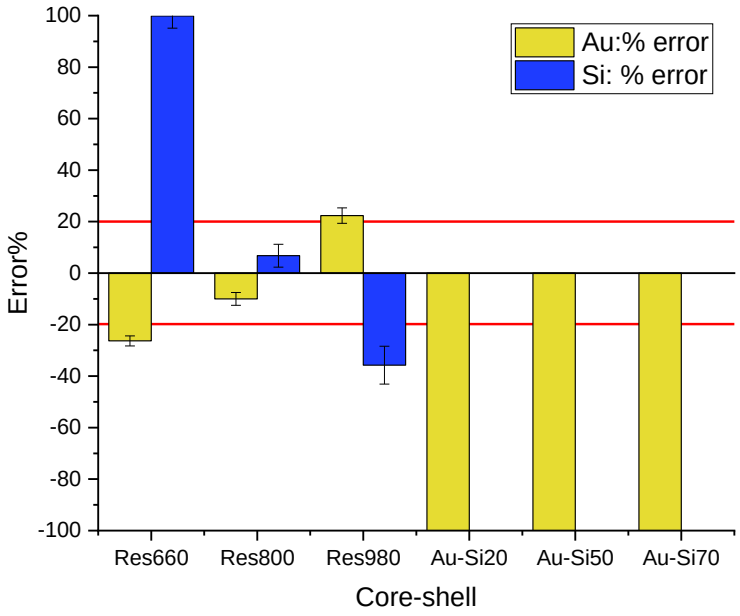

Figure 11: Error% committed in the size estimation of three Au@SiO_2NPs and three SiO_2@AuNPs

No information about size could be obtained from the measurements of Au@SiO_2, due to the encapsulation of the Au-core inside the SiO_2-shell, a more refractive material and therefore the release of Au from core is limited until the shell distorts, but the silica signal appears later, showing that the atomization of Au starts before the Si signal. These results suggest that the CSNP breaks first, then the Au-core atomizes and, afterwards, all the silica, that remains inside the furnace, is atomized too at a high temperature. Also, the Au signal profile is modified, fitting better in a Pearson IV function. Its time of appearance is extremely delayed, making this method perfect to identify silica-shell CSNPs. An

Ag@SiO_2 (results not shown in **Figure 11**) was also monitored, and the same trend was observed.

On the other hand, the t_{delay} of Au-shell measured for Res600, Res800 and Res980 were out of range of the size calibration used, and size was estimated by extrapolation. Then, the sizes were calculated using the logarithmic and the linear correlations. The results from the logarithmic curve show a higher error (between 68% and 173%) than the reference value, while the linear method provides a lower error (33%, 3% and -19% for Res660, 800 and 980 respectively), which might indicate a preference for the linear approach, at least if extrapolation is necessary.

The results for the Si-core in SiO_2@AuNPs derived from Eq. 1 were not accurate. The nature of the calculations for the SiO_2 core also provides a trend in the error that is easily recognizable. The error committed in the Au shell determination will control the error in the core result. In **Figure 11**, the results for Au-shell in Res660, Res800 and Res980, show an error of -26%, -10% and 22% respectively. Once the SiO_2-core is determined, the error follows the opposite trend, if the size estimated for the core is biased low, the core will be overestimated, and vice versa.

Therefore, the size of the core can be estimated only if the particle number is already established, and concentration and size are estimated accurately. Otherwise, results are highly biased.

- **III.4. Conclusions**

It is not feasible to differentiate among the different species of Cu, Pt and SiO_2.

Au atomizes following a Voigt profile and a single peak, while Ag fits better in a Gauss function with two to three peaks, preferably. In any case, the peak that

controls the global maximum of the signal provides the best results for sizing NPs. Derivative and peak fitting provides the same parameters. Size dependent with time/temperature follows a logarithmic trend for Au, that could also be explained as two linear regions with a change in slope at 20 nm. Interpolated results show no differences between the two approaches. In the case of Ag, also both approaches for the central peak provide similar values. However, if the results need to be extrapolated, a linear calibration might be preferred.

Mixtures of NPs of Au can be resolved if the sizes are sufficiently different. In any other case, the signal appears as a single peak, whose t_{delay} provides a result near the average size of the mixture. Ag mixtures are never resolved and only the average of the mixture can be estimated successfully. The presence of ions in mixtures increases the uncertainty of the measures.

For Core-shell measurements, sizing the metallic shell provides a result comparable to the global size of the NP, unlike what occurs for other atomic techniques (e.g., single particle-inductively coupled plasma mass spectrometry). Core size results were less accurate, but of the right order of magnitude. The size of the SiO_2 Core NPs was estimated indirectly, after the estimation of the total size determining the global size. To carry out this estimation, it is necessary to know previously the number of particles and the concentration of Si.

Silica shell distorts the atomization process of its core. In these cases, Au and Ag signal profiles are extremely delayed, hampering its sizing. Thus, this may serve as screening approach to identify the occurrence of this type of CSNPs.

- **III.5. References**

1 F. Gagné, P. Turcotte and C. Gagnon, ***Anal. Bioanal. Chem***., 2012, **404**, 2067–2072.
2 M. Resano, E. Garcia-Ruiz and R. Garde, ***J. Anal. At. Spectrom***., 2016, **31**, 2233–2241.

3 M. T. S. Cordero and J. M. C. Pav, ***J. Anal. At. Spectrom***., 2016, **31**, 2391–2398.
4 J. C. García-Mesa, P. Montoro-Leal, A. Rodríguez-Moreno, M. M. López Guerrero and E. I. Vereda Alonso, ***Talanta,*** 2021, 223(1), 121795.,
5 H. . Ortner, E. Bulska, U. Rohr, G. Schlemmer, S. Weinbruch and B. Welz, ***Spectrochim. Acta Part B At. Spectrosc.***, 2002, **57**, 1835–1853.
6 K. Leopold, A. Brandt and H. Tarren, ***J. Anal. At. Spectrom***., 2017, **32**, 723–730.
7 N. S. Feichtmeier and K. Leopold, ***Anal. Bioanal. Chem.***, 2013, **406**, 3887–3894.
8 A. Brandt, K. Kees and K. Leopold, ***J. Anal. At. Spectrom***., 2020, **35**, 2536–2544.
9 J. Gruszka, E. Zambrzycka-Szelewa, J. S. Kulpa and B. Godlewska-Żyłkiewicz, ***J. Anal. At. Spectrom***., 2018, **33**, 2133–2142.
10 J. Gruszka, A. Martyna and B. Godlewska-Żyłkiewicz, ***Talanta***, 2021, **230**(1), 122319.
11 T. Panyabut, N. Sirirat and A. Siripinyanond, ***Anal. Chim. Acta***, 2017, **1000**, 75–84.
12 K. Chatterjee, S. Sarkar, K. Jagajjanani Rao and S. Paria, ***Adv. Colloid Interface Sci***., 2014, **209**, 8–39.
13 W. Schärtl, ***Nanoscale***, 2010, **2**, 829–843.
14 R. Ghosh Chaudhuri and S. Paria, ***Chem. Rev.***, 2012, **112**, 2373–2433.
15 S. Kamimura, S. Yamashita, S. Abe, T. Tsubota and T. Ohno, ***Appl. Catal. B Environ***., 2017, **211**, 11–17.
16 M. Resano, L. Rello, M. Flórez and M. A. Belarra, ***Spectrochim. Acta - Part B At. Spectrosc***., 2011, **66**, 321–328.
17 M. Resano, E. García-Ruiz, M. Aramendía and M. A. Belarra, ***J. Anal. At. Spectrom***., 2019, **34**, 59–80.
18 A. Brandt, B. Gómez-Nieto, J. Friedland, R. Güttel and K. Leopold, ***Spectrochim. Acta - Part B At. Spectrosc***., 2020, **173**, 105976.
19 M. Resano, E. Garcia-Ruiz and R. Garde, ***J. Anal. At. Spectrom***., 2016, **31**, 2233
20 V. I. Korepanov and D. M. Sedlovets, ***Analyst***, 2018, **143**, 2674–2679.
21 L. Degenkolb, G. Metreveli, A. Philippe, A. Brandt, K. Leopold, L. Zehlike, H. J. Vogel, G. E. Schaumann, T. Baumann, M. Kaupenjohann, F. Lang, S. Kumahor and S. Klitzke, ***Sci. Total Environ***., 2018, **645**, 192–204.

4. General outline and conclusions

In this thesis three calibration approaches applied to high resolution continuum source graphite furnace atomic/molecular absorption spectrometry (HR CS GF AAS/MAS) have been studied.

- The advantages of multi-energy calibration for Br determination using Ca by monitoring the molecule CaBr have been assessed and compared with a similar approach developed during this study called multi energy ratios (MER). MER Data treatment does not require linear regression, and a dispersion of ratios between sample and sample+spike is calculated, this relationship is equivalent to the slope calculated in MEC. Since the basis mathematical relationship of this methodology is not linear, accuracy and precision of the method depend on the relative amounts of sample and amount of spike added. Better results were observed if the ratios/slope between signals of sample and saple+spike were near 0.5. results of MEC and MER were compared at two transitions of CaBr, $X^2\Sigma \rightarrow A^2\Pi$ (0,0) y $X^2\Sigma \rightarrow B^2\ \Sigma$ (1,0), showing that for similar molecular transition sensitivities, MER is a more reliable strategy. If the number of transitions is high and with different sensitivities, MEC provides better precision. Besides, a method for the calculus of the limits of detection and quantification using MER, which allows to identify if the lines have the sensitivity needed for its application. Despite a wavy background around 625 nm, and the presence of an unknown molecule, the measurements of a certified reference material QC3060 showed accurate results for Br.
- The capabilities of a machine learning algorithm (ML) for the determination of halogen proportions in active pharmaceutical ingredients (API) by means of a modular simultaneous *echelle* spectrograph (MOSES) prototype, capable of

increase the spectral window 100 times the values found in commercial continuum source instruments, coupled to a contrAA800G. Due to the univariate nature of the tree boosting algorithm, three models for F, Cl and Br each were calculated. Br model showed a bad performance, and it was decided to calculate its concentration through the remaining fraction. Validation parameters (Venetian blinds with ten splits and root mean square error of calibration, RMSEC) along with the four CRM proportions, which have variable quantities of the three halogens of interest, have shown the correct performance of the ML model. Additionally, MER was applied for the determination of F in these samples,.with errors under 5%. Afterwards, according to the proportions provided by the XGboost model and F concentration determined using MER, Br and Cl concentrations were determined, with errors under 10%.

- In this study, nanoparticles (NPs) and core-shell nanoparticles (SNPs) have been analyzed in order to identify between the atomization processes of NPs and ions of Cu, Pt, SiO_2, Au and Ag by means of HR CS GF AAS. Thus, a parameter called t_{delay} (atomization delay) was used, Absorbance spectra of NPs and ions of these elements did not show differences at any of the ramps studied.

  However, Au and Ag did show differences in their $t_{edlay,}$ calculated using a peak fit strategy. Au showed a unimodal signal for NPs following a Voigt profile,on the other hand, Au ions presented from one to two peaks, depending on the state of the tube. Ag, on the contrary, showed a complex signal for every specie analyzed, adjusting better for three Gaussian peaks. The analysis of mixtures of Au showed that only a few mixtures with high differing masses

presented a double peak. The rest of the mixtures appear as a unimodal signal. In both cases, size was estimated comparing their t_{delay} with pure AuNPs. Results show variable errors but ut seems that mixtures with significantly differing sizes provided size values closer to the expected ones. No mixture of AgNPs showed a bimodal peak. Hence, size was compared to the average size and average volume of NPs. Ag results presented lower error, except for a mixture with -19%, all mixtures showed less than 10% error in size relative to the average size.

CSNP measurements showed that size estimated using the shell if it is comprised of Au and Ag, provided similar results to the overall size of the CSNPS. Core size characterization, on the other hand, showed errors around 20%. CSNPs smaller of 20 nm presented a high error and imprecision. Lastly, the effect of the presence of silica in the structure of CSNPs with Au was assessed. In Au@SiNPs, Au-core atomizes much later than expected according to previous experiments, with a different peak profile. Si@AuNPs, Res660, Res800 and Res980, were analyzed to calculate the size of the Au structure (shell). However, these CSNPs are larger than the standards measured, and results were calculated by extrapolation. Errors between -20 and 20% were achieved, relatively good values were achieved for extrapolated data. Finally, Si-core was estimated in Si@AuNPs through the difference of the total volume of the CSNP (estimated experimentally sizing the Au-shell) and the volume of atoms of the shell occupied (volume per concentration of Au in the sample including the particle number, provided by the manufacturer).

4. Resumen y conclusiones generales

En esta tesis doctoral se han estudiado tres estrategias de calibración diferentes aplicadas a la espectrometría de absorción atómica/molecular de alta resolución con fuente continua (HR CS GF AAS/MAS).

- Se han analizado las ventajas de calibración multi-energía (MEC) para la determinación de bromo usando calcio mediante la monitorización de la molécula CaBr y se han comparado con una estrategia de calibración similar desarrollada durante este estudio denominada proporciones multi-energía (MER). El tratamiento de datos de MER no requiere regresión lineal, si no que se calcula una dispersión de las relaciones entre las señales de muestra y muestra+ adición, esta relación es equivalente a la pendiente obtenida mediante MEC.

  Debido a que la función matemática en la que se basa esta metodología no es lineal, la exactitud y la precisión del método dependerán de las relaciones de concentración entre la muestra y la cantidad de analito adicionada. Se observó que se obtenían mejores resultados si las proporciones entre las señales de muestra y muestra+ adición se aproximaban a 0.5. Los resultados obtenidos con MEC y MER se compararon a dos transiciones de CaBr, $X^2\Sigma \rightarrow A^2\Pi$ (0,0) y $X^2\Sigma \rightarrow B^2\ \Sigma$ (1,0), mostrando que, en el caso de transiciones moleculares con sensibilidades parecidas, MER es una estrategia más fiable. En caso de tener una gran cantidad de transiciones de diferente sensibilidad, MEC proporciona una mejor precisión. Se ha propuesto un método de cálculo del límite de detección y cuantificación utilizando MER, el cual permite además identificar si las líneas utilizadas presentan la sensibilidad necesaria para su utilización. A pesar de una línea base ondulante en torno a 625 nm, y de la

presencia de una molécula desconocida, las medidas de un material de referencia certificado QC3060 presentaron valores exactos de Br.

- Se ha estudiado la capacidad de un algoritmo de aprendizaje mecánico (ML) XGboost para la determinación de las proporciones de halógenos en ingredientes farmacéuticos activos (API) mediante el uso de un prototipo de espectrógrafo *echelle* modular simultáneo (MOSES), capaz de ampliar en más de 100 veces la ventana espectral de equipos de fuente continua comercial, acoplado a un contrAA800G. Debdo a que este algoritmo de impulso en árbol es univariable, se realizaron tres modelos para F, Cl y Br, de los cuales el Br presentaba peores prestaciones, y se decidió calcular mediante la fracción restante. Los parámetros de validación (ventanas Venecianas con diez separaciones y raíz media cuadrada del error de calibración) juntamente con las medidas de las proporciones de cuatro CRMs (penfluridol, efavirenz, gefitinib y selumetinib), los cuales presentan cantidades variadas de los tres halógenos de estudio, ha demostrado el correcto desarrollo del modelo. Adicionalmente, se aplicaron MER para la determinación de F en estas muestras, con errores por debajo del 5% y después, teniendo en cuenta las proporciones obtenidas mediante XGboost y la concentración de F, se calcularon las concentraciones de Cl y Br en las muestras, con errores inferiores al 10%
- En este estudio de nanopartículas (NPs) y nanopartículas core-shell (CSNPs) se han analizado los diferentes procesos de atomización de NPs e iones de Cu, Pt, SiO_2, Au y Ag mediante HR CS GF AAS. Para ello, se ha utilizado el parámetro t_{delay} (retraso de atomización). Los espectros de absorbancia

obtenidos al medir NPs e iones de estos elementos no mostraron diferencias entre sí a ninguna de las rampas de atomización estudiadas.

Sin embargo, y como ya era conocido, Au y Ag sí que mostraron diferencias en los t_{delay} calculados mediante ajuste de pico. Au presentó señales unimodales para NPs siguiendo un perfil Voigt, mientras que sus iones presentaban de uno a dos picos, dependiendo del estado del tubo de grafito. Ag, por el contrario, mostró una señal más compleja para todas las especies analizadas, ajustándose mejor a tres picos gaussianos. El análisis de mezclas de Au demostró que tan solo se separan unas pocas mezclas con grandes diferencias de tamaño, las demás aparecen como una señal unimodal. En ambos casos, se decidió estimar el tamaño estimado mediante la comparación con patrones de AuNPs puros. Los resultados muestran errores variados, pero parece que mezclas con tamaños significativamente diferentes, proporcionan valores más cercanos a los esperados. Las mezclas de AgNPs no mostraron ningún pico bimodal. Por tanto, el tamaño se comparó al tamaño medio y al volumen medio de las NPs. Los resultados de Ag presentaron un menor error, excepto una de las mezclas con un -19%, todas las mezclas presentaron un error menor del 10% respecto al tamaño medio.

Las medidas de CSNPs mostró que estimando el tamaño del *shell* si éste es Au o Ag, proporciona resultados parecidos al tamaño general de la CSNP medida. Los resultados de caracterizar el tamaño del *core* por el contrario presentaron errores en torno al 20%. Las CSNPs más pequeñas de 20 nm presentaron un error muy alto y también gran imprecisión.

Por último, se evaluó el efecto de la silica en CSNPs de este compuesto con Au. relativamente bajos. Al analizar CSNPs Au-*core;* Si-*shell* el Au atomiza mucho

más tarde, presentando un perfil distinto de señal. Res660, Res800 y Res980 presentan un *shell* de oro. Debido al gran tamaño de estas CSNPs, sus valores tuvieron que ser extrapolados, sin embargo, los errores del tamaño se encuentran entre el 20 y el -20% relativamente buenos para una extrapolación. Por último, se estimó el tamaño de Si-*core* en estas últimas CSNPs mediante un cálculo por diferencia de volúmenes entre el total (calculado mediante el tamaño experimental obtenido del *shell*) y el volumen del *shell* ocupado (volumen ocupado por la concentración de oro determinada en la muestra teniendo en cuenta el número de partículas que hay, dato proporcionado por el fabricante).